Investigating Pulse-Type Glaciers in the Canadian Arctic: A Case Study of the Characteristics of Dobbin Bay Glacier, Parrish Glacier, and Eugenie Glacier within the Agassiz Ice Cap

by

Owen Nowitsky

A thesis

presented to the University of Waterloo

in fulfilment of the

thesis requirement for the degree of

Master of Science

in

Geography

Waterloo, Ontario, Canada, 2026

© Owen Nowitsky 2026

Author's Declaration

This thesis consists of material all of which I authored or co-authored: see Statement of Contributions included in the thesis. This is a true copy of the thesis, including any required final revisions, as accepted by my examiners.

I understand that my thesis may be made electronically available to the public.

Statement of Contributions

Data analysis and writing of this thesis were done by Owen Nowitsky, under the supervision of Dr. Wesley Van Wychen. This thesis was presented in a traditional thesis format. All chapters were written by the lead author and with suggestions and edits provided by Dr. Wesley Van Wychen as my graduate supervisor. Generative AI was used throughout the drafting process for feedback on clarity, structure, and grammar. All research, analysis, interpretation and writing are the original work undertaken by the author.

Abstract

Characterizing irregular glacier dynamics is crucial for understanding the drivers of variations in ice motion, improving glacier dynamic modelling, and projecting future contributions to sea-level rise. The majority of glaciers exhibiting irregular dynamics have been classified as 'surge-type' glaciers, even though some glaciers display dynamic behaviour that falls outside the classical definition of surging. One such category is 'pulse-type' glaciers, which have been identified as a subset type of glacier surging within the Canadian Arctic. Similar to surge-type glaciers, 'pulsing glaciers' experience quiescent and active phases but experience variations of ice motion on shorter timescales, with fluctuations in glacier flow restricted to the terminus region where the bed lies below sea level. Due to the recency of this identification (i.e., first reported in Van Wychen et al., 2016), few studies of 'pulse-type' glaciers have been conducted, leaving a gap in the understanding their processes and characteristics. In this study, three previously identified pulse-type glaciers, Dobbin Bay Glacier, Parrish Glacier and Eugenie Glacier, located on Agassiz Ice Cap within the Canadian High Arctic, are studied using measurements of surface elevation, ice flow, terminus position and subglacial topography and are used to investigate and distinguish pulse characteristics from other forms of dynamic instability. Pulse events were identified on Dobbin Bay Glacier from 2004 to 2008, Parrish Glacier from 2004 to 2010, and Eugenie Glacier from before 2000 to 2008. Across all three glaciers, a surface elevation rise of 2-5 m a^{-1} was observed at regions where subglacial sills or sharp valley turns were present, while downglacier regions experienced surface elevation loss of 2- 4 m a^{-1}. During pulse events, velocities within the pulse region ranged from 500 to 1100 m a^{-1}, compared to upglacier regions, which experienced velocities from 50 - 110 m a^{-1} during both quiescence and pulse events. These findings refine the current definitions of pulse-type glaciers and provide further insight into irregular glacier dynamics within the Canadian Arctic Archipelago.

Acknowledgements

Firstly, I would like to acknowledge my supervisor, Dr. Wesley Van Wychen, who always encouraged me to continue striving for academic and career success. Secondly, I would like to acknowledge the support of my lab group and the cryosphere lab for their friendship, guidance, and academic support. They have all supported me in becoming a better version of myself. Thank you, Danielle Hallé, Jae Hun Kim, Tamara Marchant, Kristie Shannon, Kirsi O'Quinn and Katie Croutch, for endless amounts of inspiration, knowledge and joy.

I would also like to thank my family and friends for their support throughout my studies. Thank you for your continued emotional support, for helping me recover from injuries and for listening to me spout facts about glaciers.

Lastly, I would like to acknowledge the financial support of Environment and Climate Change Canada - Climate Research Division Projects: GCXE23S029 and GCXE26S065, and Natural Sciences and Engineering Research Council of Canada (NSERC): RGPIN-02443-2021, as well as the International Arctic Science Committee, the Canada Foundation for Innovation, the Province of Ontario and the University of Waterloo.

Table of Contents

Author's Declaration ... ii
Statement of Contributions ... iii
Abstract ... iv
Acknowledgements ... v
List of Figures ... viii
List of Tables ... xi
List of Abbreviations ... xii
Chapter 1 - Introduction ... *1*
1.1 Background ... 1
1.1.1 Changing Polar Environments ... 1
1.1.2 Impact of Irregular Glacier Dynamics ... 2
1.2 Research Objectives ... 4
1.3 Thesis Structure ... 4
Chapter 2 – Study Region & Literature Review ... *6*
2.1 Study Region ... 6
2.1.1Agassiz Ice Cap ... 6
2.2 Study Glaciers ... 7
2.1.2 Pulse-Type Glaciers ... 8
2.2 Literature Review ... 9
2.2.1 Glacier Mass Balance ... 10
2.2.2 Balance Velocities ... 12
2.3 Glacier Motion ... 13
2.2.4 Subglacial Hydrology Controls on Ice Motion ... 19
2.2.5 Dynamic Instabilities ... 22
Chapter 3 Methodology ... *28*
3.1 Glacier Elevation Change ... 28
3.1.1 ArcticDEM ... 28
3.1.2 XDEM ... 31
3.2 Velocity Variability ... 34
3.2.1 ITS_LIVE Optical Velocity Processing ... 34
3.2.2 ArcGIS Pro Post Processing ... 35
3.2.2 TerraSAR-X & TanDEM-X Velocity Processing ... 36
3.3 Terminus Position Mapping ... 37
3.3.1 Optical Imagery Collection ... 38
3.3.2 Terminus Position Delineation ... 39
3.4 Basal Topography ... 42
3.5 Deflection Angle ... 43
3.6 Method Summary ... 44
Chapter 4 - Results ... *46*
4.1 Dobbin Bay Glacier ... 46
4.1.1 Dobbin Bay Glacier Geometry Change ... 47
4.1.2 Dobbin Bay Glacier Ice Velocity ... 49

4.1.3 Dobbin Bay Terminus Positions Change 51
4.1.4 Dobbin Bay Glacier Bed 53

4.2 Parrish Glacier 54
4.2.1 Parrish Glacier Geometry 55
4.2.2 Parrish Glacier Velocity 57
4.2.3 Parrish Terminus Positions 58
4.2.4 Parrish Bed Topography 60

4.3 Eugenie Glacier 61
4.3.1 Eugenie Glacier Geometry Change 62
4.3.2 Eugenie Glacier Ice Velocity 64
4.2.3 Eugenie Glacier Terminus Positions 66
4.2.4 Eugenie Glacier Bed Topography 68

4.4 Summary of Results 70

Chapter 5 – Discussion 71

5.1 Pulse Event Identification 71
5.1.1 Dobbin Bay Glacier 'Pulse' Event / Dobbin Bay Glacier Pulse Evidence 71
5.1.2 Parrish Glacier 'Pulse' Event 73
5.1.3 Eugenie Glacier 'Pulse' Event 75
5.1.4 Dynamic event summary 77

5.2 Comparisons of 'Pulse' Dynamics 79
5.2.1 Similarities between all study glaciers 79
5.2.2 Similarities between Dobbin Bay and Parrish Glaciers 82
5.2.3 Similarities between Parrish and Eugenie Glaciers 83
5.2.4 Eugenie Glacier Differences 85
5.2.5 Summary 86

5.3 Contextualizing 'Pulse-Type' Glaciers with Surge-Type Glaciers 87
5.3.1 Pulse-Type Glacier Definition 88
5.3.2 Comparing Pulse-Type Glaciers to Regional Surge-Type Glaciers 89
5.3.3 Pulse-type glacier categorization 94

Chapter 6 - Conclusion 98

6.1 Summary and Primary Findings 98

6.2 Limitations 101

6.3 Next Steps 102

References 104

Appendices 110

List of Figures

Figure 2-1: Study Sites Parrish Glacier, Eugenie Glacier and Dobbin Bay Glacier, pictured left to right (Landsat 8 imagery from June 2, 2019, in WGS 1984 UTM 18N). The top right inset map provides an overview of the CAA and includes all glacier bodies within the region, with the study site marked as a star. All glacier shapefiles were retrieved from the RGI consortium, 2023.....8

Figure 2-2: A summary of typical accumulation and ablation processes experienced within glacial systems. Accumulation processes occur at higher elevations, and ablation processes more often occur at lower elevations and at the glacier's terminus. (Davies, 2020) 11

Figure 2-3: Balance velocity diagram. For a glacier to be in steady state, accumulation and ablation rates need to be equal. In this diagram, glacier A has low rates of ablation, meaning that less accumulation is needed, especially compared to glacier B, which needs higher rates of accumulation to match the higher rates of ablation. (modified from Sugen and John 1976) 12

Figure 2-4: Conceptual diagram of glacier showing the main normal (σ) and shear (τ) stresses. Normal stress is shown in blue and shear stress is shown in red. Normal stress primarily drives ice flow, while shear stress both inhibits and encourages flow (Jennings & Hambrey, 2021).....14

Figure 2-5: Diagram showing simple shear. Under simple shear, the square is skewed, with 'R and 'S sliding forward. While the shape of the square changes, its area is preserved, as it is neither squished nor stretched. (Benn & Evans, 2013).....14

Figure 2-6: Diagram of glacier motion as a result of a) internal deformation, b) internal deformation and basal sliding, and c) internal deformation, basal sliding and bed deformation (Boulton 1996).....15

Figure 2-7: Variation in Ice flow law parameter A under the influence of temperature. As the temperature rises, flow rates rise. With variation in the linear relation occurring near the melting point. (Benn & Evans, 2013; Paterson, 1994).....16

Figure 2-8: Diagram of regelation, ice builds up on the stoss side (right), leading to melt. Water then flows over the obstacle at the bed before refreezing on the lee side (left). The latent heat transfer from the transformation of water to ice further promotes the reglation process as energy transfers from the lee to the stoss side.(Benn & Evans, 2013).....18

Figure 2-9: Different subglacial drainage configurations 1) water moving through a deformable till. 2) Darcian porewater flow. 3) Pipe flow 4) Dendritic network 5) Linked cavities. 6) Braided channels 7) Thin film. Configurations 3 and 4 are efficient channelized systems, while configurations 1, 2, 5, 6 and 7 are inefficient distributed systems. (Benn and Evans, 2013).....20

Figure 2-10: Graph of various observations on Belcher Glacier from day 170 (July 19th) to 217 (August 5th), 2009. (a) Area gain of lakes and water-filled crevasses. (B) Area loss of Lakes and water-filled crevasses, showing the rate of drainage at different lakes. (c) Surface ice velocity of four GPS systems. (d) Cumulative elevation change of GPS systems. (e)Air temperature at two GPS systems. Drainage events, where large patterns of drainage occur, are highlighted and annotated as D(x) through graphs a, b and c. Motion events are denoted in graph c as A(x). Retrieved from (Danielson & Sharp, 2013).....21

Figure 2-11: Various glacier surges and surge mechanics. a) Diagrams of both land- and marine-terminating surge-type glaciers undergoing various stages of surge processes. The land-terminating glacier is undergoing a downglacier propagating surge, while the marine-terminating glacier is experiencing an up-propagating surge. b) Conceptual diagram showing the differences and characteristics of various types of glaciers. Providing the magnitude of increase in velocity along with the duration of fast flow. c) A summary of the subglacial processes within surge-type glaciers. (Lovell et al., 2026).....23

Figure 2-12: Centerline surface velocity, bed topography and elevation change of Dobbin Bay Glacier (left) and Parrish Glacier (Right) (Van Wychen, 2016). 26

Figure 3-1: ArcticDEM's spatial coverage of DEM products across the Arctic. The left image shows the density of StripMap products throughout the Arctic, highlighting areas of high temporal coverage in yellow and low temporal coverage in blue. The right image shows the coverage of mosaic products across the Arctic. (Porter et al., 2022).....29

Figure 3-2: Shows two DEM products south of Parrish Glacier, with two different errors highlighted in the 2011 DEM, that are not present in the 2016 DEM. A. shows a combination of cloud cover errors combined with a processing error. The processing error manifests in an unnatural straight line. B. shows various examples of obscuring weather features like clouds. These features suggest erratic, sharp rises in elevation that are unlikely to be present in the topography. For these reasons and given the absence of these features in the 2016 DEM, features A and B are identified as errors.....31

Figure 3-3: A diagram of the importance of co-registration in DEM products when comparing elevation. In the unregistered diagram, the DEM sees the circle and the star as the same point, leading to the elevation on bedrock being two different values. But when the co-registered offset between x and y values is reduced, leading to the bedrock having the same elevation (derived from Nuth and Kääb, 2011) 32

Figure 3-4: illustrates a difficult-to-delineate image. The image is a Landsat 7 capture from July 16, 2003, showing clear ocean, icebergs, and mélange along the ocean-terminus interface. Overlaid on the image is a red dashed circle showing where the terminus was delineated to provide an example of the decisions made on terminus delineations.....40

Figure 3-5: The created terminus intersect lines used to measure the change in distance between yearly terminus positions. Showing Parrish Glacier on the left, Dobbin Bay Glacier in the middle and Eugenie Glacier on the right. All overlaid on Landsat imagery, June 2, 2019.....41

Figure 4-1: The primary trunk of Dobbin Bay Glacier, divided into three sections. Overlayed on Landsat Imagery (collected June 2, 2019) 47

Figure 4-2: Surface elevation change from 2012 to 2022 over Dobbin Bay Glacier, derived from ArcticDEM StripMap using xDEM. Overlaid on Landsat 8 imagery (July 2, 2019). 48

Figure 4-3: Annual surface elevation change composite of Dobbin Bay Glacier, derived from xDEM. Overlaid on a Landsat 8 true colour composite imagery acquired on June 2, 2019. 49

Figure 4-4: ITS_LIVE composite velocity products by NASA JET Propulsion Laboratory, covering Dobbin Bay Glacier from 2000 to 2022, derived from optical imagery. Each image is the average surface ice velocity collected over the year.....51

Figure 4-5: Evolution of annual terminus position of Dobbin Bay Glacier from 1959 to 2024. Terminus positions are grouped based on the trend of motion presented in graph D. A) spans from 1959 to 2003, B) spans from 2003 to 2007, and C) spans from 2008 to 2024. Terminus positions are overlaid on relevant satellite captures: A) Landsat 7 satellite image, July 9, 1999; B) ASTER satellite image captured, July 22, 2007; C) Landsat 8, July 2, 2019. D) provides the terminus position along transects through the glacier and compares the position relative to the 1959 terminus position. 52

Figure 4-6: Subglacial topography of Dobbin Bay Glacier, obtained from the CReSIS MCoRDS sensor, acquired in 2014. Regions of potential error are denoted by a red arrow. Sea level is denoted by a dotted line. Overlayed on Landsat true-colour composite imagery (June 2, 2019). 53

Figure 4-7: The main trunk of Parrish Glacier, divided into four regions. Overlayed on Landsat Imagery (June 2, 2019)....55

Figure 4-8: Surface elevation change of Parrish Glacier from 2011 – 2023, derived from ArcticDEM StripMap using xDEM. Overlaid on Landsat 8 imagery collected July 2, 2019. 56

Figure 4-9: Surface elevation change composite of Parrish Glacier, derived from xDEM. Overlaid on a Landsat 8 imagery acquired on June 2, 2019. 57

Figure 4-10: ITS_LIVE composite velocity products by NASA JET Propulsion Laboratory, covering Parrish Glacier from 2000 to 2022 and derived from optical imagery. 2003 was not included due to the high presence of error. Each image shows the average velocities collected over the year. Overlaid on Landsat 8 imagery collected June 2, 2019.....58

Figure 4-11: Evolution of annual terminus positions of Parrish Glacier from 1959 to 2024. Terminus Positions are grouped based on the trend of motion presented in graph D. A) spans from 1959 to 2003, B) spans from 2003 to 2012, and C) spans from 2012 to 2024. Terminus positions are overlaid on correlating satellite imagery: A) Landsat 7, July 16, 2003; B) Aster, July 5, 2011; C Landsat 8, July 1, 2023. Graph D provides the terminus position along transects through the glacier and compares the position to the 1959 terminus position. 60

Figure 4-12: Subglacial topography of Parrish Glacier, from the CReSIS MCoRDS sensor, acquired in 2014. Regions of potential error are denoted by a red arrow. Sea level is denoted by a dotted line. Overlayed on Landsat Imagery (June 2, 2019). 61

Figure 4-13: The main trunk of Eugenie Glacier, divided into four regions. Overlaid on Landsat Imagery (June 2, 2019).....62

Figure 4-14: Surface elevation change of Eugenie Glacier from 2012 – 2021, derived from ArcticDEM StripMaps using xDEM. Overlaid on Landsat 8 imagery (July 2, 2019). 63

Figure 4-15: Surface elevation change composite of Eugenie Glacier, derived from xDEM. Overlaid on Landsat 8 imagery collected June 2, 2019. 64

Figure 4-16: ITS_LIVE composite velocity products by NASA JET Propulsion Laboratory, covering Eugenie Glacier from 2000 to 2022, derived from optical imagery. Each image is the average surface ice velocity collected over the year. Overlaid on Landsat 8 imagery collected June 2, 2019. 66

Figure 4-17: Evolution of annual terminus positions of Eugenie Glacier from 1959 to 2024. Terminus positions are grouped based on the trend of motion presented in graph d). a) spans from 1959 to 1988, b) spans from 1988 to 2008, and c) spans from 2012 to 2024. The terminus positions are overlaid on correlating satellite imagery: a SPOT, July 23, 1988, b) Landsat 7,

June 16, 2000, c) Landsat 8, July 2, 2019. d) provides the terminus position along 6 transects through the glacier and compares it with the 1959 terminus position. 68

Figure 4-18: Subglacial topography of Parrish Glacier, from the CReSIS MCoRDS sensor, acquired in 2014. Regions of potential error are denoted by a red arrow, and questionable areas by a yellow arrow. Sea level is denoted by a dotted line. Overlayed on Landsat Imagery (June 2, 2019). 69

Figure 5-1: Velocity variability, bed geometry and decadal elevation differences of the bottom 15 km of Dobbin Bay Glacier. Velocity variability was collected from the maximum and minimum velocities experienced across the annual velocity records. Markers along the centerline of the glacier are placed at intervals of 2.5 km. Overlayed on Landsat Imagery (June 2, 2019)...72

Figure 5-2: The terminus evolution of Dobbin Bay Glacier from 1959 to 2024, overlaid on the annual surface ice velocity extracted every 2.5 km along the centerline of Dobbin Bay Glacier. The active phase of the pulse is denoted by the black dashed line. 73

Figure 5-3: Velocity variability, bed geometry and decadal elevation differences of the bottom 15 km of Parrish Glacier. Velocity variability was collected from the maximum and minimum velocities experienced across the annual velocity records. Markers along the centerline of the glacier are placed at 2.5 km intervals. Overlayed on Landsat Imagery (June 2, 2019)...74

Figure 5-4: The terminus evolution of Parrish Glacier from 1959 to 2024, overlaid on the annual surface ice velocity extracted every 2.5 km along the centerline of Parrish Glacier. The active phase of the pulse is denoted by the black dashed line.....75

Figure 5-5: Velocity variability, bed geometry and decadal elevation differences of the bottom 15 km of Eugenie Glacier. Velocity variability was collected from the maximum and minimum velocities experienced across the annual velocity records. Markers along the centerline of the glacier are placed at 2.5 km intervals. Overlayed on Landsat Imagery (June 2, 2019)....76

Figure 5-6: The terminus evolution of Eugenie Glacier from 1959 to 2024. Overlaid on the annual surface ice velocity extracted every 2.5 km along the centerline of the glacier. The active phase of the pulse is denoted by the black dashed line...77

Figure 5-7: Pulse Activation Regions of the study glaciers: Dobbin Bay, Parrish, and Eugenie. Overlayed on Landsat Imagery (June 2, 2019).....78

Figure 5-8: Summary of interpreted pulse-type activity for Dobbin Bay Glacier (purple), Eugenie Glacier (blue) and Parrish Glacier (orange), from 1959 to 2024. 79

Figure 5-9: bed topography with highlights of subglacial ridges of: a) Dobbin Bay glacier, b) Parrish Glacier, c) Eugenie Glacier. Overlayed on Landsat Imagery (June 2, 2019). 80

Figure 5-10: Graphs for each study glacier, comparing bed elevation to decadal elevation change and surface ice velocities during pulse and quiescence. All values were pulled along the centerline of the glacier, which is tracked along the x-axis. The left y-axis provides the elevation reading of the surface (green line) and bed(black line) of the glacier. Surface ice velocities are tracked along the right y-axis, with the dotted red line representing velocities during a pulse event and the dotted black line representing quiescent velocities. The decadal elevation change is represented by the colour map scaling from brown to purple. 82

Figure 5-11: Deflection angle of the valley experienced by a) Parrish Glacier and b) Eugenie Glacier. Overlayed on Landsat Imagery (June 2, 2019). 84

Figure 5-12: Highlight of the surface ice velocity of Eugenie Glacier's pulse region during the pulse phase a), 2005 and during quiescence b), 2016. Overlayed on Landsat Imagery (June 2, 2019). 86

Figure 5-13: Centerline ice velocities of Southeast-2 Glacier from 2013 to 2024 derived from ITS_LIVE v2. Black markers indicate the upstream limit of fast flow >120 m a^{-1} within the glacier trunk (lower ~20 km), illustrating the upglacier propagation of the glacier over time (Lauzon et al. 2026). 91

Figure 5-14: Centerline surface velocity (m a^{-1}) of Mittie Glacier from 1988 to 2018 along the centerline of the glacier. Years with an asterisk denote years where velocities were taken from ITS_LIVE; velocities for 1996 were derived from SAR offset tracking, while annual ranges were derived from optical image feature tracking (Copland et al, 2024).....92

Figure 5-15: a) provides the surface topography (light blue) and basal topography (black) of Good Friday Glacier. B) provides the centerline ice surface velocities from 1987 to 2018. Velocities were derived through SAR speckle tracking. The yellow diamond indicates the velocities recorded at the terminus of Good Friday Glacier in 1959. (Medrzycka et al., 2019).....93

List of Tables

Table 1-1: Global mean sea level budget spanning different epochs from 1901-2015, presented values are in mm yr^{-1}. (IPCC 2022)..... 2

Table 3-1: Description of the satellite imagery used to delineate terminus positions.....38

Table 3-2: Summary of remote sensing products used along with associated methodology and temporal coverage of the dataset.....45

Table 5-1: Comparison of key dynamic characteristics between surge-type and pulse-type glaciers in the CAA.....95

List of Abbreviations

a.s.l - Above Sea Level

ASTER - Advanced Spaceborne Thermal Emission and Reflection Radiometer

Auto-RIFT - Repeat Image Feature Tracking

CAA - Canadian Arctic Archipelago

CReSIS - Centre for Remote Sensing of Ice Sheets

DEM - Digital elevation model

GLOF - Glacier Lake outburst Flood

GMSL - Global Mean Sea Level Rise

HH - Horizontal-Horizontal

HV - Horizontal-Vertical

IPCC - Intergovernmental Panel on Climate Change

LST - Land Surface Temperature

MCoRDS - Multichannel Coherent Data Depth Sounder

NCC - Normalized Cross-Correlation

NMAD – Normalized Median Absolute Deviation

NOAA - National Oceanic and Atmospheric Administration

NSIDC - National Snow and Ice Data Center

QEI - Queen Elizabeth Islands

RGI - Randolph Glacier Inventory

SAR - Synthetic Aperture Radar

SLR - Sea Level Rise

SPOT - Satellite Pour l'Observation de la Terre

UTM - Universal Transverse Mercator

VV - Vertical-Vertical

VH - Vertical-Horizontal

WGS - World Geodetic System

Chapter 1 - Introduction

1.1 Background

1.1.1 Changing Polar Environments

Polar regions are both highly important and rapidly changing environments. They "encompass surface areas equaling 20% of the global ocean, more than 90% of the world's continuous and discontinuous permafrost area, 69% of the world's glacier area (including both of the world's ice sheets) and almost all of the world's sea ice and land areas with the most persistent winter snow cover" (IPCC, 2022). However, both polar regions are experiencing rapid change due to climate change. For example, annual terrestrial snow cover is decreasing, permafrost regions are thawing, and glacier mass loss is increasing (Thoman et al., 2023). Increased glacier mass loss is particularly important, as loss of terrestrial ice contributes directly to global sea level rise. Sea-level rise has global implications, but it is especially relevant for low-elevation areas, island communities, and low-lying ecosystems. From 2006 to 2015, glaciers outside the ice sheets contributed an estimated 0.61 mm of sea-level rise per year (Table 1-1). While the largest portion of sea level rise is a result of thermal expansion, the importance of sea level contributions from glaciers is increasing over time (Table 1-1). Glaciers can contribute to global sea level rise in two ways, either through increased meltwater that reaches the ocean or through changes in ice flow behavior which increases the amount of ice that is moved from the land to the ocean. To effectively project future sea level rise outcomes under differing climate models, a detailed understanding of both future melt rates and future glacial dynamics is required.

Table 1-1: Global mean sea level budget spanning different epochs from 1901-2015, presented values are in mm yr^{-1}. (IPCC 2022)

Source	1901–1990	1970–2015	1993–2015	2006–2015
Observed contribution to GMSL rise				
Thermal expansion		0.89 (0.84–0.94) [a]	1.36 (0.96–1.76) [a]	1.40 (1.08–1.72)[a]
Glaciers except in Greenland and Antarctica	0.49 (0.34–0.64)[b]	0.46 (0.21–0.72)[o]	0.56 (0.34–0.78) [p]	0.61 (0.53–0.69)[n]
GIS including peripheral glaciers	0.40 (0.23–0.57)[c]		0.46 (0.21–0.71)[d]	0.77 (0.72–0.82)[d]
Antarctica ice sheet including peripheral glaciers			0.29 (0.11–0.47)[e]	0.43 (0.34–0.52)[e]
Land water storage	–0.12[f]	–0.07[f]	0.09[f]	–0.21 (–0.36–0.06)[g]
Ocean mass				2.23 (2.07–2.39)[h]
Total contributions			**2.76 (2.21–3.31)[i]**	**3.00 (2.62–3.38)[i]**
Observed GMSL rise from tide gauges and altimetry	**1.38 (0.81–1.95)**	**2.06 (1.77–2.34)[j]**	**3.16 (2.79–3.53)[k]**	**3.58 (3.10–4.06)[k]**
Modelled contributions to GMSL rise				
Thermal expansion	0.32 (0.04–0.60)	0.97 (0.45–1.48)	1.48 (0.86–2.11)	1.52 (0.96–2.09)
Glaciers	0.53 (0.38–0.68)	0.73 (0.50–0.95)	0.99 (0.60–1.38)	1.10 (0.64–1.56)
Greenland SMB	–0.02 (–0.05–0.02)	0.03 (–0.01–0.07)	0.08 (–0.01–0.16)	0.12 (–0.02–0.26)
Total including land water storage and ice discharge [l]	0.71 (0.39–1.03)	1.88 (1.31–2.45)	3.13 (2.38–3.88)	3.54 (2.79–4.29)
Residual with respect to observed GMSL rise[m]	**0.67 (0.02–1.32)**	**0.18 (–0.46–0.82)**	**0.03 (–0.81–0.87)**	**0.04 (–0.85–0.93)**

1.1.2 Impact of Irregular Glacier Dynamics

At present, sea-level rise projections are largely driven by glacier mass balance, with less of an emphasis placed on the contributions from ice dynamics. In many cases, even when ice dynamics are included, variations in ice motion over time are neglected (IPCC, 2022). However, around 1% of all glaciers experience irregular glacier dynamics (Jiskoot et al., 2000; Lovell et al., 2026), or dynamic instabilities, where they experience significant variations in their flow speeds over time that differ greatly from what they should experience based on their mass balance conditions (i.e. their balance velocities). This can result in significant oscillations in mass contributions to the ocean from individual glacier basins over time. Within the Canadian Arctic, glaciers that experience dynamic instabilities have been loosely grouped into three categories: surge-type glaciers, consistent acceleration-type glaciers and pulse-type glaciers (Van Wychen et al., 2016). Of the three, pulse-type glaciers have been most robustly described and characterized in the Canadian Arctic by Van Wychen et al., (2016). In this work, eight glaciers were identified as pulse-type: Antonnette Tuborg, Eugenie, Dobbin Bay and Parrish

(all located on the Agassiz Ice Cap), Ekblaw (located on Prince of Wales Icefield), and Sydkap (located on Sydkap Ice Cap), although many of these glaciers were previously identified as surge-type or potential surge-type in Copland et al., (2003). These glaciers exhibited surface deformation characteristics consistent with surge-type activity, but upon further investigation (Van Wychen et al., 2016), their dynamics were found to be somewhat adjacent to the traditional definition of a surge-type glacier. Pulse-type glaciers experience variations in velocity that differ from their mass balance conditions (like surge-type glaciers), but they only seem to experience velocity variability in the near-terminus areas of the glacier, rather than along the entire glacier length as would be expected for a surge-type glacier. More specifically, the dynamic variations of pulse-type glaciers primarily occur in regions where the glacier's bed is below sea level (Van Wychen et al., 2016). As discussed in Van Wychen et al. (2016), further investigation is required to better understand the characteristics of pulse-type glaciers, including the drivers of dynamic change and what role the glacier bed and geometry play in regulating ice motion. While pulse-type glaciers make up a small percentage of the total glacial bodies in the CAA and the world, understanding their dynamics and drivers can provide further understanding of irregular dynamics within the field of glaciology as a whole. In Van Wychen et al. (2016), Dobbin Bay and Parrish Glacier were used to identify and best exemplify pulse-type glaciers. However, with expanded datasets, more information can be gleaned from these glaciers. In addition to these two glaciers, Eugenie Glacier, which is situated between Dobbin Bay and Parrish Glacier, has shown pulse-type characteristics but has never been included in a dedicated study. Due to previous identification in the literature, their observed characteristics, and their proximity to each other, these three glaciers can provide further insight into pulse-type dynamics.

1.2 Research Objectives

This thesis aims to characterize pulse-type glacier activity in the Canadian Arctic Archipelago. These characterizations will further define pulse-type glaciers and distinguish them from surge-type glaciers. The major research objectives of this study are listed below.

1) Build a record of mass build-up through surface elevation change, ice velocity through ITS_LIVE and offset tracking of satellite data, and terminus position change using satellite imagery for Dobbin Bay Glacier, Parrish Glacier and Eugenie Glacier from 2000 to 2023.
2) Define regions of pulse-type activity on the selected glaciers based on the observed characteristics and compare the pulse regions between the glacier basins.
3) Distinguish pulse-type signals between the three different basins and compare the observed characteristics to observations of other glaciers in the Canadian Arctic Archipelago that have been identified as dynamically unstable.

This work will help provide an understanding of a previously understudied glacial dynamic behaviour and contribute to the broader definitions of behaviours that fall within the classification of 'dynamic instabilities' within the field.

1.3 Thesis Structure

This thesis is presented in a traditional thesis format and is comprised of six chapters. Chapter 1 provides an introduction and context surrounding the research topic and outlines the objectives. Chapter 2 introduces the study glaciers and provides an overview of the important fundamental literature that informs the research objectives (as a literature review). Chapter 3 describes the methodology and datasets used in the study. Following this, Chapter 4 presents the results, while Chapter 5 provides a discussion and interpretation of the results. Finally,

Chapter 6 concludes the thesis, summarizes the outcomes, and provides an outlook for future research on the topic.

Chapter 2 – Study Region & Literature Review

2.1 Study Region

The Canadian Arctic Archipelago (CAA) is a collection of islands located in Canada's Arctic (Figure 2-1, inset). The CAA is often split into a northern region (NCAA), containing the Queen Elizabeth Islands (QEI), and a southern region (SCAA), which contains Baffin Island and Bylot Island, with the division at approximately 74°N. Due to the CAA's high latitude, the region experiences short, cool summers followed by long, cold winters (Van Wychen et al., 2020). Both the NCAA and SCAA have prominent coastal mountain ranges along the coast of Baffin Bay, with maximum elevations ranging from 1800 m to 2200 m above sea level. These tall, mountainous regions, along with low Arctic temperatures, allow for the development and maintenance of the large glacial bodies found within the region (Van Wychen et al., 2020). Overall, the CAA is a highly glacierized area, with an approximate surface area of ~150 000 km^2 of glacierized terrain, representing ~28% of the world's glacier area outside the ice sheets (Sharp et al, 2014). However, the NCAA contains the majority of the region's glaciers, with a surface area of 107 000 $km^{2,}$ and much of this ice is found within the large ice caps and ice fields identified in the inset map of Figure 2-1.

2.1.1Agassiz Ice Cap

Agassiz Ice Cap is one of five major glacial regions on Ellesmere Island and contains the three individual glaciers which were selected for this thesis (Figure 2-1). Ice caps are large glacier systems that are unconstrained by their topography and have a 'dome-like' structure with various outlet glaciers that move mass to lower elevation regions of the system (Benn and Evans, 2013). Agassiz Ice Cap has an approximate surface area of 17 700 km^2 and a maximum elevation of nearly 2 200 m based on a survey of ArcticDEM data (Porter et al., 2022, RGI Consortium, 2023). The Agassiz Ice Cap is drained by 40 outlet glaciers that radiate outward

from the interior to lower-elevation areas, terminating both on land and in the ocean (RGI Consortium, 2023). The ocean-terminating glaciers feed into multiple bays and fjords surrounding the island, with eastern-flowing glaciers eventually contributing to Baffin Bay and western-flowing glaciers emptying into Greely Fiord. Between 2000 and 2015, Agassiz Ice Cap had a mean summer land surface temperature spanning -2.09 °C to 1.25 °C, with the warmest mean summer LST occurring in 2012 (Mortimer et al., 2016). The warming of the Agassiz Ice Cap mean summer temperatures is occurring at a faster rate at higher elevations, with regions above 1 400 m a.s.l. experiencing twice the rate of change in LST as lower elevations below 1 000 m a.s.l. (Mortimer et al., 2016).

2.2 Study Glaciers

The study sites selected for this research were based on Van Wychen et al. (2016), where eight pulse-type glaciers were originally identified within the CAA. Of the eight that were identified, Dobbin Bay Glacier and Parrish Glacier of Agassiz Ice Cap were selected for research in this thesis because they provided the clearest examples of the 'pulse process' described within Van Wychen et al. (2016). Additionally, Eugenie Glacier was also selected for this study due to its proximity to Dobbin Bay Glacier and Parrish Glacier, making data collection and comparison relatively straightforward. These three ocean-terminating glaciers are adjacent to each other and are located on the southeastern portion of Agassiz Ice Cap (Figure 2-1).

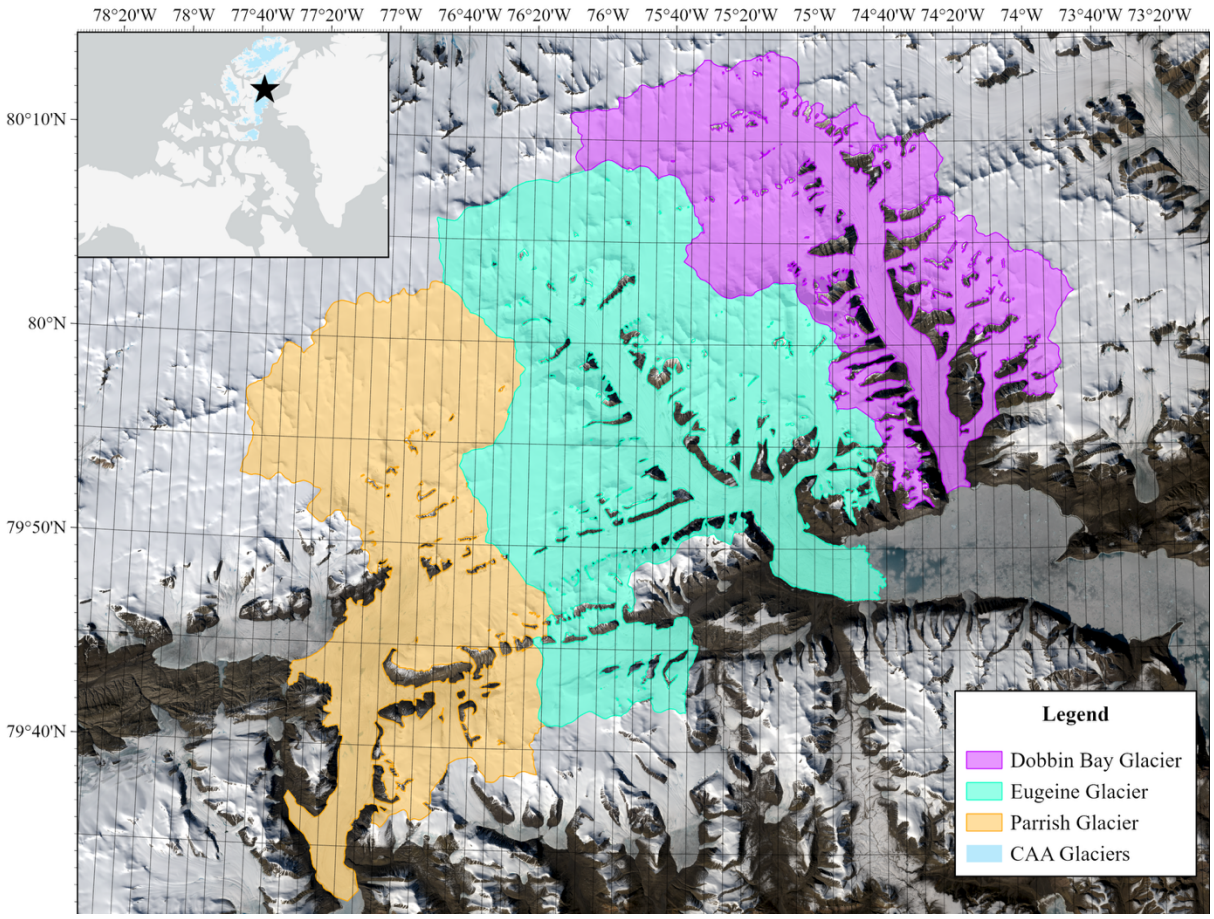


Figure 2-1: Study Sites Parrish Glacier, Eugenie Glacier and Dobbin Bay Glacier, pictured left to right (Landsat 8 imagery from June 2, 2019, in WGS 1984 UTM 18N). The top right inset map provides an overview of the CAA and includes all glacier bodies within the region, with the study site marked as a star. All glacier shapefiles were retrieved from the RGI consortium, 2023.

2.1.2 Pulse-Type Glaciers

All three study glaciers for this project have been included in previous regional studies, such as Copland et al. (2003) and Van Wychen et al. (2016). In Copland et al. (2003), Dobbin Bay Glacier and Parrish Glacier were both identified as possible surge-type glaciers, with no active phases observed. Dobbin Bay Glacier experienced "heavy terminus crevassing in 1959, a few small looped moraines and shear margins" (Copland et al., 2003). Parrish Glacier experienced "folding and shearing of surface moraines/ice bands over the terminus in 1959 and 1999" (Copland et al., 2003). Eugenie Glacier, however, was not identified as a surge-type by Copland et al. (2003). Van Wychen et al. (2016) revisited the work of Copland et al. (2003) by reanalyzing glaciers across the CAA and reclassified Dobbin Bay Glacier, Eugenie Glacier,

and Parrish Glacier, along with 4 other glaciers, as exhibiting some surge-type behavior, but they were distinct enough to warrant their own class. In Van Wychen et al. (2016), Dobbin Bay Glacier and Parrish Glacier were highlighted to show that these systems exhibit velocity variability only where the subglacial topography of the glaciers is below sea level, with velocity variability not occurring upglacier beyond this point.

These distinctions provided the contextual framework of the differences between surge-type and pulse-type glaciers within the region. Dobbin Glacier's main valley length is about ~30 km, and Eugenie Glacier's main valley length is ~40 km, with both terminating in Dobbin Bay. Parrish Glacier's main valley is about ~38 km long and ends in Copes Bay. Both Dobbin and Copes bays are smaller inlets that connect to the larger Baffin Bay. In terms of surface area, Dobbin Bay Glacier is the smallest at 660 km^2, followed by Parrish Glacier at 790 km^2, and Eugenie Glacier is the largest at 1 080 km^2. Eugenie Glacier has the widest terminus, at ~4.5 km, followed by Parrish Glacier, at ~2.5 km, and Dobbin Bay Glacier, with the narrowest terminus, at ~2 km.

2.2 Literature Review

To provide appropriate context and background information for understanding the irregular dynamics of the study glaciers, the following literature review first discusses typical glacier dynamics and mechanisms before covering irregular dynamics. First, the concept of glacier mass balance and balance velocities will be explained. Followed by a discussion on typical glacier motion and the effects of subglacial hydrology on motion. Finally, irregular dynamics will be understood by first explaining surge-type glaciers and the three theories of surge mechanics. All the current literature on "pulse-type" glaciers will then be covered, providing an understanding of how they differ from surge-type glaciers.

2.2.1 Glacier Mass Balance

Glacier mass balance is the accounting of all the processes that add and remove mass from a glacial system. Processes that add mass to the glacier system are categorized as ‘accumulation’ processes and include snowfall (and its redistribution), avalanching, the freezing of moist air onto the glacier's surface, among other typically minor processes (Figure 2-2). Mass is removed from glacier systems through ‘ablation’ processes, which include melt that runs off, sublimation and evaporation, among others (Figure 2-2). Additionally, for marine-terminating glaciers, frontal ablation occurs through melt at the water-ice interface and through iceberg calving. Accumulation processes tend to add mass that builds up in high-elevation regions of a glacier, resulting in these regions also being termed the ‘accumulation zone’, while lower elevations tend to have higher rates of ablation, resulting in these regions being referred to as the glacier’s ‘ablation zone’. Between these zones is the equilibrium line altitude (ELA), a zone of the glacier where accumulation and ablation processes are equal. Acting as a transitional marker, the ELA is defined by the altitude at which it occurs (Benn & Evans, 2013; Davis, 2020).

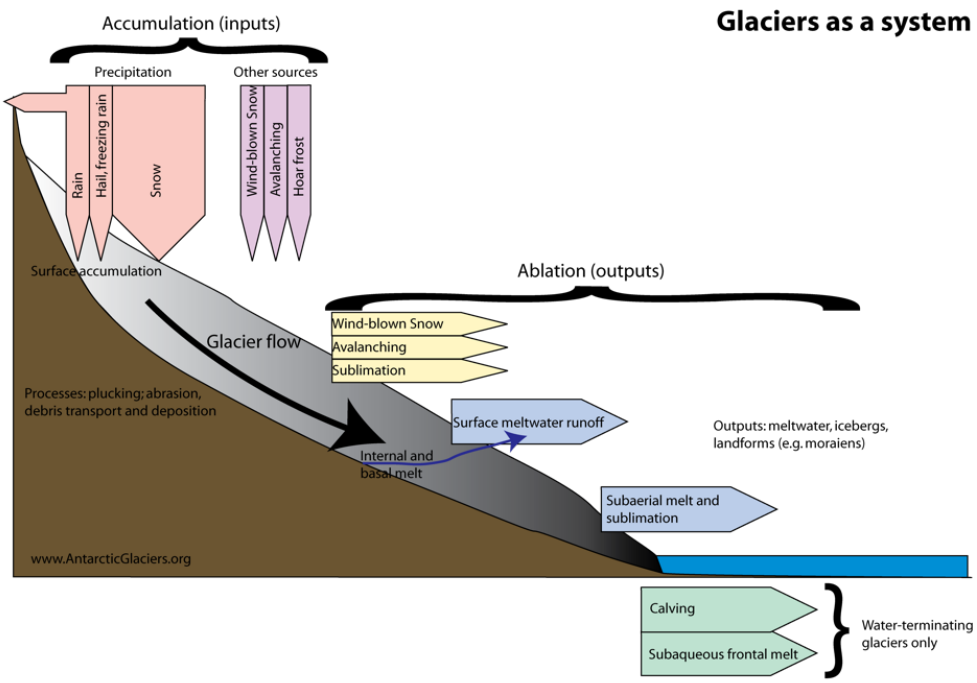


Figure 2-2: A summary of typical accumulation and ablation processes experienced within glacial systems. Accumulation processes occur at higher elevations, and ablation processes more often occur at lower elevations and at the glacier's terminus. (Davies, 2020)

The difference between accumulation and ablation over a specified period of time (typically one year) is referred to as a glacier's 'mass balance' (Benn & Evans, 2013). If accumulation exceeds ablation, the glacier experiences positive mass balance and grows. Conversely, when ablation rates exceed accumulation rates, the glacier experiences negative mass balance and recedes. Mass balance trends are both regional and seasonal, with neighbouring glaciers experiencing similar accumulation and ablation during the same periods. This is largely due to trends in air temperature and precipitation, with climatic factors influencing weather conditions on the glacier (Eisen et al., 2001). Seasonally, glaciers experience accumulation and melt seasons, which vary depending on location. Melt seasons are when the glacier experiences peak ablation, and accumulation seasons are when accumulation rates exceed ablation (Benn & Evans, 2013).

2.2.2 Balance Velocities

For glacial systems to persist, mass is redistributed from regions of accumulation to regions of ablation. As mass accumulates, mass moves downslope due to glacial motion processes (discussed in section 2.2.3). This movement of mass from the accumulation zone to the ablation zone effectively replenishes mass that is lost in low elevation areas (Benn & Evans, 2013). Balance velocities describe the rate of ice motion required for a glacier to achieve a steady state, meaning that how fast the glacier moves is a function of how much mass is added to the system (via accumulation processes) versus how much is lost (via ablation processes) (Figure 2-3).

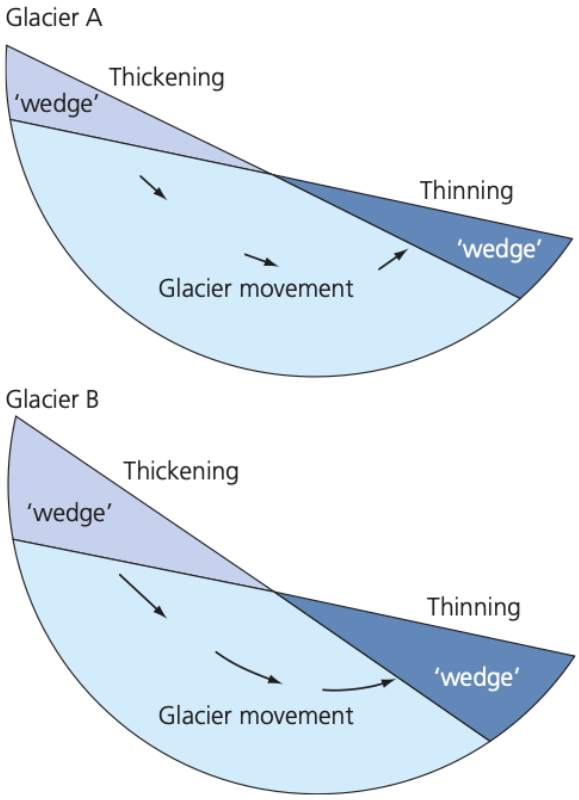


Figure 2-3: Balance velocity diagram. For a glacier to be in steady state, accumulation and ablation rates need to be equal. In this diagram, glacier A has low rates of ablation, meaning that less accumulation is needed, especially compared to glacier B, which needs higher rates of accumulation to match the higher rates of ablation. (modified from Sugen and John 1976)

Glaciers in cold, dry climates with low mass balance gradients only need slower balance velocities because less mass is being added to or lost from the system, meaning less mass needs to be redistributed. For glaciers in warm climates, higher balance velocities are generally

required for the glacier to persist because, as accumulation and ablation rates increase, more mass needs to be redistributed (Clarke, 1987; Benn & Evans, 2013). This relationship is exemplified in Figure 2-3, which shows balance velocities in an ideal steady state, with higher ablation rates requiring equal rates of accumulation.

Importantly for this thesis, glaciers that experience dynamic instabilities such as surge-type and pulse-type events do not flow at their balance velocities for reasons that are not well understood. In short, these glaciers typically flow at speeds slower than their balance velocities for long periods, followed by periods when they flow at speeds much faster than their balance velocities for a relatively short period.

2.3 Glacier Motion

Glacial motion occurs due to the wide range of force balance relationships found within glacial systems. Due to the large amount of ice mass within glacial systems, ice flows downward under gravity (Jennings & Hambrey, 2021). The immense weight of ice results in the glacier experiencing both stress and strain. Normal stress is a force applied perpendicular to the surface and occurs in glaciers due to the weight of ice on top of itself. Shear stress is a force that acts parallel to the surface and occurs when ice moves against itself or the surrounding bed or valley of the glacier.

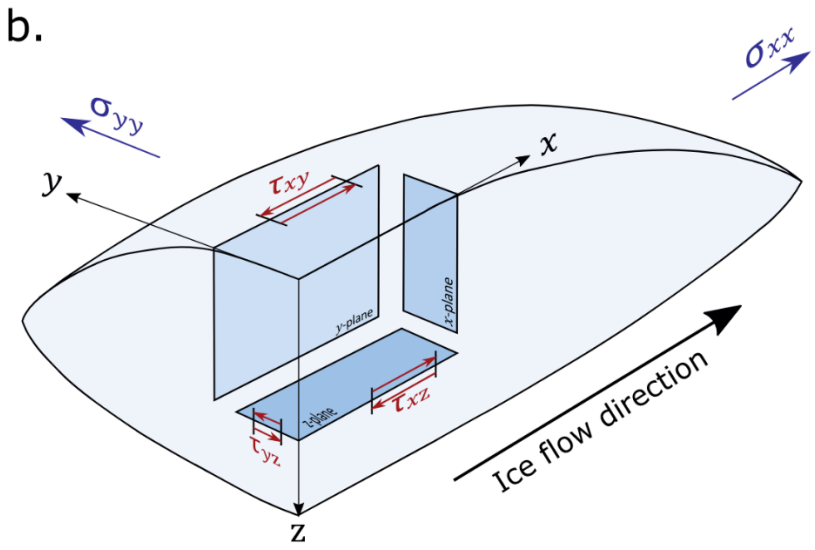


Figure 2-4: Conceptual diagram of glacier showing the main normal (σ) and shear (τ) stresses. Normal stress is shown in blue and shear stress is shown in red. Normal stress primarily drives ice flow, while shear stress both inhibits and encourages flow (Jennings & Hambrey, 2021).

Figure 2-4 shows an idealized view of the normal stress and shear stress that a glacier experiences. The glacier experiences strain in response to the applied stress on the ice. As force is applied, the ice undergoes strain in two primary ways: pure shear and simple shear. Pure shear is a flattening response in which the ice has experienced normal stress, resulting in compressive and tensile reactions. Simple shear, exemplified in Figure 2-5, is often compared to a stack of playing cards, in which material slides and rotates, affecting the material higher up the stack as strain occurs.

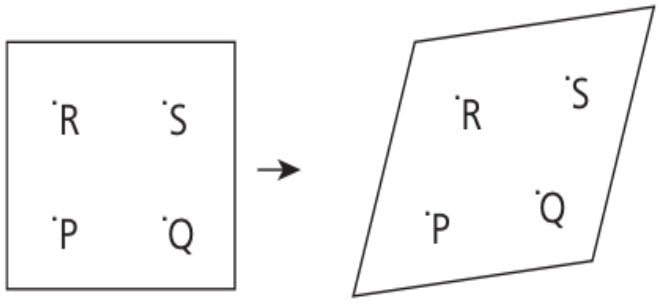


Figure 2-5: Diagram showing simple shear. Under simple shear, the square is skewed, with 'R and 'S sliding forward. While the shape of the square changes, its area is preserved, as it is neither squished nor stretched. (Benn & Evans, 2013)

Due to internal stress and strain within a glacial system, ice flows downslope. While there are various driving forces behind glacier flow, there also exists resistive stresses to the flow of the glacier. Resistive forces prevent the glacier from infinitely accelerating. The type of ice motion that occurs by this process is termed ice creep or internal deformation, and this form of motion is present on all glaciers. However, this is not the only way that a glacier can move; glacier motion can also happen when glaciers slip along their bed (known as sliding) or when the sediment beneath the glacier deforms and carries the glacier along with it (known as bed deformation). Figure 2-6 provides a schematic overview of each type of ice motion.

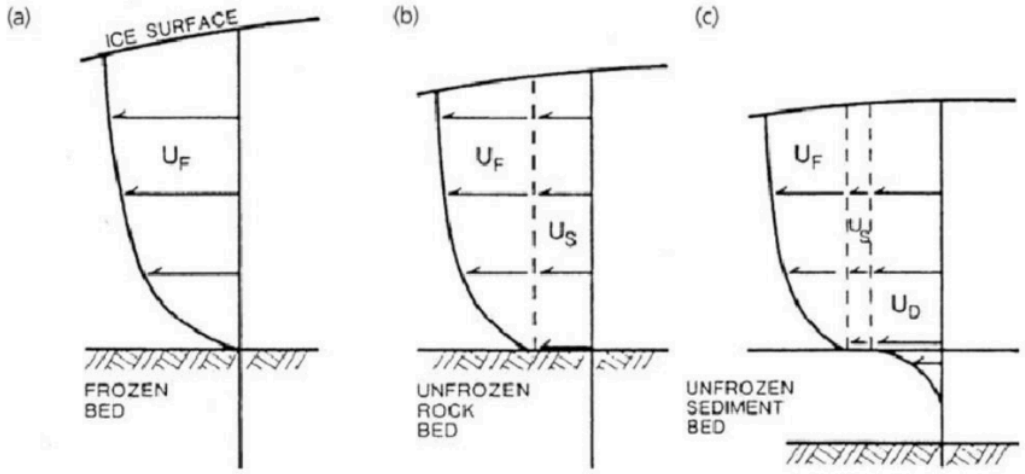


Figure 2-6: Diagram of glacier motion as a result of a) internal deformation, b) internal deformation and basal sliding, and c) internal deformation, basal sliding and bed deformation (Boulton 1996)

2.2.3.1 Ice Creep

Ice creep is a form of glacial motion which is present in all glacial systems and occurs as ice crystals that make up the glacier deform internally and flow past other crystals due to the stresses that the glacier experiences. Occurring in three ways, ice crystals either creep through cleavage planes, along crystal defects or experience recrystallization (Benn & Evans, 2013). Ice creep is described by Glen's flow Law (equation 1), which relates the internal strain of ice to the stresses being applied to it.

$$\epsilon = A\tau^n$$

Equation 1: Glen's flow law

The rate of creep (ϵ) is accounted for through: A - the condition of the ice, τ - the applied shear stress, and n - the creep component. A describes the crystal structure and is primarily influenced by temperature, but is also affected by factors such as water content, grain size, orientation, presence of impurities and hydrostatic pressure (Cuffey & Paterson, 2010; Benn & Evans, 2013). While more complex representations of ice creep exist in the literature, Glen's flow law provides a robust explanation of creep for the purposes of this thesis. This is often used throughout various glaciology purposes, even in modelling. (Benn & Evans, 2013)

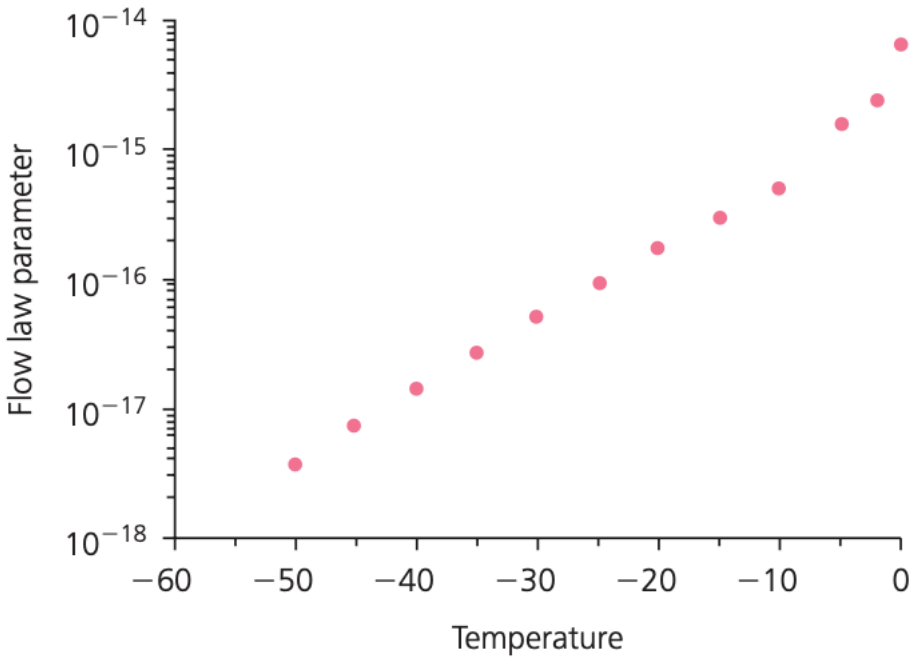


Figure 2-7: Variation in Ice flow law parameter A under the influence of temperature. As the temperature rises, flow rates rise. With variation in the linear relation occurring near the melting point. (Benn & Evans, 2013; Paterson, 1994)

Creep rates also vary locally within the glacier system, both throughout the ice column and laterally across the glacier. Throughout the ice column, ice is exposed to differing stresses and differing crystal conditions. Under these conditions, creep rates increase near the bed as internal deformation increases and ice temperatures approach the pressure-melting point. Near the glacier boundaries, such as valley walls, strain decreases because less internal stress is

present within the glacier due to a lower ice mass and because resistive stresses are greater (Jennings & Hambrey, 2021). Under this force-balance regime, creep rates are highest in the central flow of the glacier and decrease towards the margins. While creep rates are higher in warm glaciers, internal deformation is often the only form of motion found within cold, frozen to the bed glaciers. The total amount of motion that a glacier can experience due to ice creep processes is low, meaning that faster ice motion is facilitated when the glacier experiences either basal sliding or bed deformation.

2.2.3.2 Basal Sliding

Basal sliding occurs when the glacier slides along the bed (Earth's surface) beneath the glacier and occurs when water is present at the ice-bed interface. When a glacier is frozen to its bed, little to no sliding will occur. However, when water is present at the bed, sliding occurs with water essentially acting as a lubricant at the glacier base, allowing it to slide past obstacles. This is because water decreases contact between the glacier and the bed, reducing friction (Cuffey, 2013). Sliding is more common for temperate glaciers, where meltwater reaches the bed easily, but it also occurs on polythermal glaciers like those found in the Canadian Arctic.

Sliding occurs because of two processes: regelation and enhanced creep. Both mechanics allow ice to deform past objects located at the bed. Regelation is the process in which glacier ice builds up against the stoss side (upglacier section) of a bump (Figure 2-8). As pressure increases, melt is generated on the stoss side of the obstacle and water flows over the top and refreezes on the lee side (downglacier side). In this situation, heat transfer from the lee to the stoss side of the obstacle further facilitates melt on the stoss side. Regelation works most effectively on bumps smaller than 0.5 m.

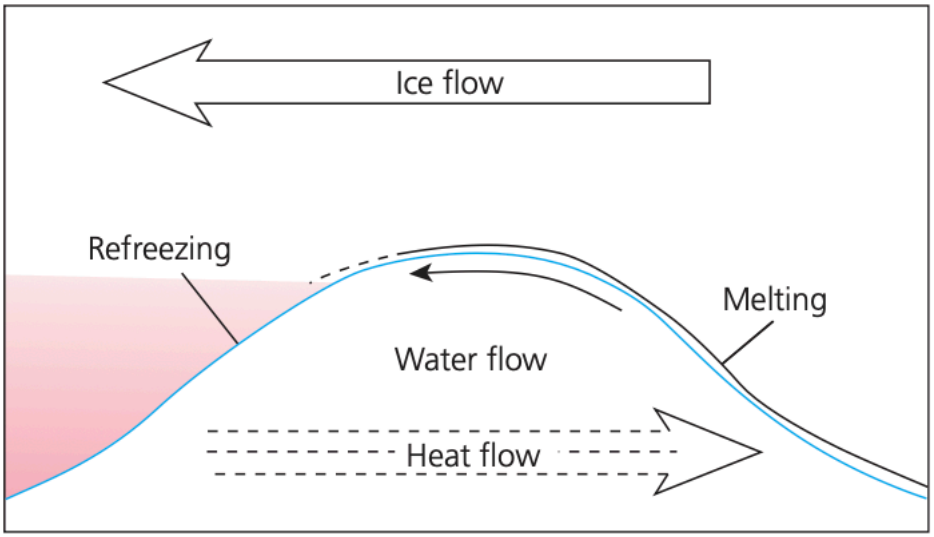


Figure 2-8: Diagram of regelation, ice builds up on the stoss side (right), leading to melt. Water then flows over the obstacle at the bed before refreezing on the lee side (left). The latent heat transfer from the transformation of water to ice further promotes the reglation process as energy transfers from the lee to the stoss side.(Benn & Evans, 2013)

Enhanced creep follows a similar process, where ice mass builds up against an object, but instead, the ice plastically deforms around the obstacle. This process follows the mechanics of ice creep (described in section 2.2.2.2). As previously described, internal ice deformation is driven through stress and ice condition. As ice is strained due to the driving pressure of its mass and the resisting stress of the object, strain increases, allowing for the deformation of ice to occur more easily. When ice is pressed up against larger obstacles (greater than 1 m), creep is enhanced (Benn & Evans, 2013; Cuffey, 2010). Due to the differing sizes of obstacles that regelation and enhanced creep function at, the greatest resistance to sliding is generated from objects that are between 0.5 and 1 m in size. While enhanced creep and regelation are studied on smaller scales underneath the glacier, it is important to remember the context of the whole system. Various sections of a glacier system are exposed to regions of high friction and areas where sliding processes are enhanced.

2.2.3.3 Bed Deformation

Bed deformation is a form of glacier motion in which the sediments beneath the glacier deform in response to the glacier's overlying mass. In this situation, the glacier moves because

it is carried along with the displacement of underlying unlithified sediments. For glaciers that have regions of their bed that are comprised of a loose consolidation of till, such as clay, silt or sand, this can be an important process. The bed deforms most effectively when this till becomes unfrozen, and water infiltration occurs (Benn & Evans 2013). As water infiltrates the till's pores, effective pressure decreases, allowing the till's grains to deform more easily. This allows for grains to flow more easily around itself and to deform more under the stress of the glacier (Benn & Evans, 2013), and this relationship is shown in Figure 2-6C. Along with low effective pressure, grain size and characteristics determine the rate of bed motion. With velocities increasing in systems with lower grain size (Benn & Evans, 2013), because the grain can more easily move past itself. Due to the need for low effective pressures within the till, this motion only occurs in polythermal or warm glaciers, which allow for water infiltration into the sediments.

2.2.4 Subglacial Hydrology Controls on Ice Motion

Water within glacial systems can greatly impact ice motion largely by reducing friction at the bed. This is most impactful in the case of basal sliding, which can be enhanced when there are greater volumes of water at the ice-bed interface. Increases in water at the ice-bed interface tends to vary seasonally, as surface temperatures increase and surface melt is generated, this

water can flow on top and through the glacier (the englacial system), carried through moulins and other englacial conduits, to the subglacial drainage network.

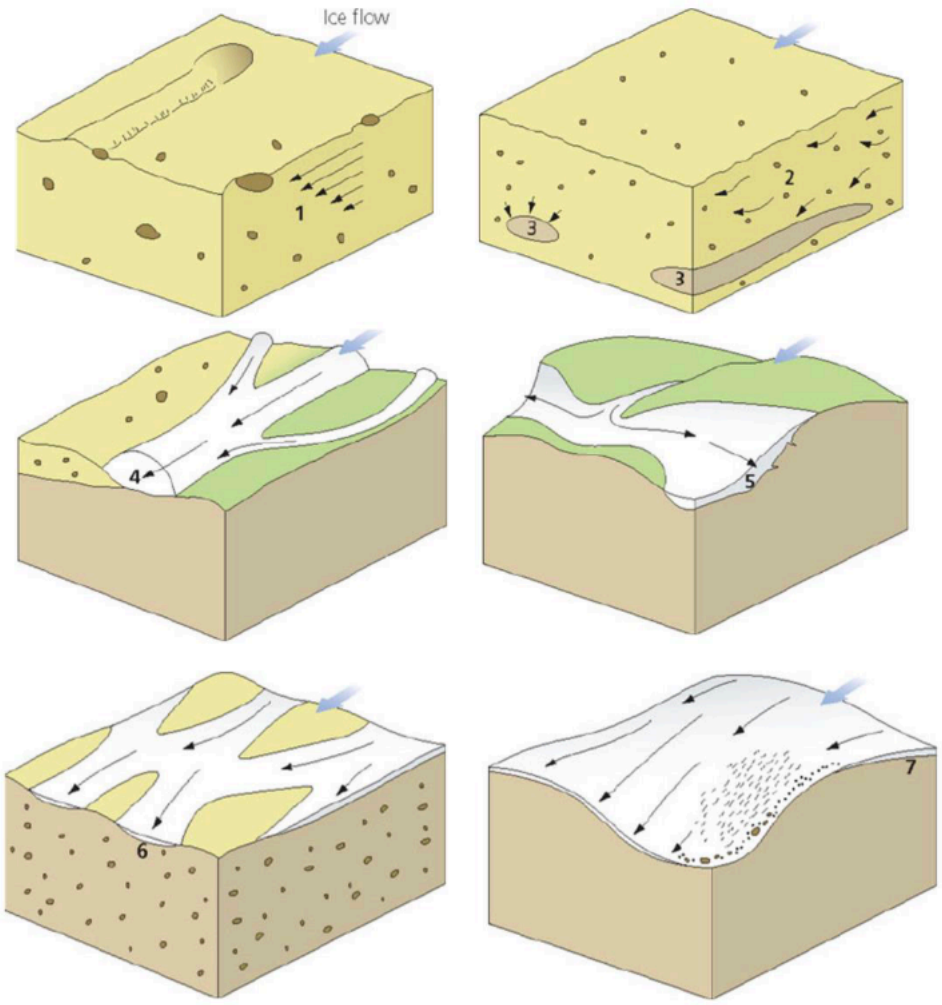


Figure 2-9: Different subglacial drainage configurations 1) water moving through a deformable till. 2) Darcian porewater flow. 3) Pipe flow 4) Dendritic network 5) Linked cavities. 6) Braided channels 7) Thin film. Configurations 3 and 4 are efficient channelized systems, while configurations 1, 2, 5, 6 and 7 are inefficient distributed systems (Benn and Evans, 2013).

Figure 2-9 shows various drainage networks which can occur at the bed. These networks are categorized into two groups: channelized systems and distributed systems. In a channelized drainage system, water is transferred efficiently through the subglacial network, with relatively negligible impacts on glacier motion. In distributed systems, however, water spreads out further, flowing in an inefficient manner and thus has a much larger impact on rates of glacier motion. Given this, subglacial drainage networks have a major impact on the flow speed of a glacier,

with distributed networks causing faster flow rates. This is because more water spends more time in the system, along with more of the bed being covered by water, which has a greater impact in terms of reducing friction at the bed. However, subglacial drainage networks are also dynamic, changing due to the amount of water flowing through the system and can evolve back and forth between efficient and inefficient networks.

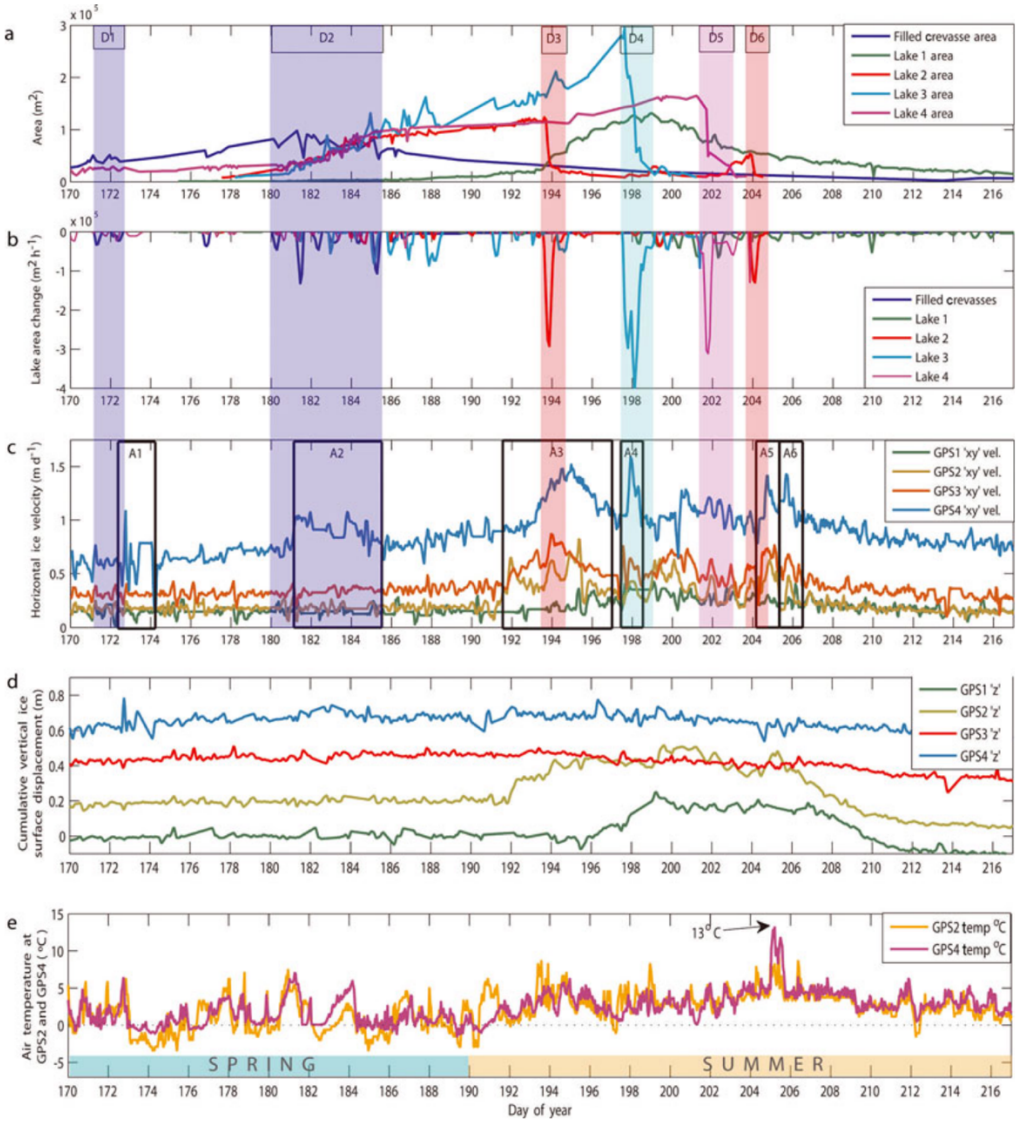


Figure 2-10: Graph of various observations on Belcher Glacier from day 170 (July 19th) to 217 (August 5th), 2009. (a) Area gain of lakes and water-filled crevasses. (B) Area loss of Lakes and water-filled crevasses, showing the rate of drainage at different lakes. (c) Surface ice velocity of four GPS systems. (d) Cumulative elevation change of GPS systems. (e)Air temperature at two GPS systems. Drainage events, where large patterns of drainage occur, are highlighted and annotated as D(x) through graphs a, b and c. Motion events are denoted in graph c as A(x). Retrieved from (Danielson & Sharp, 2013).

Figure 2-10 presents multiple measurements of the flow speed of Belcher Glacier throughout the 2009 melt season. Belcher Glacier is a marine-terminating glacier located in the

CAA on Devon Ice Cap, with the study from Danielson & Sharp (2013) identifying the 2009 spring from June 19th to July 9th and summer from July 9th to August 5th. Within the study, 4 GPS systems were placed along the main trunk of the glacier (GPS 1 at the head and GPS 4 at the terminus), monitoring the ice velocity and elevation change at each station, and air temperature at stations 2 and 4. Along with this, surface water storage features were identified and monitored throughout the melt season to determine the occurrence and rate of drainage events. Within the study, while most of the change in ice velocity was attributed to air temperature, fast drainage events early in the melt season were suggested to explain the initiation and enhancement of ice flow. Specifically, D3, which was a fast drainage of Lake 2, led to ice velocities across the glacier increasing past the rate explained by air temperatures. This velocity increase also occurred hours after the drainage event was recorded. Danielson and Sharp (2013) suggest that this led to increased meltwater reaching the bed in an inefficient drainage pattern, with the elevation of the nearby GPS systems rising. Drainage events later in the season, while transporting more water to the bed and increasing short-term velocity, did not lead to the same long-term increase in ice velocity. This is because by this time in the season, drainage networks most likely formed efficient networks, meaning that even though water was being transported to the bed of the glacier, it had little impact on flow speeds.

2.2.5 Dynamic Instabilities

Dynamic instabilities are a term used to describe rates of glacier motion that fall outside of what would be expected based on the glacier's mass balance conditions (i.e. the glacier flows at a speed faster or slower than its expected balance velocity). The most well-known and well-described type of dynamic instability is identified as 'surge-type' glaciers, while 'pulse-type' glaciers have also been identified; they have generally been little described in the literature. The following section provides an overview of 'surge-type' and 'pulse-type' glaciers, with an emphasis on their behaviors in the Canadian Arctic.

2.2.5.1 Surge-Type Glaciers

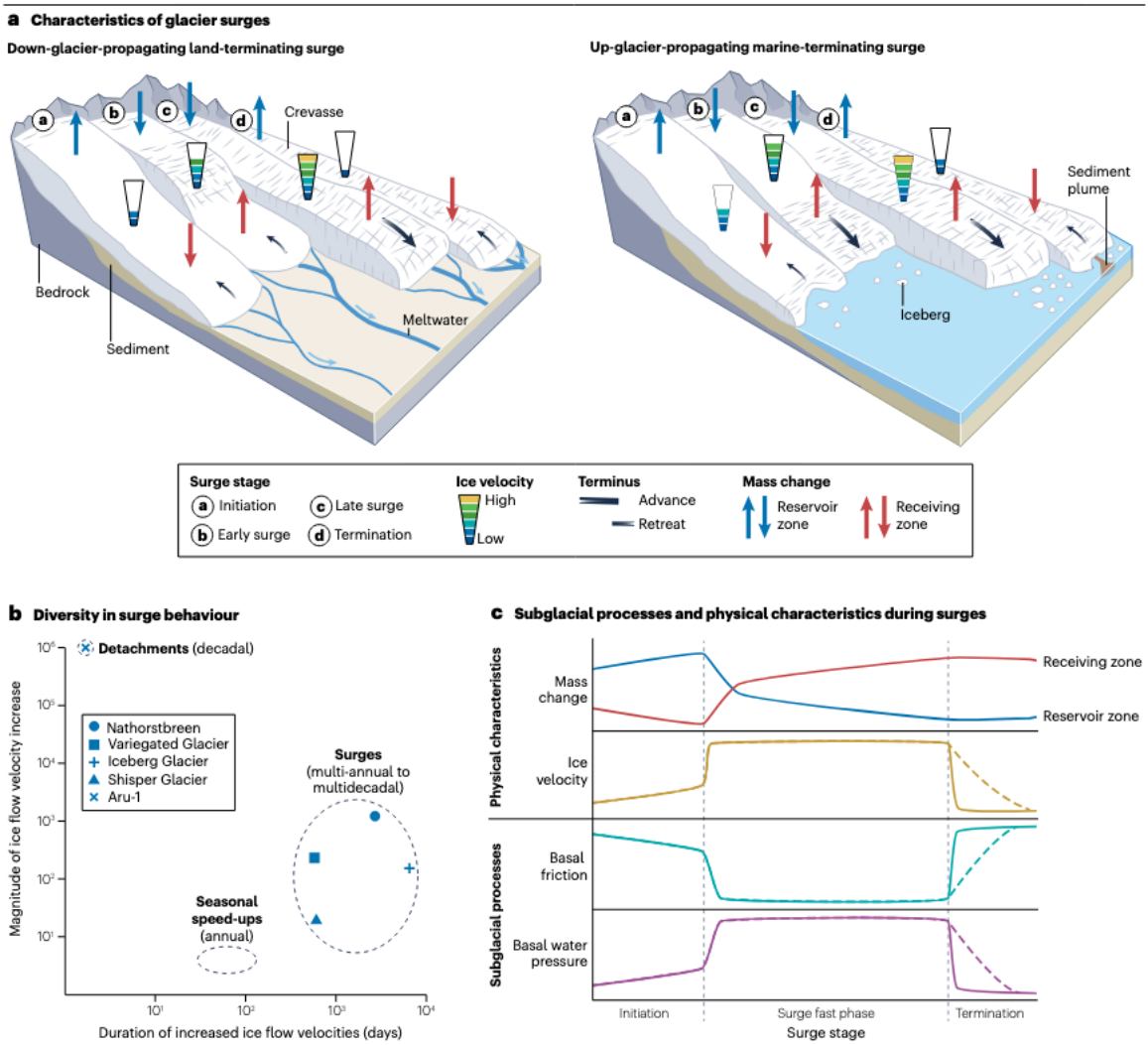


Figure 2-11: Various glacier surges and surge mechanics. a) Diagrams of both land- and marine-terminating surge-type glaciers undergoing various stages of surge processes. The land-terminating glacier is undergoing a downglacier propagating surge, while the marine-terminating glacier is experiencing an up-propagating surge. b) Conceptual diagram showing the differences and characteristics of various types of glaciers. Providing the magnitude of increase in velocity along with the duration of fast flow. c) A summary of the subglacial processes within surge-type glaciers. (Lovell et al., 2026)

Surge-type glaciers experience two different phases of glacier motion: a quiescent phase and an active phase. The quiescent phase is a period in which velocities are much slower than they should be based on balance velocity and is characterized by mass build-up in the accumulation region and depletion in the ablation region (Figure 2-11). As seen in Figure 2-11a, during the active phase, velocities increase substantially (10 to 1000 times), leading to mass transfer downglacier, either to the ablation zone in a down-propagating surge-type glacier

or further extending the terminus in an up-propagating surge-type glacier (Raymond 1987, Benn and Evans 2013; Lovell et al., 2026). Figure 2-11b further shows differences in surge-type activity, including the magnitude of acceleration across glaciers and the length of the active phase. In terms of geometric changes, following the initiation of a surge, the upper regions of the glacier begin to thin as mass is transferred downglacier, resulting in surface elevation gains at low elevations and terminus extension (Figure 2-11). The active and quiescent phases occur on a bimodal cycle, with the cycle being of largely consistent length for a single glacier. The length of a cycle has also generally been found to be similar between surge-type glaciers in similar climates. In warmer climates, quiescent phases last from ~35-40 years and active phases from ~1-4 years. In colder climates, phases are longer, with quiescence lasting ~50-100 years and active phases lasting from 7-15 years (Van Wychen et al., 2016; Lovell, 2026).

While much research has been done on surge-type glaciers and uncovering surge mechanisms, direct causes have yet to be proven, with the two prevailing theories being the Hydraulic/Alaskan theory and the Thermal/Svalbard theory. In the hydraulic model, surge activity is hypothesized to be driven by changes in the drainage system at the glacier bed. During quiescence, the drainage network configuration causes bed water pressure to rise and eventually initiate a surge. Kamb (1987) theorized that the link cavity configuration (Figure 2-9, configuration 5) was most likely the cause of these surges, with cavity channels collapsing and leading to large water influxes released across the bed.

The thermal model argues that surge activity is caused by the thermal condition of the bed changing from frozen to unfrozen. As ice builds up during the quiescent phase, pressure at the bed increases, driving ice creep and generating heat, which in turn creates meltwater that becomes trapped at the bed. Over time, this water either allows greater sliding to occur or enables the bed sediments to transition from frozen to unfrozen (Benn & Evans, 2013). In either

case, friction at the bed is decreased and glacier velocities increase, leading to the activation of a surge event. As the surge event progresses, ice thickness in the region where it initiated decreases, leading to a decrease in bed pressure and the surge's termination. This allows the glacier to start building up mass for the next surge.

Both the hydraulic and thermal models are believed to be more relevant in different climatic regions, with the hydraulic model being more likely to occur in warmer climates and the thermal model being more relevant in colder climates. In an attempt to provide a unifying theory to surging, the enthalpy model has been suggested. The enthalpy model, introduced in Sevestre & Benn (2015) and further discussed in Benn et al. (2019), frames the discussion of surge-type glaciers in terms of the disparity between the energy built up and evacuated from within a glacial system and the rate at which this happens. With the controls of enthalpy within a glacier being the: climatic properties, geometric properties and bed properties. In a stable or non-surge system, enthalpy is built up and evacuated at a steady state, which effectively means that the glacier will flow at its balance velocities. However, in a non-stable or surge-type glacier, energy buildup exceeds the glacier system's capacity to remove energy during the quiescent period. Eventually, too much enthalpy is at the bed ice interface, leading to reduced effective pressure, enhanced basal motion and a glacier surge.

2.2.5.2 Pulse-Type Glacier Dynamics

Pulse-type glaciers in the Canadian Arctic, which were originally defined in Van Wychen et al. (2016), experience irregular dynamics similar to surge-type glaciers but with some key differences. Like surge-glaciers, pulse-type glaciers experience a quiescent phase of slow velocity and mass build-up and an active phase of increased velocities as the built-up mass moves to the terminus (Lovell et al., 2026). However, pulse-type glaciers primarily experience this activity in their terminus region, and largely where the glacier bed is grounded below sea level (Van Wychen et al., 2016).

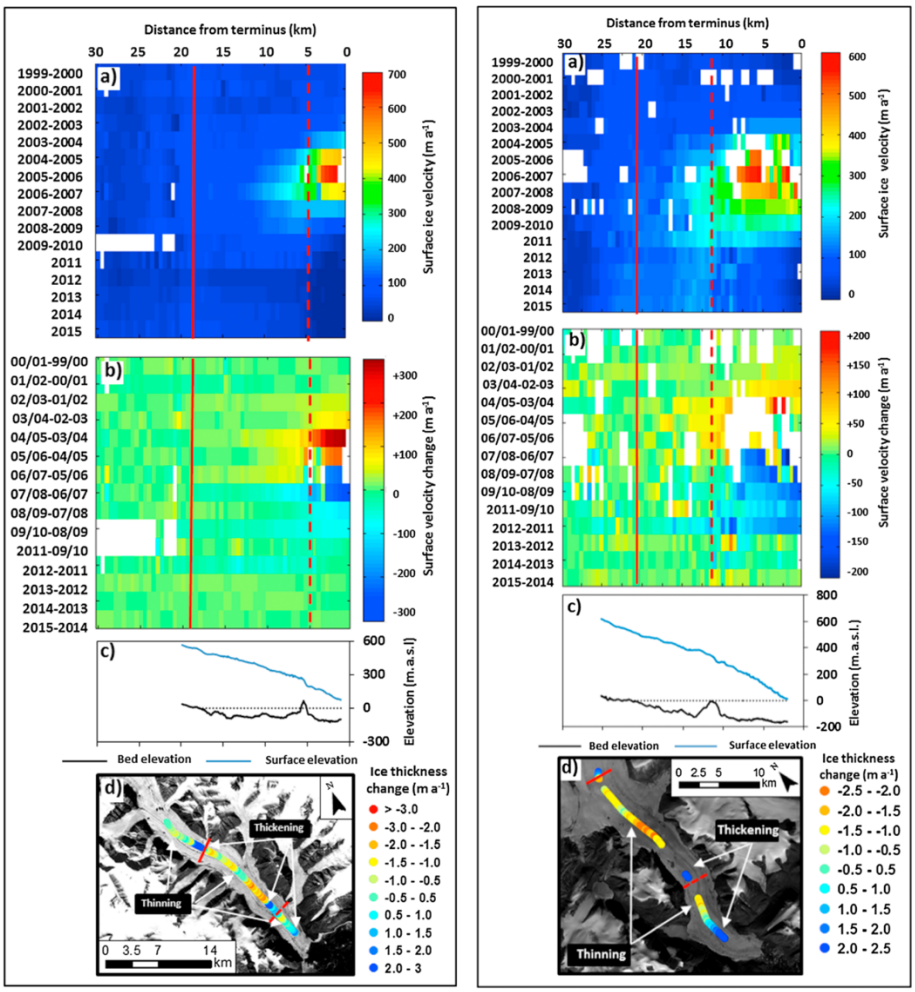


Figure 2-12: Centerline surface velocity, bed topography and elevation change of Dobbin Bay Glacier (left) and Parrish Glacier (Right) (Van Wychen, 2016).

From comparisons of bed elevation and ice thickness of Dobbin Bay and Parrish Glacier (Van Wychen, 2016), as shown in Figure 2 -12, it was found that prominent subglacial ridges exist within these terminus regions. These subglacial obstacles were suggested to be important pinning-points that increase basal friction, leading to compressive ice flow and localized ice thickening, which was important for pulse initiation. Another major difference is that surge-type glaciers typically experience velocity variation along a much longer portion of the glacier system. Despite the identification of this process in Van Wychen et al. (2016), there has been limited research on pulse-type glaciers since then.

Chapter 3 Methodology

This section of the thesis describes the datasets and methodologies used to investigate pulse-type activity on Dobbin Bay, Parrish and Eugenie glaciers. This study takes a remote sensing-based approach, which allows for a multiyear spatial and temporal comparison between the active and quiescent phases of all three study glaciers to be undertaken. Each of the datasets and methodologies outlined in this chapter contributes to the overall research objectives of the thesis.

3.1 Glacier Elevation Change

One approach to quantifying glacier elevation change involves comparing surface elevations of successive Digital Elevation Models (DEM) and measuring where and when (or if) elevation change occurs. This practice is commonly used within the field of glaciology to estimate surface mass balance conditions, with the work of Hugonnet et al (2021) providing an example of this method at the global scale <https://www.theia-land.fr/en/blog/product/rate-of-glacier-elevation-changes-from-2000-to-2019/>. However, DEM differencing can also be used to identify irregular glacier dynamics and map where mass is redistributed during surge or pulse events (Van Wychen et al 2022; 2025). This thesis uses DEM differencing to map the volumetric redistribution of ice for the three study glaciers. Additionally, the use of time-stamped DEMs also allows one to determine when surge or pulse events occurred. This thesis utilizes openly available ArcticDEM StripMap products processed with the XDEM Python package to determine elevation change.

3.1.1 ArcticDEM

ArcticDEM is an open-use archive of DEM products created and distributed by the University of Minnesota's Polar Geospatial Centre (Porter et al., 2022)

<https://www.pgc.umn.edu/data/arcticdem/>. ArcticDEM products are derived from panchromatic optical imagery collected by the Maxar satellite constellation (Porter et al., 2022). This process uses stereo image pairs to derive elevation by triangulating ground points. Using the satellite's positions and viewing angles, the scene's parallax of points is calculated, allowing their elevations to be derived through triangulation. (Porter et al., 2022). Unlike other methods of DEM creation, such as deriving elevations from LiDAR and SAR products, stereo image pairs are susceptible to poor weather and cloud cover, which can obscure the Earth's surface. While these limitations exist, ArcticDEM provided high-resolution, multi-year elevation products across the Canadian Arctic from 2010 to 2024.

The Polar Geospatial Centre distributes two types of ArcticDEM products: StripMap products and Mosaic products. StripMap products are derived from the single stereo pair acquisition obtained by the optical sensors. Each ArcticDEM StripMap product is time-stamped and can be obtained with a resolution of 2 m. The mosaic product is an amalgamation of data from corrected StripMap products, providing a continuous representation of surface elevations but without a specific timestamp.

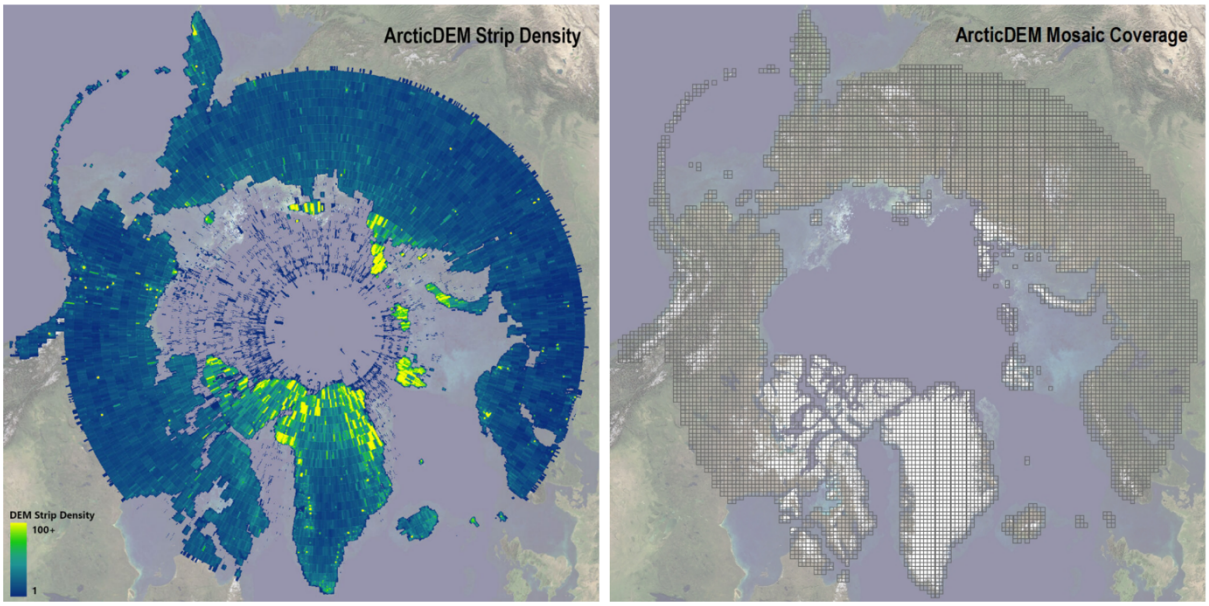


Figure 3-1: ArcticDEM's spatial coverage of DEM products across the Arctic. The left image shows the density of StripMap products throughout the Arctic, highlighting areas of high temporal coverage in yellow and low temporal coverage in blue. The right image shows the coverage of mosaic products across the Arctic. (Porter et al., 2022)

As shown in Figure 3-1, both products provide coverage across the Arctic. The Mosaic product has continuous coverage, whereas the StripMap products have varying density in their spatial coverage. Due to their temporal preservation, the StripMap DEMs were selected for this thesis to allow for change to be monitored over time.

In total, 44 DEM strips were used out of the total 603 DEM strips that covered one of the three glaciers. DEMs were selected for use based on the strip's coverage and quality. For coverage, a DEM had to be centred on the main trunk of the observed glacier to maximize glacier coverage in a single scene. In terms of quality, DEMs were first selected based on the valid area percent attribute of the strip. This attribute is calculated based on the ratio of data pixels in the DEM that are marked as match points by the SETSM analysis, thereby excluding cloud cover, shadows, water bodies, and low-texture surfaces. In years of dense strip coverage, only strips above 90% were selected for further analysis. Finally, the scenes were qualitatively analysed for errors present within the study site. Errors are typically noticeable due to erratic changes in elevation, as shown in Figure 3-2. Finally, one DEM was selected per year.

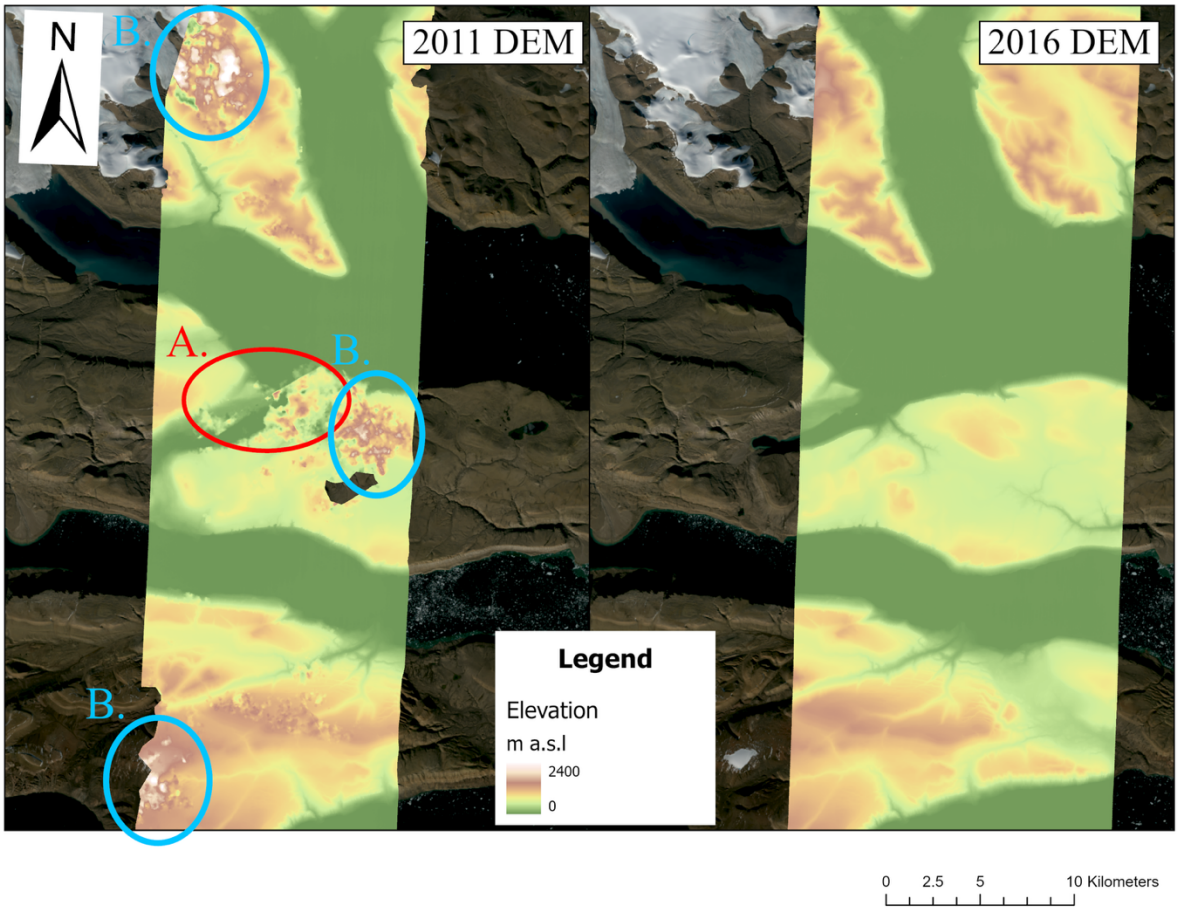


Figure 3-2: Shows two DEM products south of Parrish Glacier, with two different errors highlighted in the DEM collected on June 25, 2011 (left), that are not present in the DEM collected on March 20, 2016. A. shows a combination of cloud cover errors combined with a processing error. The processing error manifests in an unnatural straight line. B. shows various examples of obscuring weather features like clouds. These features suggest erratic, sharp rises in elevation that are unlikely to be present in the topography. For these reasons and given the absence of these features in the 2016 DEM, features A and B are identified as errors.

3.1.2 XDEM

XDEM is a Python package that performs georeferencing, co-registration, differencing and other operations on DEM products. Currently, the package's development is led by CNES (the French space agency), with funding from NASA and SNSF (Swiss National Science Foundation). For the purposes of this thesis, the XDEM package was used to co-register two DEMs and then compute the normalized elevation difference between them. Co-registration of DEM products is performed to reduce x- and y-offsets between two DEM scenes, ensuring that, as much as possible, the same location is represented in both DEM captures. When DEM scenes without co-registration are overlaid, slight offsets are observed between the x-, y- and z-values,

which can cause artificial surface elevation changes to be determined when the products are differenced.

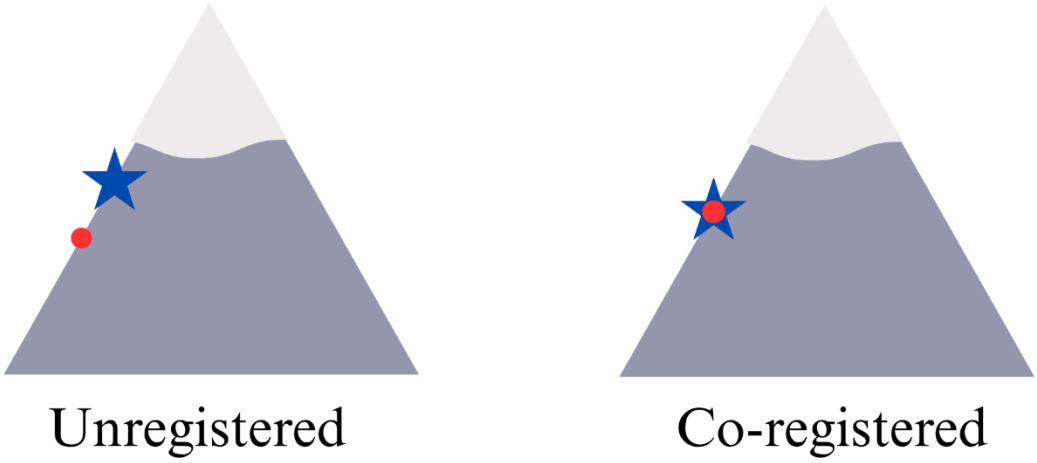


Figure 3-3: A diagram of the importance of co-registration in DEM products when comparing elevation. In the unregistered diagram, the DEM sees the circle and the star as the same point, leading to the elevation on bedrock being two different values. But when the co-registered offset between x and y values is reduced, leading to the bedrock having the same elevation (derived from Nuth and Kääb, 2011)

As seen in Figure 3-3, the elevation difference between unregistered products leads to inaccurate comparisons of topography, even though the points are meant to represent the same spot. Through the co-registration of DEMs, these points become more aligned. XDem supports co-registration via various methods, but for this project, the Nuth and Kääb method was chosen due to its widespread use in glaciology (Nuth and Kääb, 2011; Sevestre et al., 2018; Hugonnet et al., 2021). This method analyses the slopes across stable terrain and compares the scene's elevation, slope, and aspect to calculate the horizontal shift between DEMs. This statistical analysis is performed iteratively across the scenes until the horizontal shift is within an acceptable range throughout each scene's stable ground area.

For this project, a custom script was written to perform elevation difference *en masse*. The script DEM_DIF.py effectively wraps the XDEM code, allowing the user to drop data into subdirectories within a single directory for data processing (the three subdirectories are named: 'input', 'mask', and 'ref_dem'). The input directory contains all the DEM products that the user wants to be differenced. The mask directory contains a mask shapefile of unstable ground,

including ocean and glacier areas, which ensures that the co-registration process of the DEM products only uses stable areas to build the model used for correction. The mask shapefile was created by combining a glacier-extent shapefile for the Canadian Arctic (in this case, from version 7 of the RGI) (Pfeffer, 2014) and the NSIDC Arctic Ocean shapefile (Meier, W. N. & Stewart, J. S, 2023), thereby improving accuracy and runtime by removing areas not viable for co-registration from the process. The ref_dem directory contains a reference DEM of the study selected by the user. The reference DEM serves as the singular DEM that all the other DEMs are referenced to and was selected based on providing the greatest amount of overlap with all the other DEM files. DEM_DIF.py first adjusts the reference DEM, which is resampled bilinearly to the desired scale, and then reprojected to the relevant UTM projection. For this thesis, a resampling of 20 m was used. Due to the location of the study site, the DEMs were re-projected into the WGS 84 / UTM 18N datum. Once the ref_dem is prepared, all DEMs in the input folder are resampled and reprojected to match the reference DEM's parameters. Once all DEMs are prepared, they are co-registered to the reference DEM using the Nuth and Kääb method, with the XDEM co-registration function: *xdem.coreg.NuthKaab()*. Finally, the co-registered DEM products are sequentially differenced, yielding an annual elevation difference over the glacier. Along with annual difference products, two additional statistical reports are made: a metadata text file and a graph of the statistical spread of data (graphs presented in the Appendices). These reports provide the uncertainty and viability of the differenced products, including the mean, median, standard deviation, and Normalized Median Absolute Deviation (NMAD). To evaluate uncertainty, the median and NMAD were used as metrics rather than means. The reason that means were discarded when considering the dataset's uncertainty is the presence (at times) of large outliers that skew the mean error statistics, leading to misrepresentations of the data's spread. Using median and NMAD, the spread and average values provide more robust reporting of uncertainty (Hugonnet et al., 2021).

3.2 Velocity Variability

One way to derive surface ice velocity from remote sensing is to track the displacement of the glacier surface between successive SAR or optical images. Put most simply, surface ice features are identified and tracked between two images. Then, using the time between image acquisition and the distance travelled by the identified objects, the ice's velocity is derived. The global collection of satellite imagery has enabled large-scale analysis of glacier ice velocities worldwide (Gardner et al., 2025). Both SAR and optical image surface tracking products were performed within this study. Due to temporal availability, surface ice velocity was measured primarily through optical images for this study. This thesis then used ice velocity measurements to map dynamic changes in ice flow over the study period.

3.2.1 ITS_LIVE Optical Velocity Processing

Surface ice velocity products were obtained from ITS_LIVE, https://its-live.jpl.nasa.gov/>, a remote sensing data processing service created by NASA's Jet Propulsion Laboratory (JPL) that freely disseminates glacier velocity products derived from select optical and synthetic Aperture Radar (SAR) datasets to the community (Gardner et al., 2025). More specifically, ITS_LIVE produces surface ice velocity using Landsat 4, 5, 6, 7, 8, and Sentinel-2 optical images and Sentinel-1 SAR data using the autonomous Repeat Image Feature Tracking (autoRIFT) algorithm. While data from ITS_LIVE spans 1985 to 2023, many regions lack coverage for the full timeframe, with global, annual coverage available following the launch of Landsat 8 in 2013. Due to scanline errors present within Landsat 7's later years, the introduction of Landsat 8 enabled more consistent global acquisition and improved return times (Gardner, 2025).

AutoRIFT derives surface velocity across a glacier by calculating the displacement of pixel groups of the glacier. This is done by dividing the glacier into 16 x 16 or 32 x 32-pixel

chips. Once created, the pixel chips are compared against a successive image using a normalized cross-correlation (NCC) algorithm to find the strongest match. Once matches have been completed, they are filtered using a normalized displacement coherence, removing matches that are low confidence or spatially incoherent. The possibility of the match is evaluated further by using reference velocity plots to estimate if a chip could have moved the distance it did. Finally, once the velocity of chips across the glacier has been calculated, the velocity of patches are combined into a single raster, providing the ice velocity across the glacier (Gardner et al., 2018, 2025).

While ITS_LIVE offers both image pair and annual surface velocity products, the annual products were selected for this project. Image pair products provide the calculated velocity of image pairs, which gives a more temporally precise estimate of surface ice velocity. However, annual composites lower the influence of noise and errors and are sufficient for the long-term detection of dynamic changes that are needed for this thesis. At the time that the analysis of this thesis was undertaken, annual data for the Canadian Arctic was available from 1999 to 2022, with individual image pairs also being available for download. For the purposes of this thesis, pre-derived annual velocity products were used to gain a comprehensive understanding of the changing velocity structure of the identified glaciers over the study period.

3.2.2 ArcGIS Pro Post Processing

Following the download of annual ITS-LIVE composites for the Canadian Arctic, the glacier velocity geotiffs were clipped to the extents of Dobbin Bay, Eugenie and Parrish glaciers. Glacier boundaries were obtained from the Randolph Glacier Inventory (RGI), a shapefile-based inventory of approximately 198 000 glaciers worldwide (Pfeffer, 2014). The RGI is a community-driven initiative to map glacier extents and is commonly used throughout the glaciological community (Pfeffer et al., 2014). Maps of the annual velocity structure were first created in ArcGIS Pro, allowing exploration of spatial and temporal changes in glacier

dynamics across all glaciers to be made. For a more quantitative analysis of dynamic change, glacier centerlines were manually drawn in ArcGIS to approximate the flow of the main trunk of each glacier. These were then used to extract centerline velocities, which could then be plotted to visualize variability over time. Comparison of glacier velocities extracted along a centreline is a common practice in glaciology to investigate spatial and temporal variations in ice motion (Van Wychen et al., 2016; Dalton et al. 2022). The centrelines were drawn as 'polyline' shapefiles, which were then converted to a series of point locations placed every 100 m along the centreline starting at the glacier terminus and moving upglacier. To extract glacier velocities, the 'Extract Multi Values to Points' spatial analyst tool within ArcGIS Pro was utilized. This tool automatically extracts the underlying pixel values from all input raster datasets and appends them to the shapefile's attribute table.

3.2.2 TerraSAR-X & TanDEM-X Velocity Processing

TerraSAR-X is an X-band Synthetic Aperture Radar (SAR) satellite launched by the German Aerospace Center (DLR) in 2007. TanDEM-X is a twin satellite to TerraSAR-X, which closely follows the same orbital track as TerraSAR-X but was launched three years later in 2010 (also by DLR). Both satellites orbit at a height of ~514 km with a repeat orbit period of 11 days, with TanDEM-X following around 250-500 m behind TerraSAR-X. TerraSAR-X and TanDEM X both provide options for data collection in all four polarizations (depending on beam mode), HH/VV/HV/VH. All data for this project were obtained with HH polarization. There are three main beam modes for both sensors: StripMap Mode, Spotlight Mode, and ScanSAR Mode, with all having different resolutions. TerraSAR-X/TanDEM-X and other SAR sensors/products have been widely used throughout the glaciology community for glacier velocity mapping (and other applications). TerraSAR-X data is used in this study because of research partnerships within DLR that have facilitated the regular data collection over the study sites.

Offset tracking of SAR images is a widely used method within the glaciology community for deriving glacial ice velocity. This process uses SAR datasets to identify and track the offset of unique speckle patterns returned from a glacier surface. As the glacier flows, the near-surface conditions of the glacier are unchanged, and the speckle pattern is preserved, allowing recurring SAR images of a glacier to be used to infer ice motion. Surface velocity is derived using the time between acquisitions and the tracked displacements of the speckle patterns between images. In this study, offset tracking is performed using the Gamma RS software which is a software commonly used to derive ice velocity (Schellenberger et al., 2016, Lauzon et al., 2023). This methodology was only performed over Parrish Glacier from 2022 to 2023 due to time and data restraints but allow for the validation and alignment of findings between TSX processing and the more expansive ITS-LIVE velocity records.

3.3 Terminus Position Mapping

Terminus position mapping can be used as an indicator of irregular glacial dynamics, such as surge- and pulse-type processes (Copland et al., 2003; Dalton et al., 2022; Main et al., 2023). Given that activation of a surge or a pulse event typically involves the redistribution of mass from upper to lower elevations, these events are commonly linked to the rapid advance of the glacier terminus over a short period (Copland et al., 2003; Lauzon et al., 2023). Conversely, during the quiescent phase, when mass is being restricted from being moved down the glacier, the terminus position often retreats more than what would be expected from surface mass balance processes alone. Given this, the tracking of terminus position can be used to constrain when surge and pulse events may have occurred, and because of the relatively wide availability of different remote sensing optical products, such as Landsat, SPOT and Aster imagery, this analysis can be used to expand the temporal understanding of dynamic instabilities for the three study glaciers.

3.3.1 Optical Imagery Collection

Various optical panchromatic and true-colour images of the study sites were used to delineate the position of each glacier's terminus, including satellite imagery from the ASTER, SPOT, and Landsat sensors, as well as historic aerial photographs from the Government of Canada, provided by Cook et al. (2019).

Table 3-1: Description of the satellite imagery used to delineate terminus positions.

Dataset	Spatial Resolution	Temporal Coverage Used	Approximate Uncertainty	Source /URL
Air Photo	~5 m	1959	5 – 15 m	(Cook et al., 2019), available from the National Air Photo Library
Landsat 1	60 m	1975 – 1977	60 – 180 m	U.S geological Survey (USGS) Earth Explorer <https://earthexplorer.usgs.gov/>
Landsat2	60 m	1979 – 1981	60 – 180 m	U.S geological Survey (USGS) Earth Explorer <https://earthexplorer.usgs.gov/>
Landsat 3	60 m	1982	60 – 180 m	U.S geological Survey (USGS) Earth Explorer <https://earthexplorer.usgs.gov/>
SPOT	20 m	1987 – 1996	20 – 60 m	CNES, 2024. SPOT world Heritage archive <https://regards.cnes.fr/html/swh/Home-swh3.html>
Landsat 7	30 m	1999 – 2012	30 – 90 m	U.S geological Survey (USGS) Earth Explorer <https://earthexplorer.usgs.gov/>
Aster	30 m	2004 - 2011	30 – 90 m	NASA Earth data, 2024 <https://www.earthdata.nasa.gov/data/instruments/aster>
Landsat 8	30 m	2012 - 2024	30 – 90 m	U.S geological Survey (USGS) Earth Explorer <https://earthexplorer.usgs.gov/>

Across all datasets, images were first filtered for site coverage, with the search boundaries set to the terminus of each glacier. Following the launch of Landsat 8 in 2012, larger amounts of imagery were available for the study sites, allowing for a temporal filter from March to April to be applied as well as a cloud coverage filter of 15%. Finally, before delineation, scenes were qualitatively checked for error across the terminus. Common errors include dead pixels and similar sensor errors found more prominently in pre-2000 imagery, with scanline

errors being present most commonly in Landsat 7 scenes following 2003. While these datasets could make interpretation difficult, exceptions were made for images that showed sections of the terminus.

Following the image selection and collection, the images were projected into the WGS 1984 UTM Zone 18N coordinate system. Images were then georeferenced to a common 2019 Landsat 8 image (multispectral_LC08_L1TP_048002_20190702_20200830_02_T1_MTL), which includes all the study sites along with sufficient surrounding topography. Various polynomial orders were used to georeferenced images for delineation, based on the sensor from which the image was acquired. For Landsat 8 images, only a zero-order polynomial was applied using 1 GCP, as the products were collected with the same sensor and processed similarly. A zero-order polynomial was also applied to the historic aerial photography, as the products used were already orthorectified in Cook et al. (2019). Second-order polynomials were used to transform historic Landsat imagery, being images captured from Landsat 1-3 and Landsat 7, with 6 GCP's being used. Finally, third-order polynomials were applied to SPOT and ASTER products due to different sensor specifications. For images from these product sensors, 10 GCPs were placed throughout the scene to ensure an alignment of the terminus of each glacier.

3.3.2 Terminus Position Delineation

Terminus positions were delineated on all collected images in ArcGIS Pro 3.4.1 (Table A-1), where a multiline shapefile was created for each study site. Georeferenced images were then imported, and a new attribute was created in the multiline shapefile to represent that terminus delineation. The terminus was then manually mapped with points placed every ~100 m or where the terminus experienced a change in geometry, which required greater point density. In tracing the terminus, various scales were used based on image clarity and resolution.

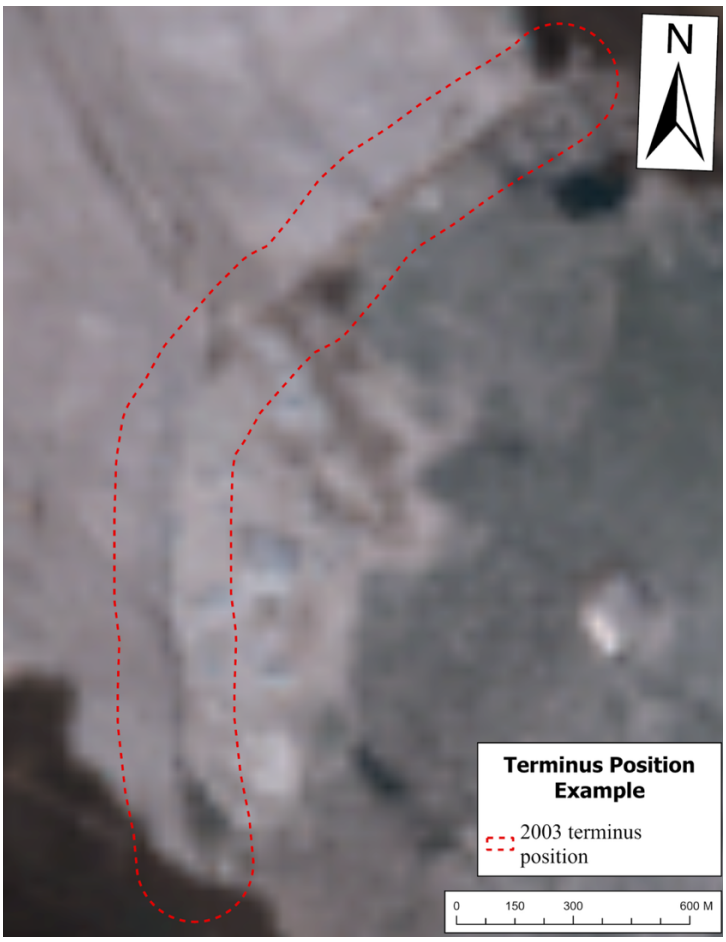


Figure 3-4: illustrates a difficult-to-delineate image. The image is a Landsat 7 capture from July 16, 2003, showing clear ocean, icebergs, and mélange along the ocean-terminus interface. Overlaid on the image is a red dashed circle showing where the terminus was delineated to provide an example of the decisions made on terminus delineations.

Figure 3-4 shows an example of a 2003 Landsat image with a clear section of the terminus (top right) and a complex section (centre). In images with a clear view of the terminus, the line was drawn on the upglacier side of the dark pixels. In Figure 3-4, sea ice is present in the image, obscuring the position of the terminus and making delineation more difficult. In instances such as this, the shape of the object, along with temporal context, was used to determine the position of the terminus. Once the terminus positions were traced, the change in distance was calculated along the terminus transect lines (Figure 3-5).

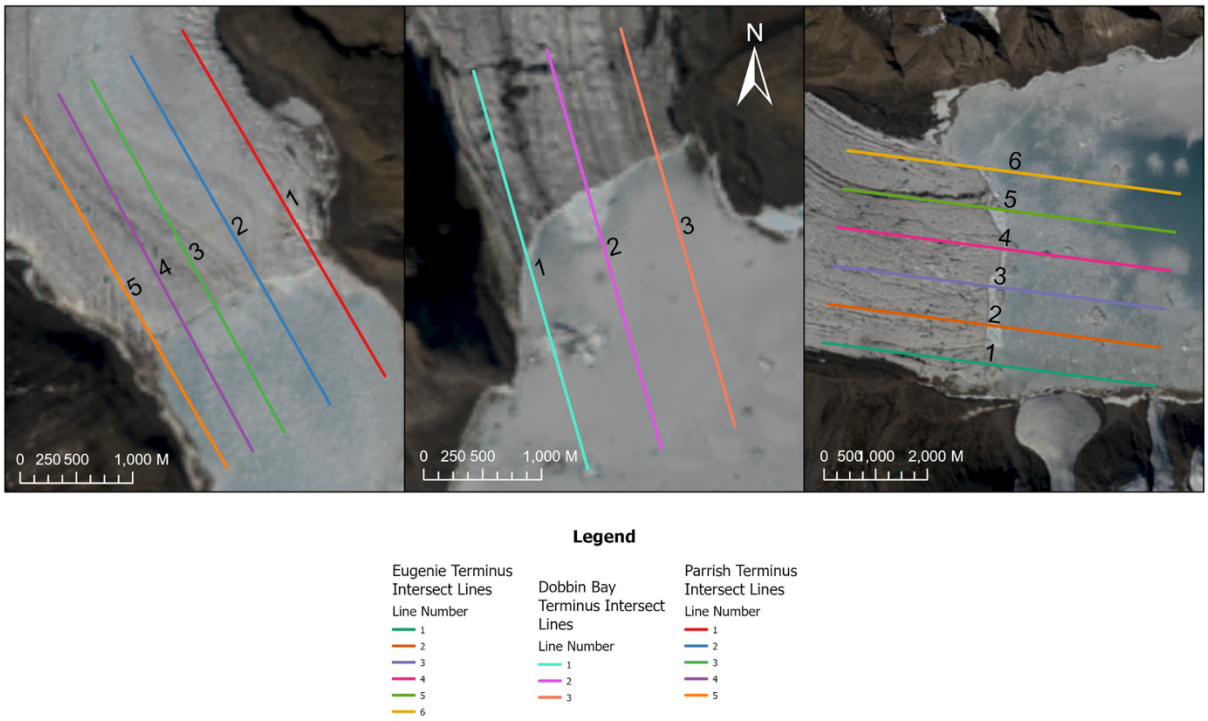


Figure 3-5: The created terminus intersect lines used to measure the change in distance between yearly terminus positions. Showing Parrish Glacier on the left, Dobbin Bay Glacier in the middle and Eugenie Glacier on the right. All overlaid on Landsat imagery, June 2, 2019

Transect lines were placed roughly parallel to the centreline flow, with additional lines being placed 1 km offset from the centre. Terminus-intersecting lines are then used to measure the distance between successive years' terminus positions. Allowing for the temporal evolution of the terminus to be quantified.

Uncertainty in terminus positions arises in two ways: first, from satellite imagery and manual tracing; second, from georeferencing. As seen in Table 3-1, there are four levels of resolution for the satellite imagery used: 60 m for Landsat 1, 2, and 3; 30 m for Landsat 7, 8, and ASTER; 20 m for SPOT; and 5 m for the air photos. Along with this, georeferencing and manual delineation lead to an uncertainty of +/- 1-3 pixels, leading to an expected uncertainty of 60-180 m for Landsat 1, 2, 3; 30 – 90 m for Landsat 7, 8, ASTER; 20 – 60 m for SPOT; and 5 – 15 m for the aerial photograph.

3.4 Basal Topography

As outlined in section 2.2, the geometry at the bed of the glacier seems to be very important for pulsing glacial dynamics. As such, characterizing the basal topography underneath glaciers is highly relevant for this investigation. Additionally, regarding pulse-type glacier literature, it was previously theorized that pulse-type activity was bound to regions where the bed was below sea level (Van Wychen, 2016).

Bed elevation data was collected by NASA using the Centre for Remote Sensing of Ice Sheets (CReSIS) Multichannel Coherent Data Depth Sounder (MCoRDS) during the 2014 Greenland Mission Operation IceBridge data collections (CReSIS, 2024). The MCoRDS system was fitted on the P-3 Orion and flown along the centerlines of Dobbin Bay Glacier, Eugenie Glacier, and Parrish Glacier on April 1st, 2014. MCoRDS is an ice penetrating radar system that operates at a frequency range of 180-210 MHz as a depth sounder by emitting a pulse of energy and measuring the time it takes for the pulse to return to the receiver (CReSIS, 2014). The data collected from the mission was then organized into three data groups: L1b, which is the echograms; L2, which is the ice thickness, ice surface and ice bottom elevations; and L3, which is the gridded ice thickness, ice surface and ice bottom elevations (CReSIS, 2014). For this thesis, the L3 product was used. While the data was collected along the centerline, the L3 product was created by merging multiple datasets, including radar depth sounder data over multiple seasons, airborne LIDAR data for the ice surface, optical data for ice boundaries, and various DEM products. (CReSIS, 2014), This creates a 3D rasterized visualization of the bed topography at a resolution of 25 m^2.

Gridded bed topography data sets were created from the 2014 MCoRDS data for the Canadian Arctic region, and these data sets were downloaded from the CReSIS data portal. Basal topography maps were created by subtracting nadir ice thickness data from a surface

DEM. Previous studies have suggested that the uncertainty of the MCoRDS system is within 10-20 m (Wu et al., 2011; Jezek et al., 2013; Dalton et al., 2022). The gridded bed topography raster provides an estimate of bed position outside the MCoRDS flightline. Changes in the slope and elevation of the subglacial topography provide further context for the geometric factors affecting pulse-type systems. Subglacial topography also allows stronger relationships to be drawn between elevation change and velocity variability. If irregular dynamic and geometric activity is found in locations of the glacier with specific subglacial topographic conditions (i.e., areas below sea level), further inferences can be drawn about the impact that subglacial topography may have on pulse-type systems.

3.5 Deflection Angle

Collecting deflection angles at significant turns in the valley flow is used to better understand local ice dynamics within systems. While the deflection angle of a glacier's valley has not been directly linked to irregular dynamics within the CAA, changes in flow direction are understood as an effect of dendritic glaciers, which have been found to affect surge dynamics. Specifically, at junction locations where flows connect, the downglacier region is impacted, including changes in flow direction, increased ice flux, enhanced basal erosion, and horizontal and vertical strain (Jiskoot et al., 2017). Therefore, in key areas of the study glaciers, the deflection angle of the valley was collected. Deflection angles are more commonly used in river studies to understand erosion processes on river walls (Li et al., 2018). Since the change in flow direction is conceptually the same, a similar azimuth-based approach is used here.

The deflection angle of the valley was derived by taking the azimuth of centre lines along the relevant glaciers. Using Landsat imagery, lines were digitized before and after the turn in the valley along the valley's centreline. To ensure comparable azimuth readings, each line was digitized from upglacier to downglacier. The azimuths of the lines were then calculated using the Calculate Geometry tool in ArcGIS Pro. The deflection angle of the valley

turn was calculated using the difference in azimuth between the upglacier and downglacier centre lines (Li et al., 2018).

3.6 Method Summary

The methodologies outlined in this chapter allow for a record of mass build-up, ice velocity, and terminus position evolution to be created for the selected study glaciers. As shown in Table 3-2, data from various sources have been processed, providing a comprehensive understanding of the dynamic and geometry evolution of Dobbin Bay Glacier, Parrish Glacier, and Eugenie Glacier from 1959 to 2024 and enabling the identification of pulse-type activity. While the methodologies have variable temporal coverages, sufficient overlap exists to provide an understanding of the activity experienced across the selected sites.

Table 3-2: Summary of remote sensing products used along with associated methodology and temporal coverage of the dataset.

Methodology	Dataset & Source	Temporal Coverage
Surface Elevation Change	ArcticDEM – University of Minnesota	2010 - 2024
Velocity Variability	ITS_LIVE - NASA	1999 - 2022
Terminus Position	Historic Air photo – (Cook et al., 2019)	1959
Terminus Position	Spot – CNES	1980 - 1996
Terminus Position	Aster – NASA JPL	2004 - 2011
Terminus Position	Landsat 1, 2, 3, 7, 8, 9 - NASA	1970 - 2024
Bedrock Topography	Multichannel Coherent Data Depth Sounder (MCoRDS) – Center for Remote Sensing of Ice Sheets (CReSIS)	2014
Deflection Angle	Landsat 9 – Nasa	2019
Glacier Outlines	Randoph Glacier Inventory (RGI) – NSDIC Pfeffer, 2014	2000

Chapter 4 - Results

This chapter presents the major results of the thesis, organized by glacier: Dobbin Bay Glacier first, followed by Parrish Glacier, and finally Eugenie Glacier. Elevation change will be reported first, then velocity variability, terminus position and finally bed tomography.

4.1 Dobbin Bay Glacier

For the purposes of reporting results, Dobbin Bay Glacier is divided into three sections: the terminus region, the lower trunk and the upper glacier (Figure 4-1). The ‘terminus region’ of Dobbin Bay Glacier extends from the glacier terminus to 2.5 km upglacier. The ‘lower trunk’ extends from 2.5 km from the terminus to 12.5 km from the terminus. Finally, beyond 12.5 km from the terminus is considered the ‘upper glacier’.

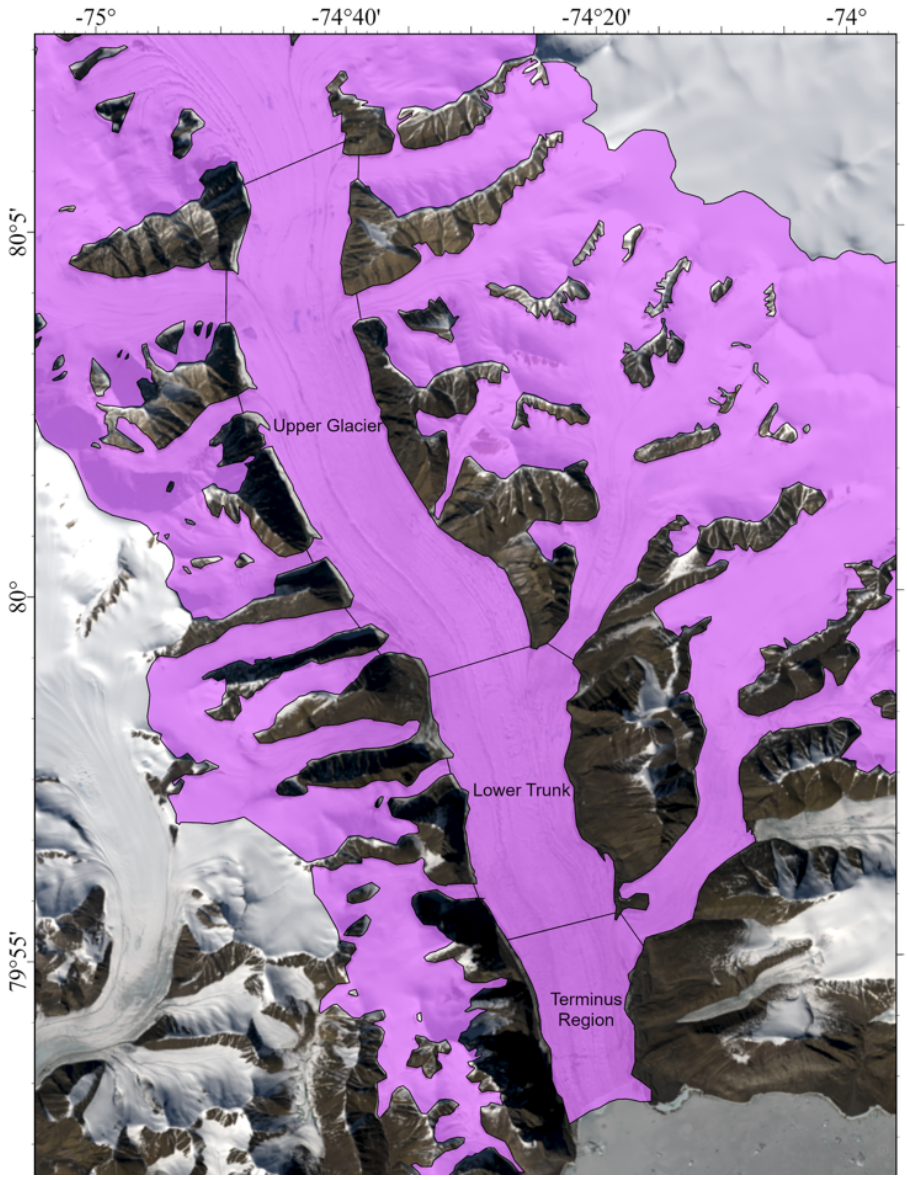


Figure 4-1: The primary trunk of Dobbin Bay Glacier, divided into three sections. Overlayed on Landsat Imagery (collected June 2, 2019)

4.1.1 Dobbin Bay Glacier Geometry Change

Between 2012 and 2022, there was a notable pattern of surface elevation change, with high elevation loss in the terminus region, elevation gain through the lower trunk (Figure 4-2), and slight elevation loss across the upper glacier (not shown in Figure 4-2). As seen in Figure 4-2, pronounced loss occurs close to the terminus at a rate of -2.5 m a^{-1}, but steadily decreases to -1 m a^{-1} by the upglacier portions of the terminus region. Between the terminus region and the lower trunk is a transition zone, where trends of elevation loss switch to elevation gain. The majority of the lower trunk region experiences an elevation gain of around 1 m a^{-1}. But rather

than steadily increasing, the rate of elevation gain varies across the region in patches. These five patches experience high rates of elevation gain, up to 4 m a^{-1} in places. Three of these patches are found along the centreline flow of Dobbin Bay Glacier, while the two remaining patches are found on the west and east sides of the lower trunk. Within the upper glacier region, areas of elevation loss and gain are variable, with most of the surface area showing no change in elevation.

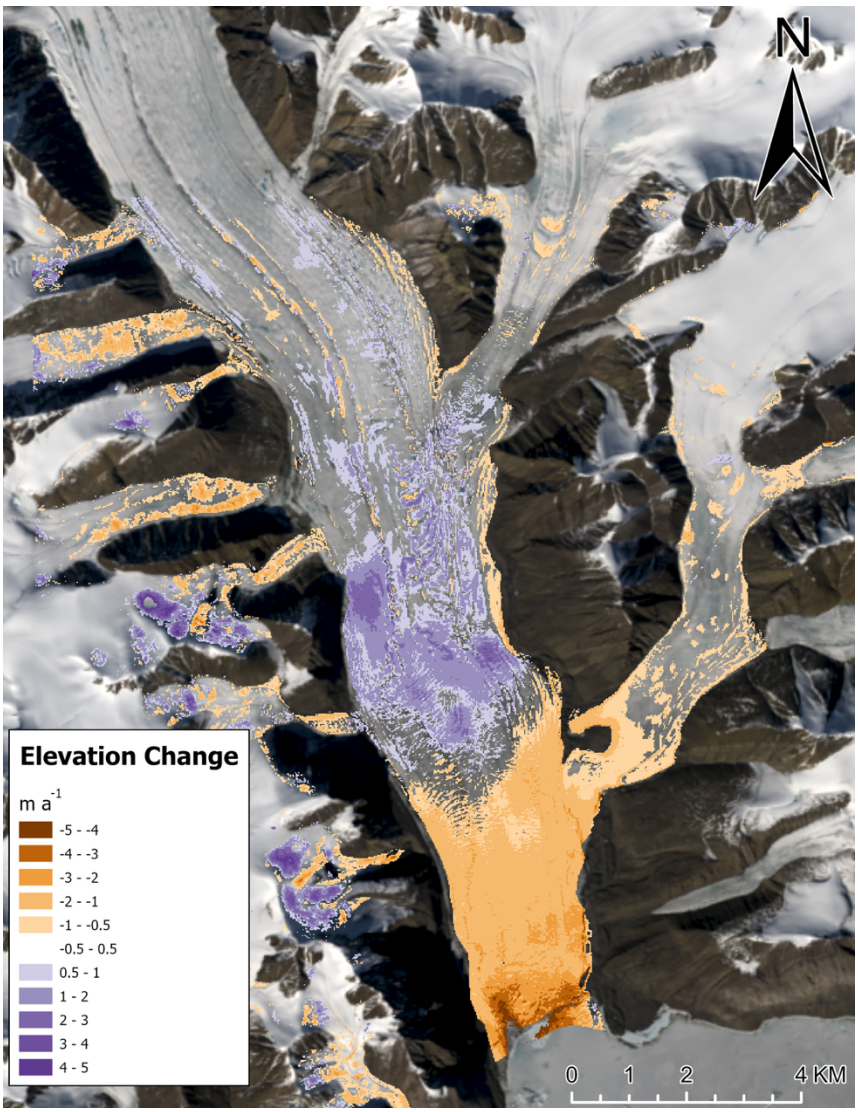


Figure 4-2: Surface elevation change from 2012 to 2022 over Dobbin Bay Glacier, derived from ArcticDEM StripMap using xDEM. Overlaid on Landsat 8 imagery (July 2, 2019).

In examining the annual elevation differencing products in Figure 4-3, similar trends to those in the decadal differencing (Figure 4-2) emerge. With the terminus region and upper glacier remaining regions of elevation loss. While the lower trunk mostly experiences elevation gain throughout the annual difference products, there are years when the region experiences no elevation change or a slight loss. While 2014-2015, 2016-2017, 2019-2020, and 2021 – 2022 experience elevation change rates of -1 – 0 m a^{-1}, most annual differences experience elevation gains of 1-3 m a^{-1}.

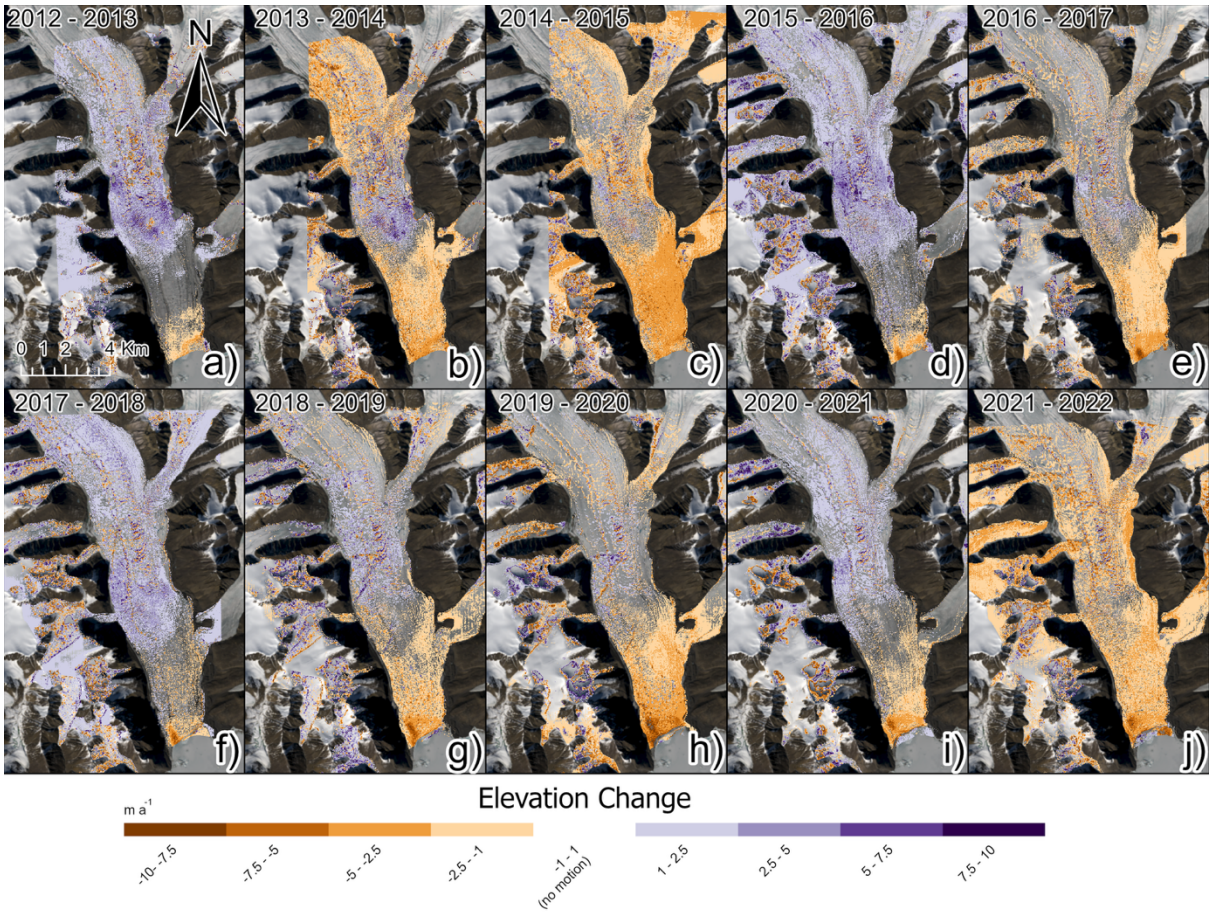


Figure 4-3: Annual surface elevation change composite of Dobbin Bay Glacier, derived from xDEM. Overlaid on a Landsat 8 true colour composite imagery acquired on June 2, 2019.

4.1.2 Dobbin Bay Glacier Ice Velocity

Within the upper glacier, the flow speeds do not change over the study period, with velocities remaining at ~75 m a^{-1} between 12.5 km and 22.5 km and slowing further beyond

this point. Within the lower trunk, velocities varied from a minimum of ~25 m a^{-1} to a maximum of up to ~1100 m a^{-1} during the study period (Figure 4-3).

In 2000 and 2001, the velocities of Dobbin Bay Glacier remained consistent throughout the valley, with ice motion between 50 m a^{-1} and 75 m a^{-1} measured in these years (Figure 4-4). In 2002, the near-terminus region experienced higher velocities, approaching ~150 m a^{-1}. These high terminus velocities then began to spread up the glacier in 2003, with velocities rising to 200 m a^{-1} up to 5 km of the terminus (Figure 4-4). From 2004 to 2007, velocities increased and spread up the glacier, with the terminus region in 2004 reaching velocities of ~500 m a^{-1} (Figure 4-4). 2005 is when the highest velocities are recorded across the glacier. In the near terminus region, velocities rose to ~1100 m a^{-1} and gradually decreased to ~100 m a^{-1} by the 12.5 km marker (Figure 4-4). While peak velocities decreased from 2006 to 2007, the extent of faster ice flow extends further up the glacier, with velocities of 150 m a^{-1} extending to 20 km from the terminus (Figure 4-4). The trend of higher velocities in the lower sections of Dobbin Bay, observed from 2003 to 2007, reverses in 2008 with the slowest section of the glacier recorded between the terminus and 5 km from it (Figure 4-4). In this region, velocities only reach ~100 m a^{-1}, while the glacier velocities beyond 5 km from the terminus to 12.5 km from the terminus remain at ~150 m a^{-1}. This trend remains in 2009 and strengthens in 2010, with the section of the glacier between the terminus and 7.5 km from the terminus decreasing to velocities less than 50 m a^{-1}. The flow structure then remains relatively constant for the remaining 12 years of recorded data. In the remaining time, velocities between the terminus and 7.5 km from the terminus remain near ~25 m a^{-1}, with velocities gradually increasing up to 50 m a^{-1} once reaching 15 km from the terminus (Figure 4-4).

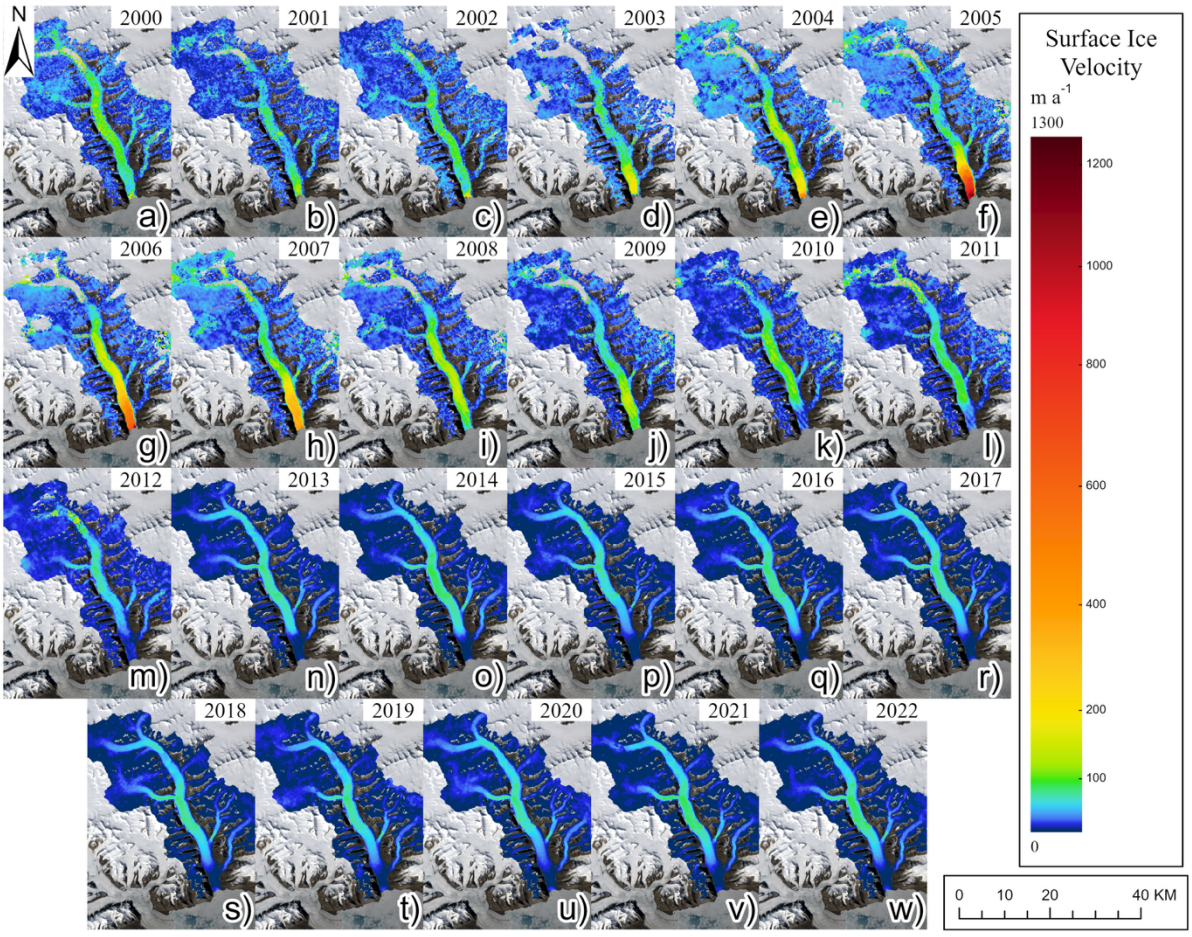


Figure 4-4: ITS_LIVE composite velocity products by NASA JET Propulsion Laboratory, covering Dobbin Bay Glacier from 2000 to 2022, derived from optical imagery. Each image is the average surface ice velocity collected over the year.

4.1.3 Dobbin Bay Terminus Positions Change

Dobbin Bay Glacier exhibits three periods of terminus position evolution: receding from 1959 to 2003, advancing from 2004 to 2007, and finally retreating again from 2008 to 2024 (Figure 4-5). This pattern persists across the entire length of the terminus, with the terminus along the centre and western transects evolving more similarly than the terminus along the eastern transect. The 1959 terminus position, which is the maximum recorded extent, lies beyond the surrounding bedrock topography of the valley, extending into Dobbin Bay (Figure 4-5). Over the next 4 decades, the glacier receded gradually, reaching its minimum extent in 1999 and remaining at that position for 3 years until 2002 (Figure 4-5). From the earliest observation to 2002, the terminus along the western and centre transects both retreated 2 km, while the terminus along the eastern transect only retreated 1.3 km (Figure 4-5d).

Beginning in 2003, the terminus advanced rapidly, with the glacier along the western transect advancing nearly 2 km within 4 years, almost reaching its 1959 position (Figure 4-5b). The terminus along the centre transect also advances rapidly, advancing 1.7 km, while the eastern section of the terminus advances 800 m (Figure 4-5b). Following 2008, the glacier began to retreat again (Figure 4-5c), but at a faster rate than previously experienced. Within 15 years, the western terminus retreats by 1.5 km while the centre retreats 1 km (Figure 4-4c). The eastern portion of the terminus also experiences rapid retreat, but only retreats by 700 m. While uncertainty is present within the terminus position delineations, the magnitude of motion experienced by Dobbin Bay's terminus is greater than the uncertainty expected and described in the methodology chapter.

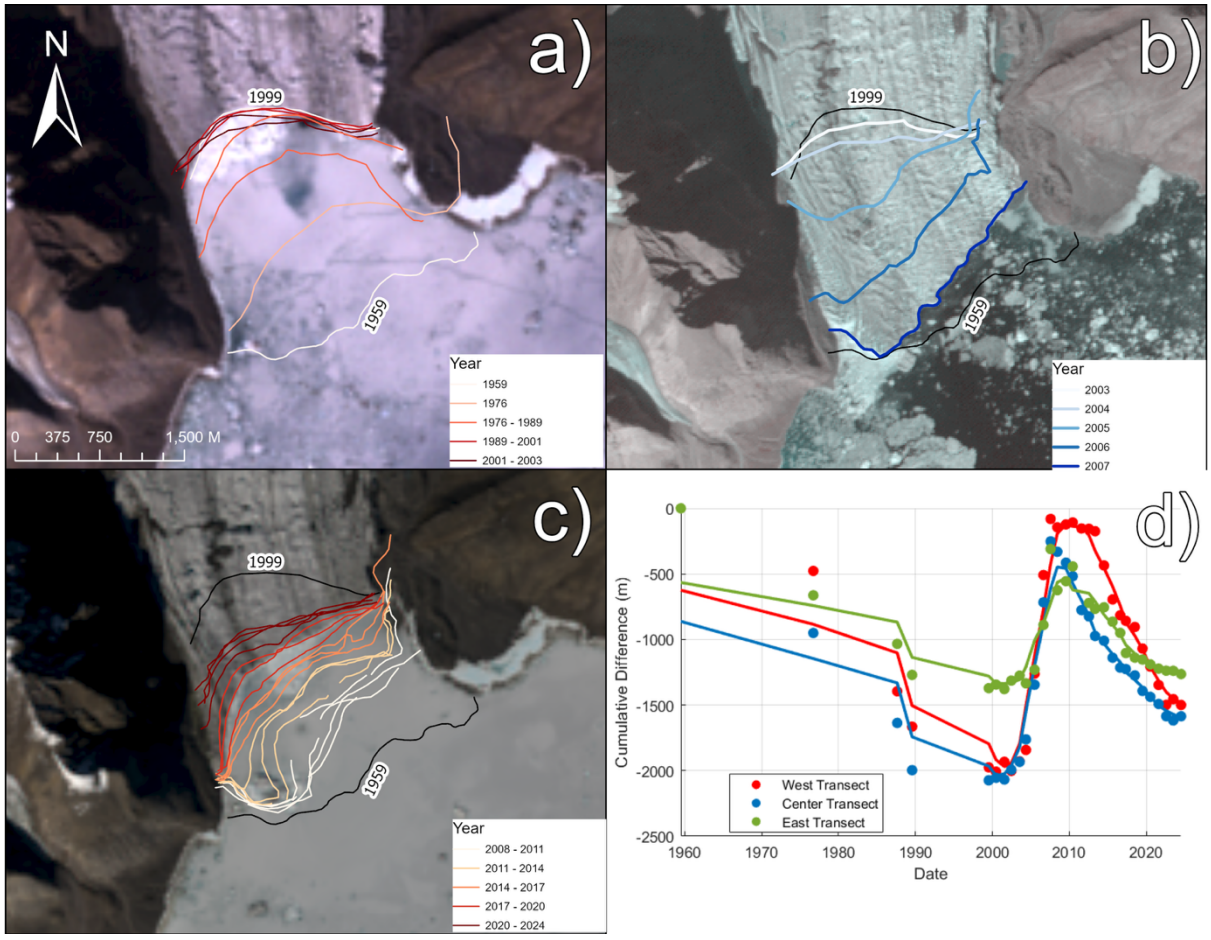


Figure 4-5: Evolution of annual terminus position of Dobbin Bay Glacier from 1959 to 2024. Terminus positions are grouped based on the trend of motion presented in graph D. A) spans from 1959 to 2003, B) spans from 2003 to 2007, and C) spans from 2008 to 2024. Terminus positions are overlaid on relevant satellite captures: A) Landsat 7 satellite image, July 9, 1999;

B) ASTER satellite image captured, July 22, 2007; C) Landsat 8, July 2, 2019. D) provides the terminus position along transects through the glacier and compares the position relative to the 1959 terminus position.

4.1.4 Dobbin Bay Glacier Bed

Figure 4-6 provides the bedrock topography underneath Dobbin Bay Glacier clipped to the extent of the 2013 terminus position. The deepest region of the bed is present slightly upglacier of the terminus, with a channel in the bed which runs for 2 km at a depth of -175 m a.s.l. At 6 km from the terminus, a subglacial bump, which rises to ~30 m a.s.l., is present and following this, bed elevations then rise above 0 m roughly 17 km from the terminus.

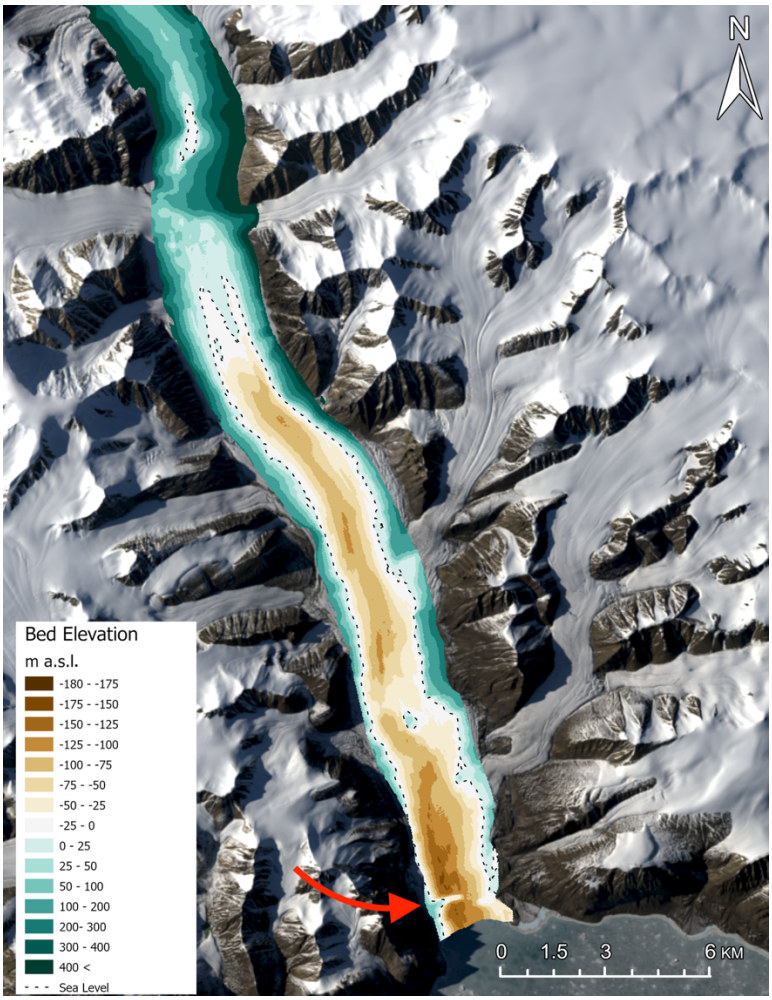


Figure 4-6: Subglacial topography of Dobbin Bay Glacier, obtained from the CReSIS MCoRDS sensor, acquired in 2014. Regions of potential error are denoted by a red arrow. Sea level is denoted by a dotted line. Overlayed on Landsat true-colour composite imagery (June 2, 2019).

Within the MCoRDS dataset, there is a region of spurious data which suggests a potential region of processing error (denoted with a red arrow in Figure 4-6). In this area, the

bed rises above sea level to 50 m a.s.l., which seems unlikely given that this area lies within 200 m and directly interrupts the deepest channel along the bed.

4.2 Parrish Glacier

For the purposes of reporting results, Parrish Glacier is divided into four sections: the ‘terminus region’, the ‘lower trunk’, the ‘middle trunk’ and the ‘upper glacier’ (Figure 4-7). The ‘terminus region’ of Parrish Glacier extends from the terminus to 1 km upglacier from it. The ‘lower trunk’ extends from 1 km from the terminus to 7 km. Then the ‘middle trunk’ is present from 7 km from the terminus to 17.5 km from the terminus. Finally, the ‘upper glacier’ area, which exists from 17.5 km upglacier from the terminus and extends upglacier into the main body of Parrish Glacier.

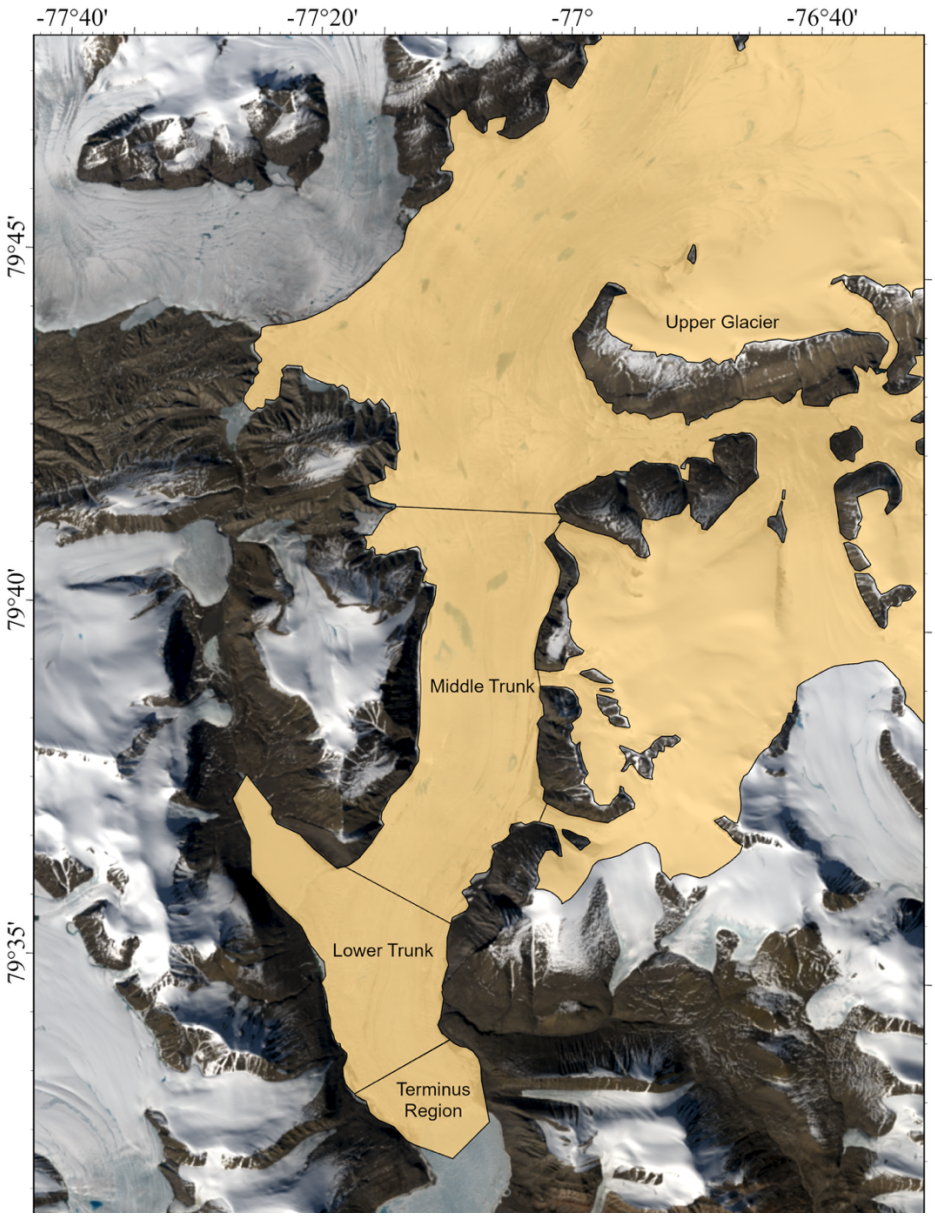


Figure 4-7: The main trunk of Parrish Glacier, divided into four regions. Overlayed on Landsat Imagery (June 2, 2019)

4.2.1 Parrish Glacier Geometry

In the decadal elevation change on Parrish Glacier, three major regions of activity are evident: elevation loss at the terminus, elevation gain in the lower and middle trunks, and elevation loss in the upper glacier (Figure 4-8). Within the terminus region, elevation loss is greatest at the terminus at -1.8 m a^{-1} and slightly decreases to the end of the region to a rate of -0.5 m a^{-1} (Figure 4-8). A small region of no change exists along the transition between the terminus region and the lower trunk, with elevation steadily increasing to 2 m a^{-1} throughout the lower trunk (Figure 4-8). Elevation gain is largest upglacier of the transition between the

lower and middle trunk, where the glacier experiences elevation gains of 3 m a^{-1} to 3.5 m a^{-1} (Figure 4-8). Beyond 10.5 km from the terminus, elevation steadily decreases to 1 m a^{-1} by the end of the middle trunk (Figure 4-8). The upper glacier experiences a loss rate of -1 m a^{-1} in the lowest regions, then steadily decreases throughout the rest of the region.

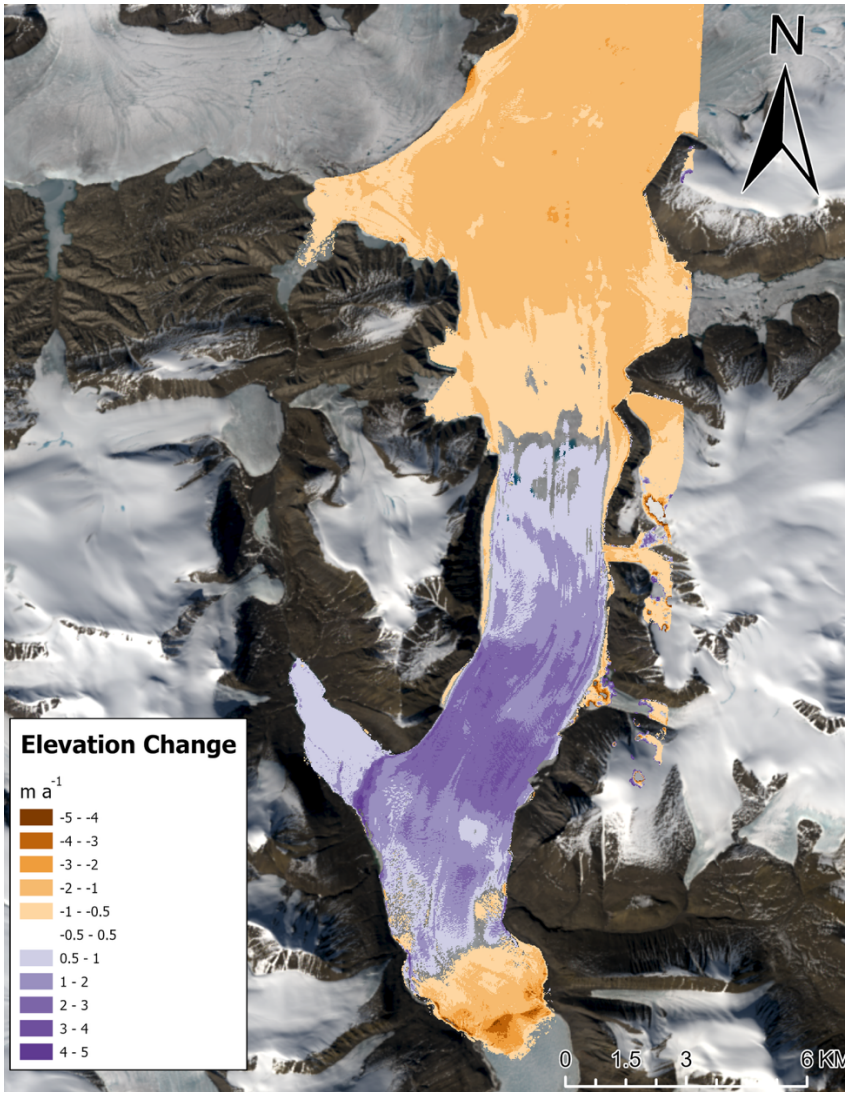


Figure 4-8: Surface elevation change of Parrish Glacier from 2011 – 2023, derived from ArcticDEM StripMap using xDEM. Overlaid on Landsat 8 imagery collected July 2, 2019.

Interannual comparisons of elevation over Parrish Glacier show that elevation gain primarily occurs in the middle trunk from 7 km to 10 km from the terminus (Figure 4-9). In all interannual difference maps, this region consistently has the highest rates of elevation gain. The lower trunk experiences years with no elevation change or loss, namely in 2012 - 2013 and 2019 – 2020 (Figure 4-9). The upper glacier region also primarily experiences elevation loss,

with 2016 – 2017 and 2020 – 2021 being years with the most extensive coverage of no change to slight gain (Figure 4-9).

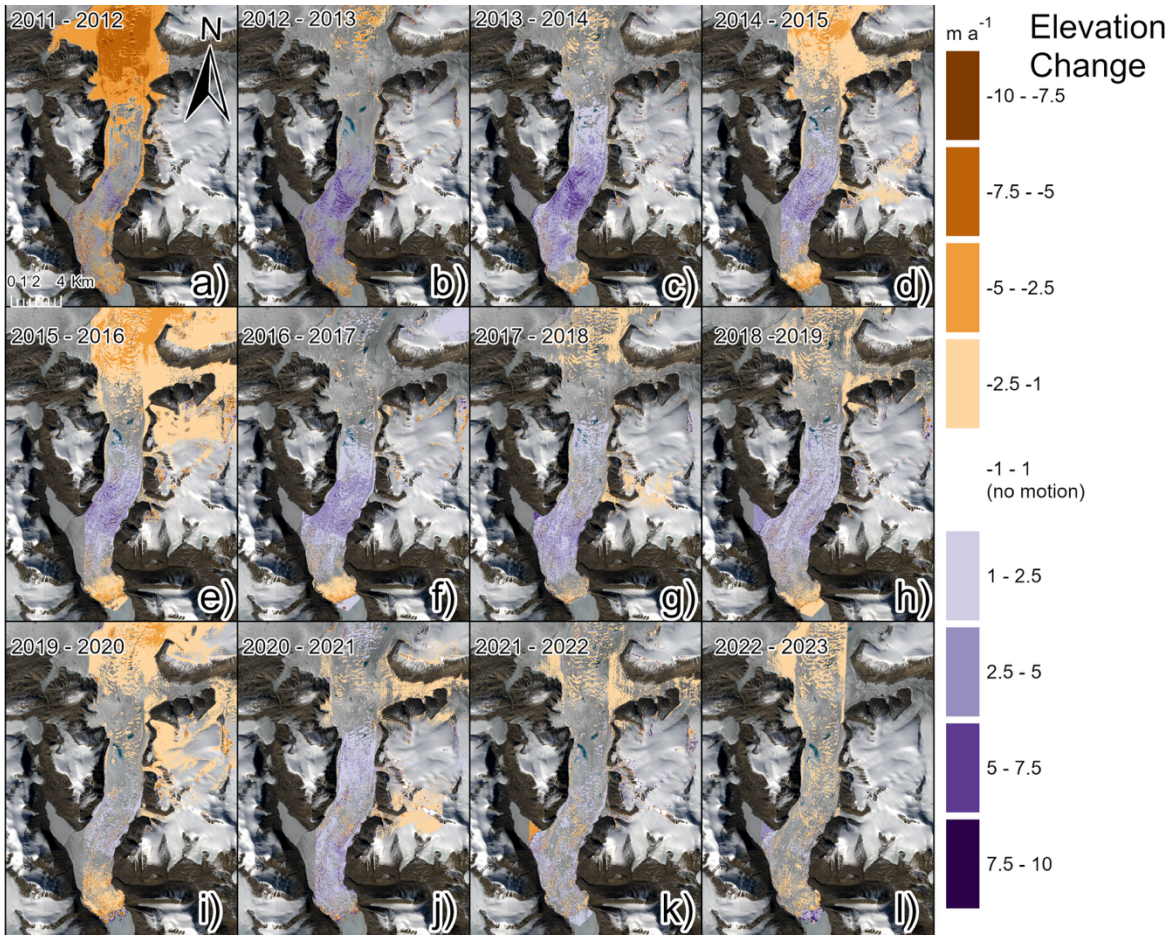


Figure 4-9: Surface elevation change composite of Parrish Glacier, derived from xDEM. Overlaid on a Landsat 8 imagery acquired on June 2, 2019.

4.2.2 Parrish Glacier Velocity

From 2000 to 2004, the velocity record of Parrish Glacier is of relatively low quality, but the results show that the glacier likely maintained a consistent velocity of ~100 m a^{-1} over this period (Figure 4-10). In 2005, velocities in the lowermost region began to increase, with velocities in this area ranging from 300 – 600 m a^{-1}. In 2006 and 2007, velocities peak at ~1200 m a^{-1} throughout the terminus and lower trunk regions of the glacier, which represent the maximum flow speeds observed for the glacier over the entire observation period. In 2008, glacier speeds generally slowed throughout the lower and middle trunk to speeds around 600 m a^{-1} (Figure 4-10). By 2009, velocities slowed further, with the lower trunk and the terminus

region reaching maximum velocities of 200 m a^{-1}, while the middle trunk maintained velocities of 600 m a^{-1}. From 2011 to 2022, the velocity structure of Parrish Glacier remains largely consistent, with relatively slow velocities that are near stagnation measured in the lower terminus region, and higher velocities of ~100 m a^{-1}, measured along the middle portion of the main trunk of the glacier.

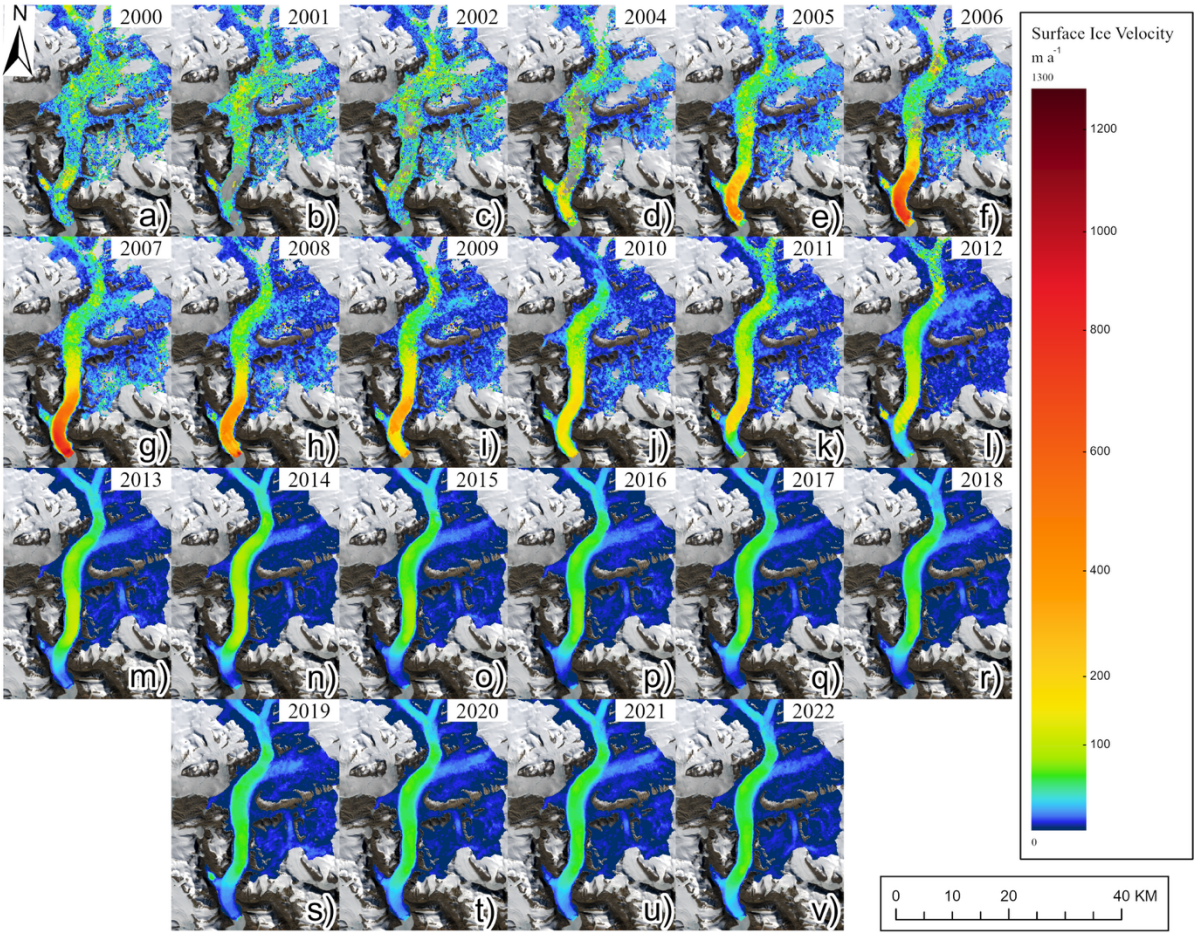


Figure 4-10: ITS_LIVE composite velocity products by NASA JET Propulsion Laboratory, covering Parrish Glacier from 2000 to 2022 and derived from optical imagery. 2003 was not included due to the high presence of error. Each image shows the average velocities collected over the year. Overlaid on Landsat 8 imagery collected June 2, 2019.

4.2.3 Parrish Terminus Positions

Parrish Glacier's terminus position evolution is grouped into three periods: recession from 1959 to 2003, advance from 2004 to 2012, and recession from 2012 to 2024 (Figure 4-11). Different portions of the terminus experience differing rates of retreat or advance, but all largely follow the same trend. The position of the terminus in 1959 is one of the most advanced

positions delineated over the entire observation period and at this time it had a concave profile along the glacier front, suggesting the glacier was in a retreating phase prior to this time (Figure 4-11a). Over the next four decades, from 1959 to 2003, the terminus retreated more pronouncedly along the northeastern side of the glacier (Figure 4-11a). A relatively large retreat occurred between 1975 and 1982, when the glacier retreated nearly 2 km on its northeastern side. During the same period, the terminus along the southwestern transect only retreated 250 m. After 1982, retreat occurs more gradually, with the northeastern portions retreating by about 500 m and the southwestern portions by about 1 km. Retreat continued until 2003, when the minimum extent was recorded. In total, from 1959 to 2003, the terminus retreated a total of ~2 km along the southwestern side and ~2.6 km along the northeastern side.

In 2004, Parrish Glacier experienced a period of terminus advance that ended in 2012, when the maximum terminus extent was recorded (Figure 4-11b). During this 8-year period, most of the advancement occurred from 2005 to 2008 (Figure 4-11b), where the glacier advanced ~1 km along the southwestern and central portions, and 1.5 km along the northeastern side. By 2012, Parrish Glacier's terminus had advanced past the 1959 position along the centre of the terminus. As the terminus advanced over the latter portion of the 2004-2012 period, the profile of the glacier also changed from convex to concave and it is notable that over this 8-9 year period, nearly all of the glacier retreat that had been observed between 1959 and 2003 had been regained.

From 2012 to 2013 the glacier transitions back into a period of retreat, with the terminus beginning to recede and the middle portion of the terminus retreating 500 m. Following a period of rapid retreat from 2013 to 2017, the terminus position then stabilizes. The position of the terminus remained relatively consistent over the next 7 years until the end of the observation period. With the terminus retreating 1 km through the centre and 750 m along the valley walls from 2017 to 2024.

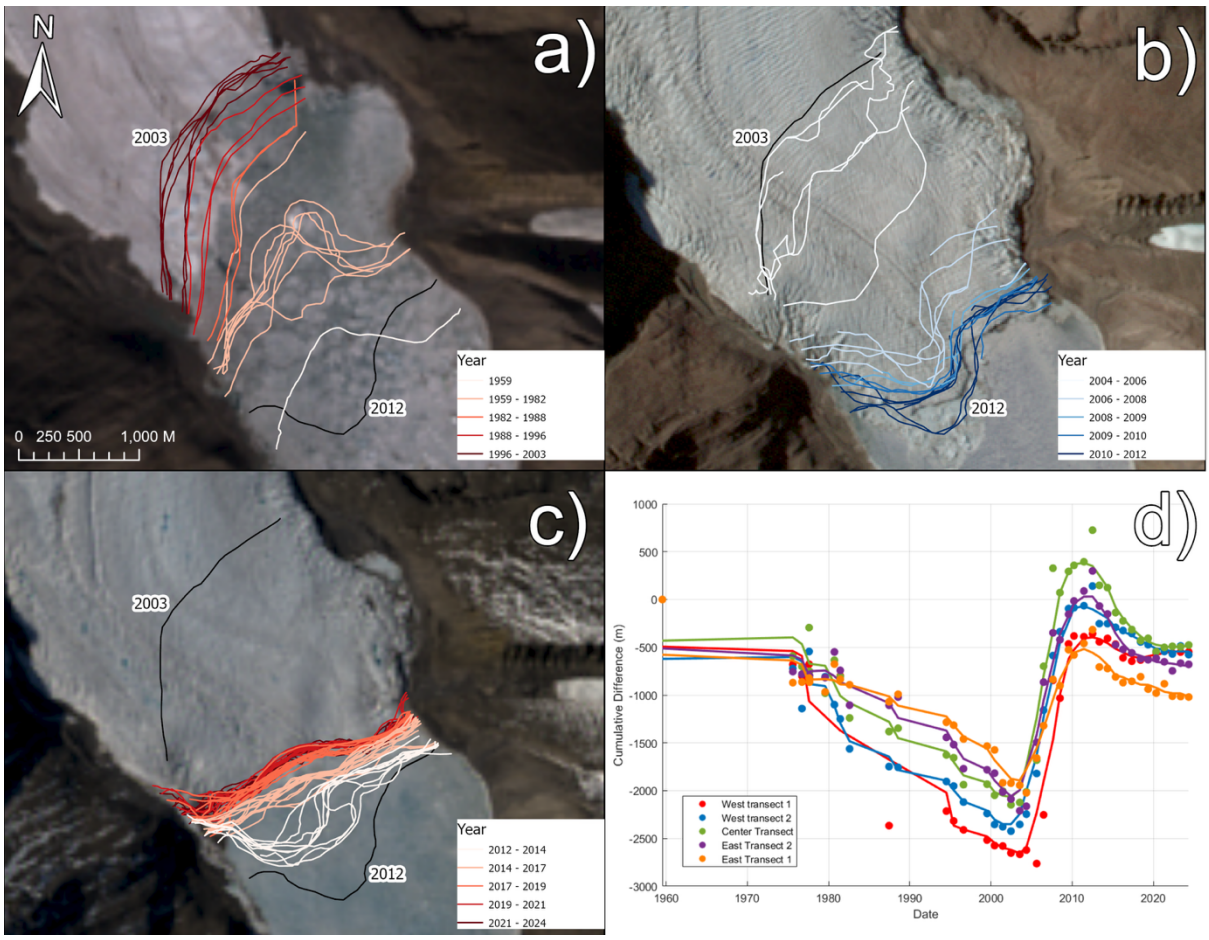


Figure 4-11: Evolution of annual terminus positions of Parrish Glacier from 1959 to 2024. Terminus Positions are grouped based on the trend of motion presented in graph D. A) spans from 1959 to 2003, B) spans from 2003 to 2012, and C) spans from 2012 to 2024. Terminus positions are overlaid on correlating satellite imagery: A) Landsat 7, July 16, 2003; B) Aster, July 5, 2011; C Landsat 8, July 1, 2023. Graph D provides the terminus position along transects through the glacier and compares the position to the 1959 terminus position.

4.2.4 Parrish Bed Topography

Figure 4-12 provides the bed topography of Parrish Glacier. The bed is the deepest throughout the lower trunk to the terminus, with the deepest depth being -150 m a.s.l at 3 km from the terminus. At 10 km from the terminus there is a subglacial ridge, with elevations rising to -50 m a.s.l and dipping to -100 m a.s.l on the lee and stoss sides of the ridge. Bed elevations rise above 0 m a.s.l at 17.5 km upglacier from the terminus.

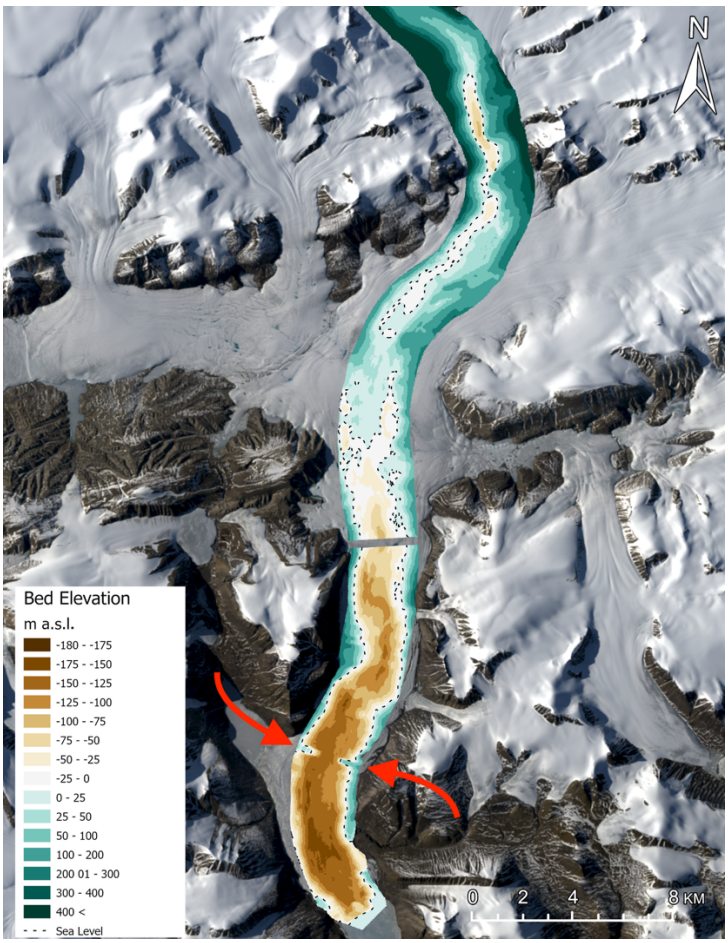


Figure 4-12: Subglacial topography of Parrish Glacier, from the CReSIS MCoRDS sensor, acquired in 2014. Regions of potential error are denoted by a red arrow. Sea level is denoted by a dotted line. Overlayed on Landsat Imagery (June 2, 2019)

At ~7 km from the terminus, two areas of seeming error are present on both sides of the glacier's valley (identified with red arrows in Figure 4-12). The error suggests that there are two features at an elevation of 100 m a.s.l. that protrude ~1 km from the valley walls. Due to the location and steepness of the features, these objects are most likely processing errors within the data.

4.3 Eugenie Glacier

Eugenie Glacier is divided into 4 sections: the terminus region, the lower trunk, the transverse trunk and the upper trunk. As seen in Figure 4-13, the terminus region on Eugenie Glacier extends from the terminus to 7.5 km upglacier. Following this is the lower trunk, that runs from 7.5 km to 12.5 km from the terminus. Next is the transverse trunk, which is present

from 12.5 km from the terminus to 17.5 km from the terminus. Finally, there is the upper trunk, which is present from 17.5 km from the terminus to the main body of Eugenie Glacier.

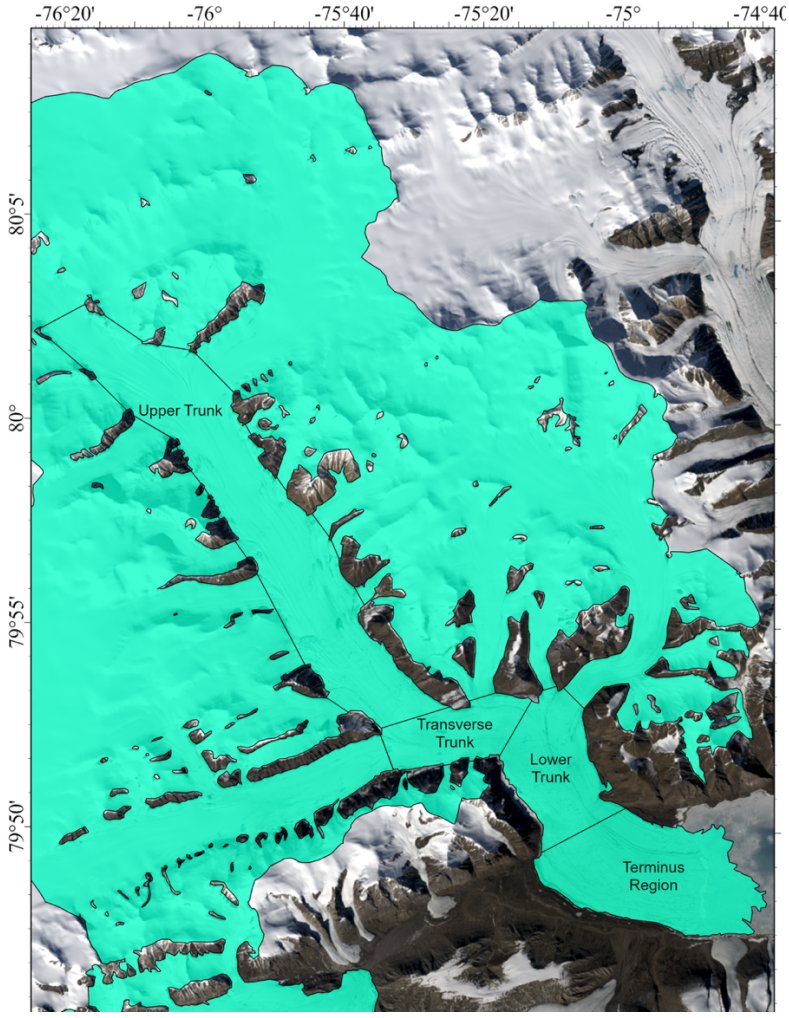


Figure 4-13: The main trunk of Eugenie Glacier, divided into four regions. Overlaid on Landsat Imagery (June 2, 2019)

4.3.1 Eugenie Glacier Geometry Change

In the decadal difference of elevation change on Eugenie Glacier, two regions of elevation loss and gain are present across the glacier. In the terminus region, there is a consistent loss of ~-2 m a^{-1}, with the rate of elevation loss decreasing closer to the lower trunk area (Figure 4-14). The lower trunk experiences two areas of elevation gain: the lower half gains slightly at 1 m $a^{-1,}$ while the upper portions gain 3 m a^{-1} (Figure 4-14). Throughout the transverse trunk, elevation change rates stay at ~2 m a^{-1} until the upper trunk. Elevation gain

occurs in the lower section of the upper trunk up to 25 km from the terminus, then slowly decreases further upglacier to the main body (Figure 4-14).

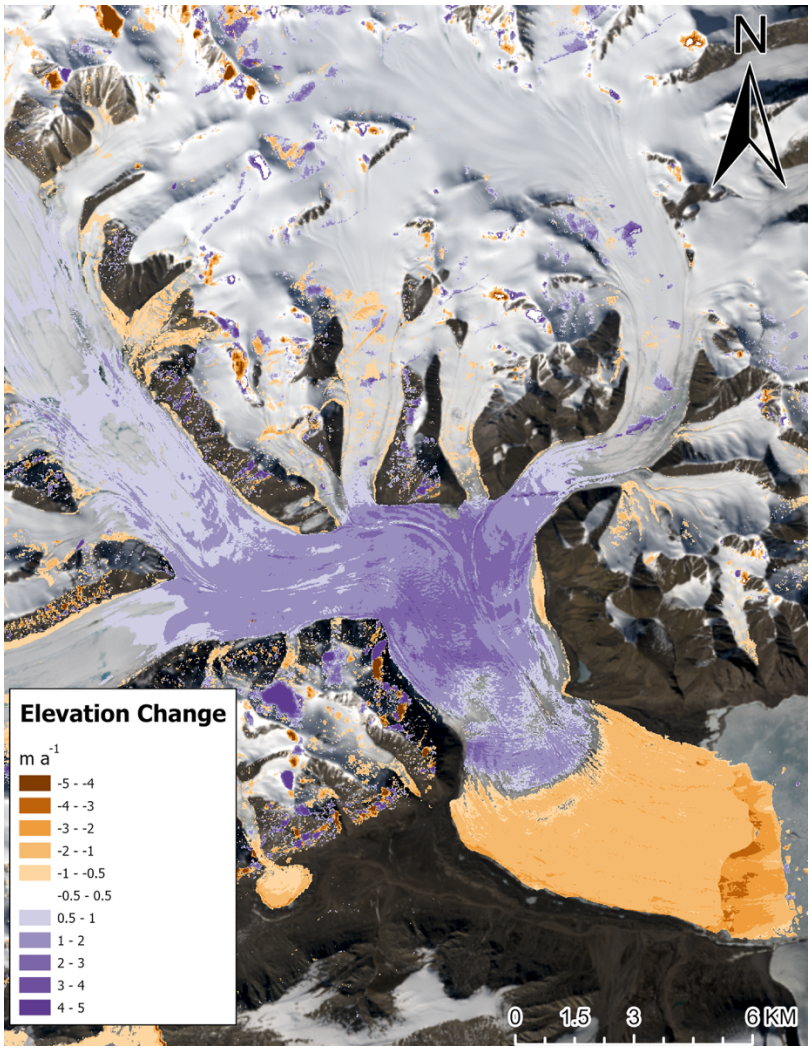


Figure 4-14: Surface elevation change of Eugenie Glacier from 2012 – 2021, derived from ArcticDEM StripMaps using xDEM. Overlaid on Landsat 8 imagery (July 2, 2019).

The trends observed in the decadal difference largely persist in interannual comparisons on Eugenie Glacier as well, with exceptions in specific years (Figure 4-15). Across all years, the terminus region experiences no change or loss, with 2020 – 2021 being the only year in which no change was observed across the entire terminus region (Figure 4-15). Elevation gain also typically begins to occur at the border between the terminus region and the lower trunk, except for 2013–2015 and 2015–2016. In recent years, elevation gain has only begun occurring

farther up the glacier, at ~8 km from the terminus. Beyond 8 km from the terminus, elevation gain is consistently experienced throughout the lower and transverse trunk.

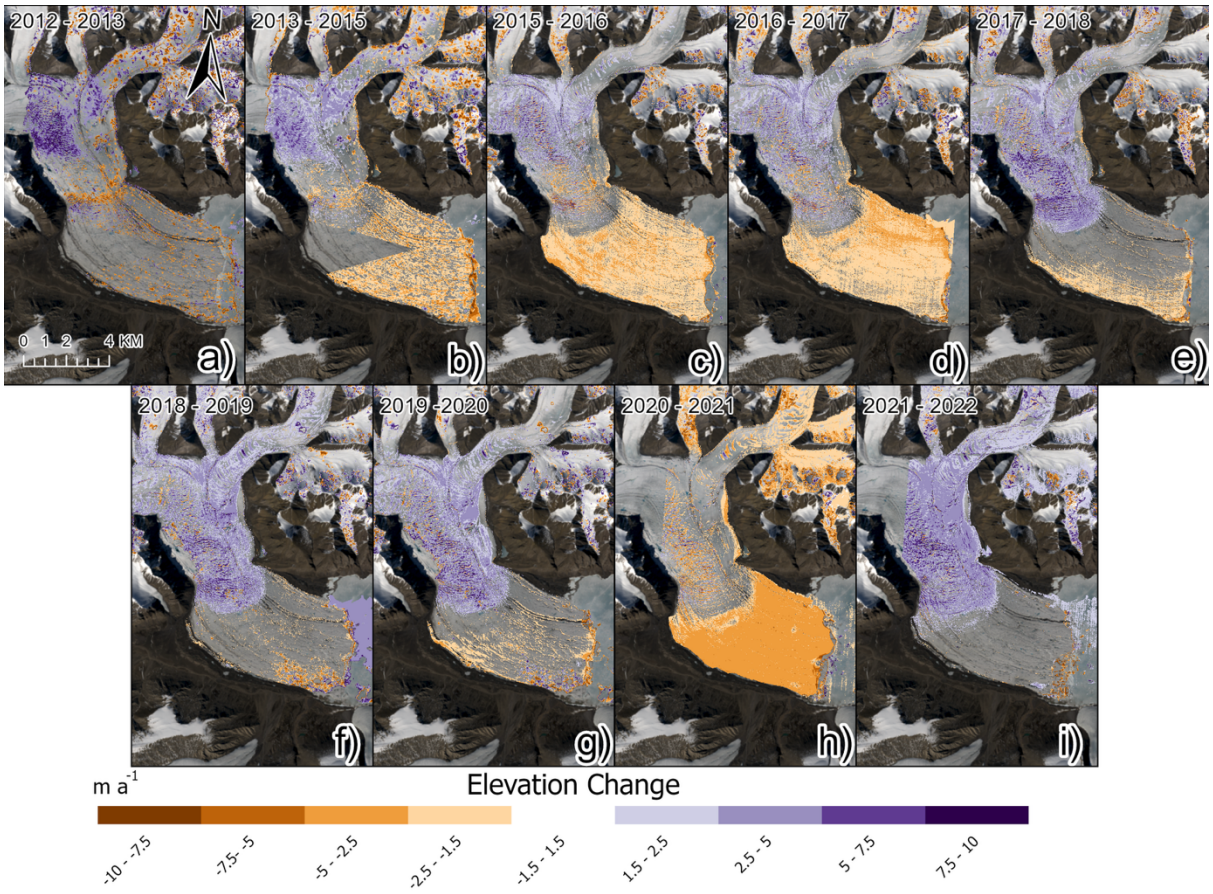


Figure 4-15: Surface elevation change composite of Eugenie Glacier, derived from xDEM. Overlaid on Landsat 8 imagery collected June 2, 2019.

4.3.2 Eugenie Glacier Ice Velocity

Measurements of ice velocity for Eugenie Glacier show two periods with distinct ice-flow regimes (Figure 4-16). From 2000 to 2008, ice velocities were relatively fast over a large part of the glacier, while from 2009 to 2022, velocities in the terminus region and lower trunk decreased significantly, and the velocities in the transverse and upper trunk decreased as well, albeit to a lesser degree (Figure 4-16).

More granularly, in 2000, at the start of the observation period, Eugenie Glacier was observed to have surface ice velocities of 400 m a^{-1} across the terminus region. Velocities

increase when transitioning to the lower trunk section, with velocities of 700 m a^{-1} being measured, before slowing back down to 400 m a^{-1} moving further upglacier (Figure 4-16). Through the transverse trunk, velocities gradually slow to 300 m a^{-1} before reaching the upper trunk. Velocities decrease further along the upper trunk to 200 m a^{-1}. From 2001 to 2007, the velocity structure described for 2000 remained largely consistent, with higher velocities recorded between the terminus region and the lower trunk (Figure 4-16 b-h). The glacier's lowermost velocity structure starts to deviate from this overall pattern in 2008 (Figure 4-16i), with the terminus region decelerating to 100 m a^{-1}, while the rest of the glacier was largely unaffected. The lower trunk slowed slightly to 150 m a^{-1}, but in the transition zone between this region and the transverse trunk, ice flow speeds of 300 m a^{-1} were maintained. Velocities gradually decrease from this point upward, with the rest of the transverse trunk slowing down to velocities of 150 m a^{-1}, which is maintained through the upper trunk. The next year with large decelerations is 2010 (Figure 4-16k), when the terminus slows to near stagnant levels of 20 m a^{-1}. The lower and transverse trunks also experience slower velocities of 100 m a^{-1} and 140 m a^{-1}, respectively. Even though all lower regions of Eugenie Glacier slowed down, the upper trunk only slowed down slightly to 140 m a^{-1}. From 2012 to 2022 (Figure 4-16 m-w), the velocity structure of Eugenie Glacier was largely consistent, with the terminus region having velocities indicating stagnation in this region (~20 m a^{-1}), and flow speeds of 50 m a^{-1} to 100 m a^{-1} along much of the rest of the glacier.

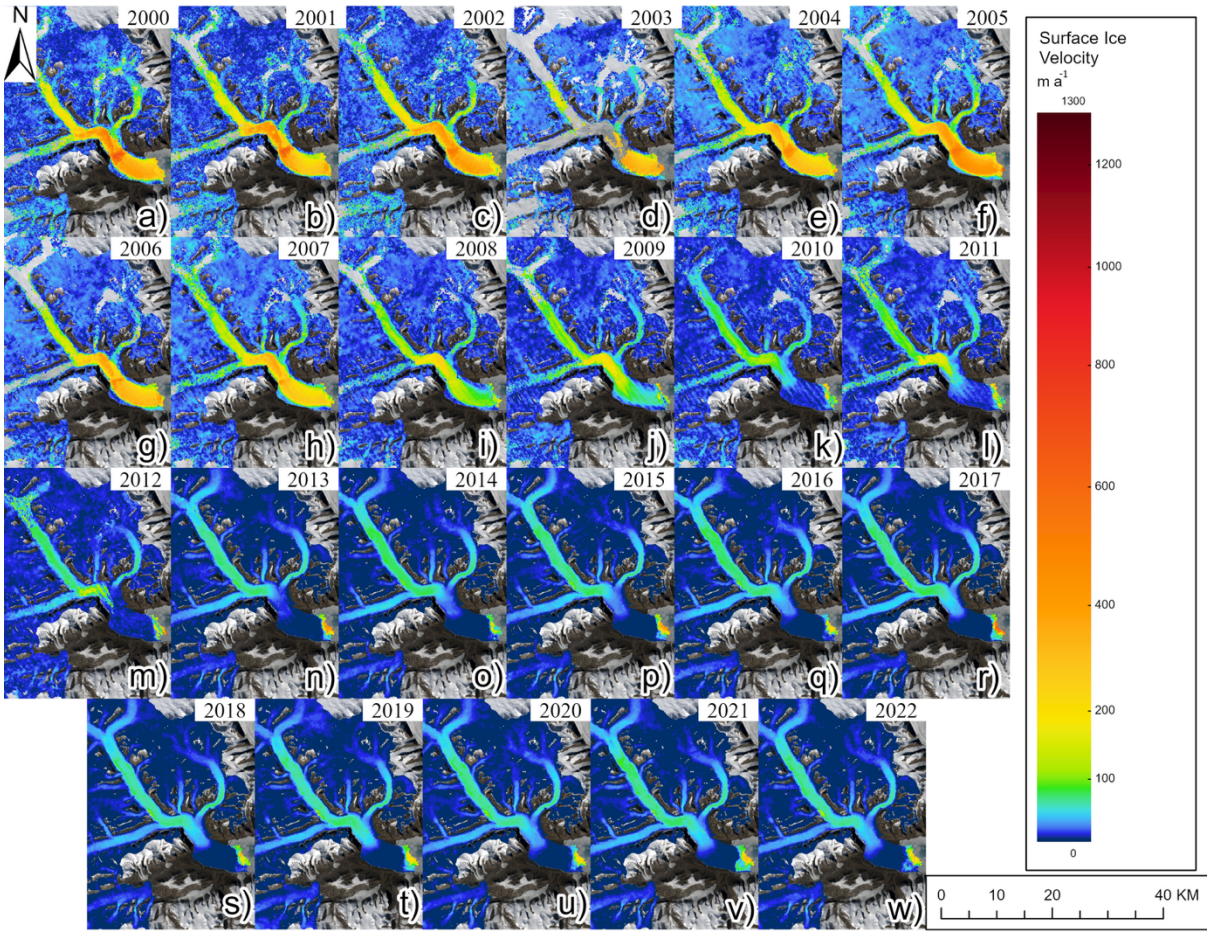


Figure 4-16: ITS_LIVE composite velocity products by NASA JET Propulsion Laboratory, covering Eugenie Glacier from 2000 to 2022, derived from optical imagery. Each image is the average surface ice velocity collected over the year. Overlaid on Landsat 8 imagery collected June 2, 2019.

4.2.3 Eugenie Glacier Terminus Positions

Figure 4-17 presents the evolution of Eugenie Glacier's terminus position from 1959 to 2024. Eugenie Glacier has the least coverage from before 2000. The evolution of Eugenie Glacier's terminus can be broadly grouped into four phases: retreat from 1959 to 1988; an advance from 1988 to 1999 (uncaptured in detail in imagery); stability from 1999 to 2008; and retreat again from 2009 to 2024.

In 1959, the terminus is near the maximum extent captured in the study, with the northern and southern portions extending farther than the middle portion (Figure 4-17). While this shape of the terminus remains the same in 1976 and 1977, the terminus recedes by a kilometre along most transects from its 1959 position (Figure 4-17a). Retreat continues into 1987 and 1988, where the terminus recedes a further 2 km along the southern transects and 1.5

km in the middle and northern regions (Figure 4-17a). Over three decades, the terminus retreated almost 3.3 km along the southern transect, 2.5 km along the centre of the terminus, and 1.5 km in the northern sections. By 1999, the terminus advanced to its maximum extent, with notable advancement along the southern and centre portions of the terminus. With both the southern and centre sections advancing 3.5 km. In the northern portion of the terminus, the glacier advances only slightly, with the direction of the advancement appearing to change. In 1988, the terminus appears to be advancing in a more northward direction, wrapping around the mouth of the valley. But in 1999, the terminus appears to be flowing more eastward, which is more in line with the rest of the terminus. In total, the northern section of the terminus advanced by ~2 km. Compared to the 1988 terminus, the shape of the terminus in 1999 is also far more jagged, with crevasses visible upglacier from the terminus. While the terminus retreats slightly between 1999 and 2008 (Figure 4-17b), the terminus position is relatively stable over this time. However, over the 1999 to 2008 period, the front of the glacier becomes more linear, and the highly digitate features of the terminus in 1999 are lost. Starting in 2009, the glacier entered another phase of retreat, which continued steadily over the next 15 years (Figure 4-17c). Over this decade and a half, the northern and southern sections retreated by nearly 3 km, while the centre of the terminus retreated by 2.5 km. In the final years of observation, the southern section of the terminus then begins to retreat faster than the other sections, retreating ~1 km further than the centre and northern sections.

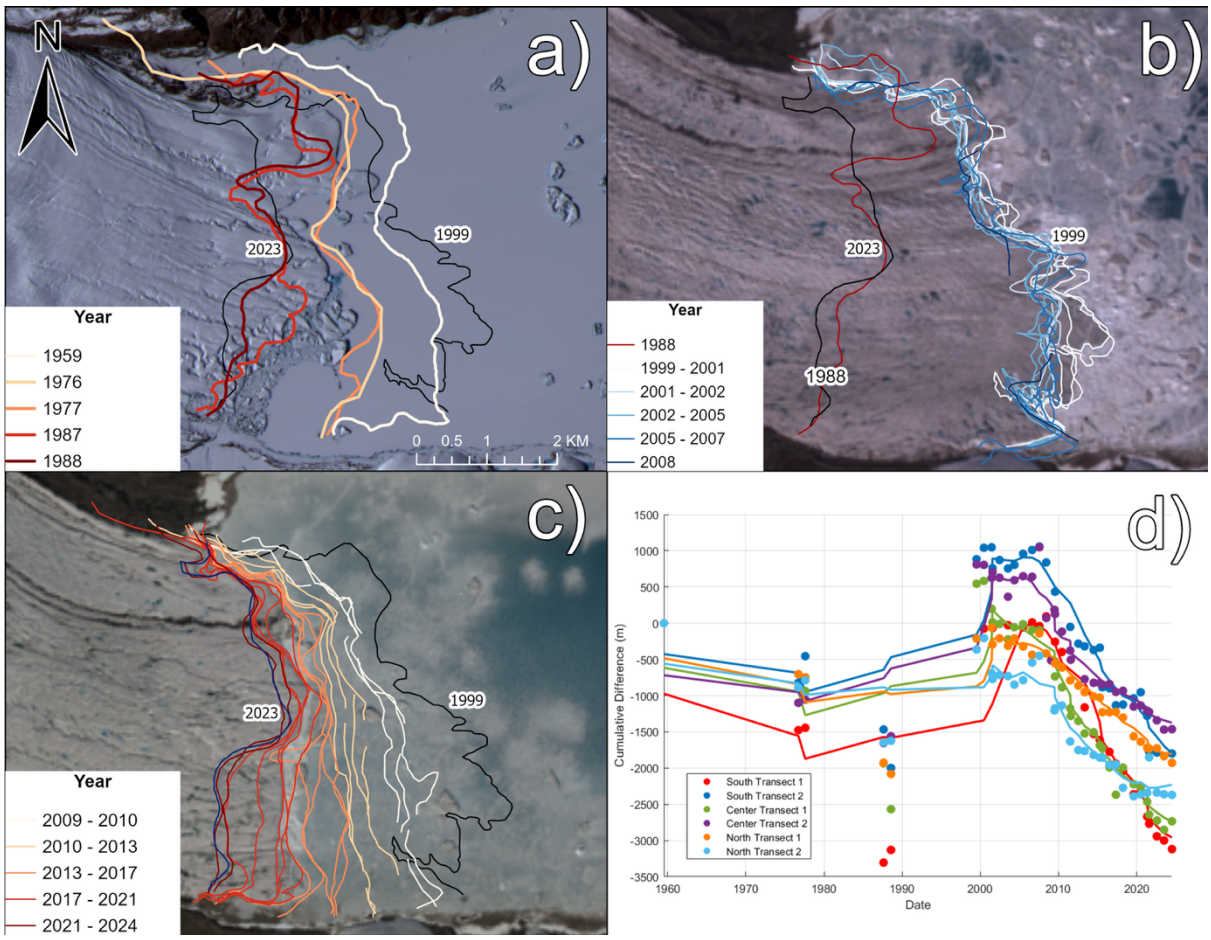


Figure 4-17: Evolution of annual terminus positions of Eugenie Glacier from 1959 to 2024. Terminus positions are grouped based on the trend of motion presented in graph d). a) spans from 1959 to 1988, b) spans from 1988 to 2008, and c) spans from 2012 to 2024. The terminus positions are overlaid on correlating satellite imagery: a SPOT, July 23, 1988, b) Landsat 7, June 16, 2000, c) Landsat 8, July 2, 2019. d) provides the terminus position along 6 transects through the glacier and compares it with the 1959 terminus position.

4.2.4 Eugenie Glacier Bed Topography

Figure 4-18 provides the subglacial topography of Eugenie Glacier clipped to the 2013 terminus extent. Within the terminus region, the deepest bed elevation is -150 m a.s.l. located 1 km from the terminus. Elevations then gradually rise to -75 m a.s.l in the upper portions of the terminus region as the direction of flow changes around the lowest bend (Figure 4-18). Within the lower trunk region there is a deep channel with a maximum depth of -125 m a.s.l. that extends for 3 km. Elevations then rise to sea level around the bend between the lower trunk and the transverse trunk (Figure 4-18). Moving upglacier to the lower trunk, another deep channel is found, reaching depths of -150 m a.s.l. This channel persists along the entire

transverse trunk for 5 km. Following the final bend into the upper trunk, elevations rise to sea level within 3 km and then gradually climb to the main body of Eugenie Glacier.

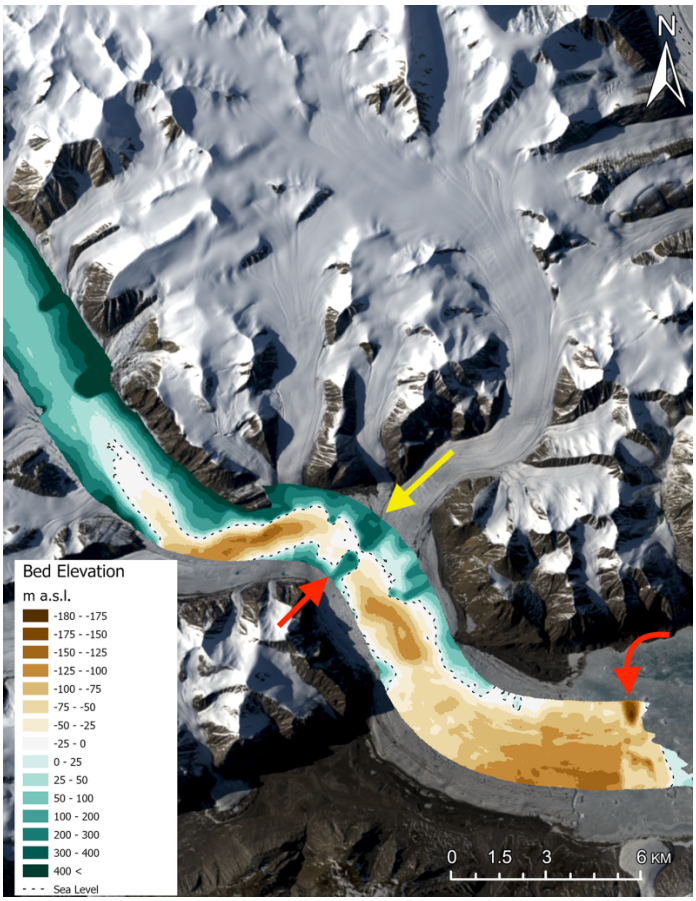


Figure 4-18: Subglacial topography of Parrish Glacier, from the CReSIS MCoRDS sensor, acquired in 2014. Regions of potential error are denoted by a red arrow, and questionable areas by a yellow arrow. Sea level is denoted by a dotted line. Overlayed on Landsat Imagery (June 2, 2019).

There are two regions in the bed data where there are likely issues with the data: at the terminus and at the bend between the lower trunk and the transverse trunk (marked with yellow and red arrows in Figure 4-18). The error at the terminus is present along the northern edge and suggests that there is a hole with a depth of -175 m a.s.l. This section of the raster is most likely a processing error, as the elevation of the bed rises and falls by 150 m a.s.l within 0.5 km, which seems implausible. The second error is located at the bend between the lower trunk and the transverse trunk, where elevations are measured to rise to 400 m a.s.l. connected to the southern valley wall, this high-elevation error would directly block the central flow channel of

Eugenie Glacier. Along the northern valley wall, patches of similar elevation are present, but because exposed bedrock is visible in optical imagery, these elevations are plausible.

4.4 Summary of Results

Chapter 4 advanced objective 1, which was to create a record of mass build-up, ice velocity and terminus position change for Dobbin Bay, Eugenie and Parrish glaciers. Along with the subglacial topography, the data presented here allow for the spatial and temporal comparison and understanding of the dynamic periods for the three glaciers. The next chapter will undertake these comparisons and place them within the context of dynamic instability literature within the Canadian Arctic.

Chapter 5 – Discussion

Chapter 5 addresses thesis objectives 2 and 3, which are to spatially refine the regions where 'pulse-type' behaviour is observed for the three study glaciers and to further characterize and distinguish pulse signals among the three glacier basins. Before establishing pulse regions, the pulse phase will be defined using the results of Chapter 4. Following this, similarities and differences between study glaciers and pulse events will be presented and discussed. Finally, pulse-type glaciers will be compared to other unstable glaciers in the CAA to further understand the unique dynamics of the study glaciers.

5.1 Pulse Event Identification

Based on the observations presented in Chapter Four, along with observations from Van Wychen et al. (2016), regions that experience pulse dynamics are defined as: sections of the glacier where velocity deviates by 400 m a^{-1} or more between active and quiescence phases, where surface elevation changes cannot be explained by surface mass balance processes, and where the glacier bed typically features a prominent subglacial feature (i.e., a subglacial bump or ridge). The onset of a pulse event is defined as occurring when the pulse region's surface ice velocity is double the speed of the upper valley's velocity and when the terminus begins to advance. Termination of a pulse event is defined here when the surface ice velocity of the pulse region is half the speed or slower than the upper portions of the glacier valley. In cases where velocity records are unreliable for determining velocities across the glacier, the findings of Van Wychen et al. (2016) are used to augment estimates of the onset of a pulse event for each glacier.

5.1.1 Dobbin Bay Glacier 'Pulse' Event / Dobbin Bay Glacier Pulse Evidence

Based on the results presented in Chapter 4, Dobbin Bay Glacier's 'pulse region' is defined spatially from 6 km from the terminus to 10 km from the terminus. This region is centred over the subglacial bump present at 7.5 km from the terminus, where the bump rises to

30 m a.s.l. (Figure 5-1a). Preceding and following the subglacial bump, bed elevations fall to -100 m a.s.l. On the lee side of the bump, surface ice velocities start to deviate, rising to a difference of 400 m a^{-1} at the lower section of the pulse region (Figure 5-1b). In terms of surface elevation, mass builds up on the stoss side and over the top of the bump at a rate of 3–4 m a^{-1} (Figure 5-1c).

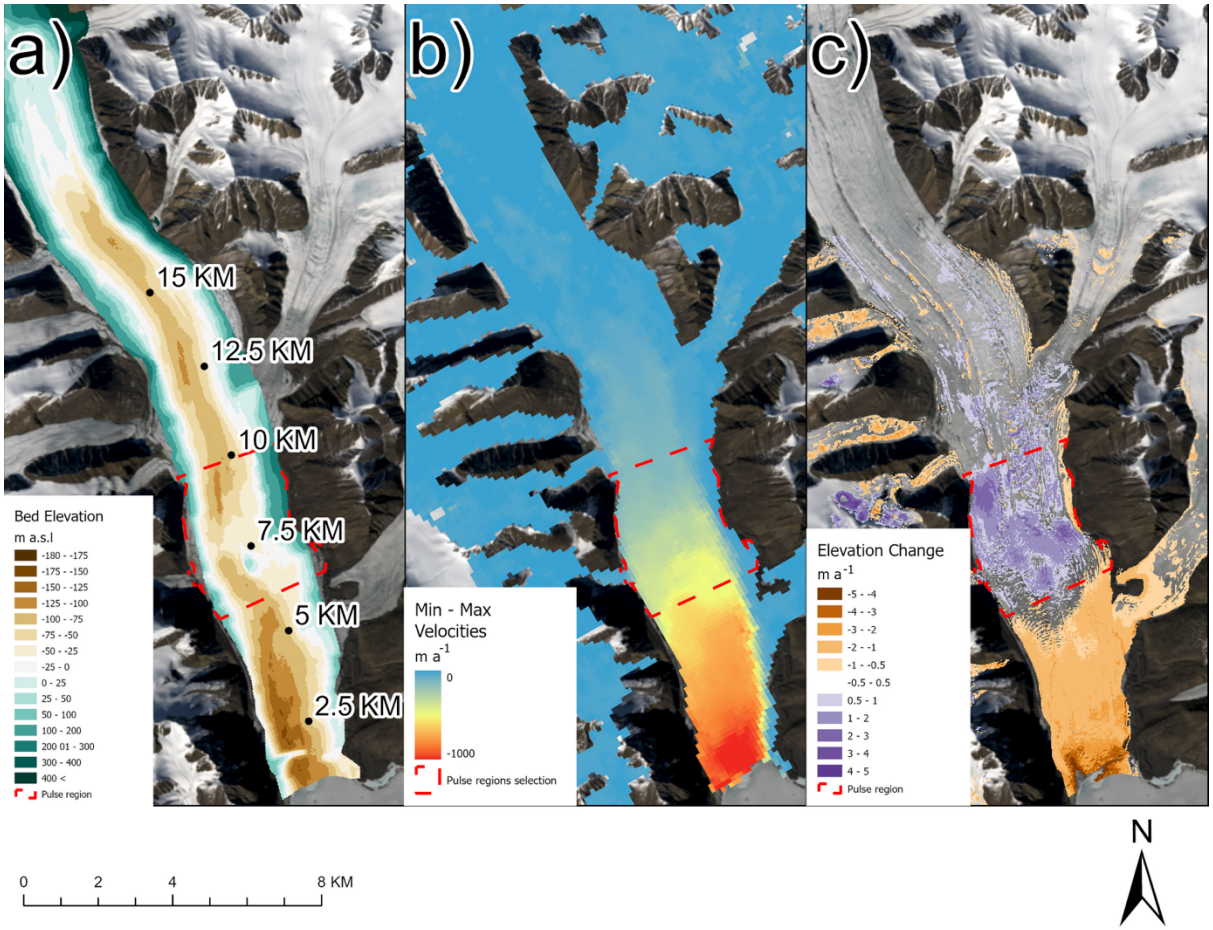


Figure 5-1: Velocity variability, bed geometry and decadal elevation differences of the bottom 15 km of Dobbin Bay Glacier. Velocity variability was collected from the maximum and minimum velocities experienced across the annual velocity records. Markers along the centerline of the glacier are placed at intervals of 2.5 km. Overlayed on Landsat Imagery (June 2, 2019).

As seen in Figure 5-2, from 1959 to 1999, the terminus of Dobbin Glacier retreated, but in 2003 the pattern changed, with slight advancement beginning. During this time, velocities in the 2.5 km closest to the terminus began flowing faster (Figure 5-2). The following year, the terminus slightly advances as velocities in the lowermost 5 km portion of the terminus double, with the highest speeds achieved being 400 m a^{-1}. 2005 is when the rate of terminus

advancement and velocity change peak (Figure 5-2), with speeds reaching 1100 m a^{-1}, and reducing down to 200 m a^{-1} by 10 km from the terminus. Glacier velocities declined through 2006 and 2007, while the rate of advancement continues before slowing in 2009. Following 2009, the terminus transitions to retreat while velocities in the pulse region slow to near-stagnant levels of <20 m a^{-1}. Based on this collection of evidence, the pulse of Dobbin Bay Glacier occurred from 2004 to 2008.

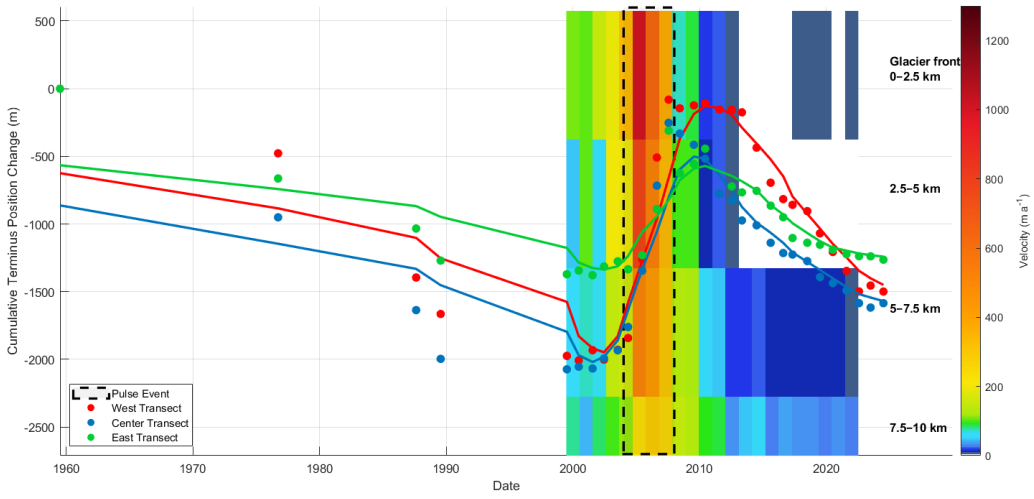


Figure 5-2: The terminus evolution of Dobbin Bay Glacier from 1959 to 2024, overlaid on the annual surface ice velocity extracted every 2.5 km along the centerline of Dobbin Bay Glacier. The active phase of the pulse is denoted by the black dashed line.

5.1.2 Parrish Glacier 'Pulse' Event

Parrish Glacier's pulse region is spatially defined as the area from 7.5 km from the terminus to 12 km from the terminus (Figure 5-3). As seen in Figure 5-3a, a subglacial sill at an elevation of -50 m a.s.l is present at 10 km from the terminus. The bed elevation on the lee and stoss side of this sill falls to -100 m a.s.l. Surface ice velocities begin to diverge further over top of the subglacial sill, increasing to 600 m a^{-1} (Figure 5-3b) and continue to deviate further down the glacier. In this region, elevation change rates peak at 4 m a^{-1} (Figure 5-3c), with high elevation gain continuing 2 km following the sill. Notably, this region also

experiences a 27° turn in the glacier valley (Figure 5-3 b). On the inside valley wall of this turn (west side), elevation gain persists over a larger area, extending 2 km farther up the glacier.

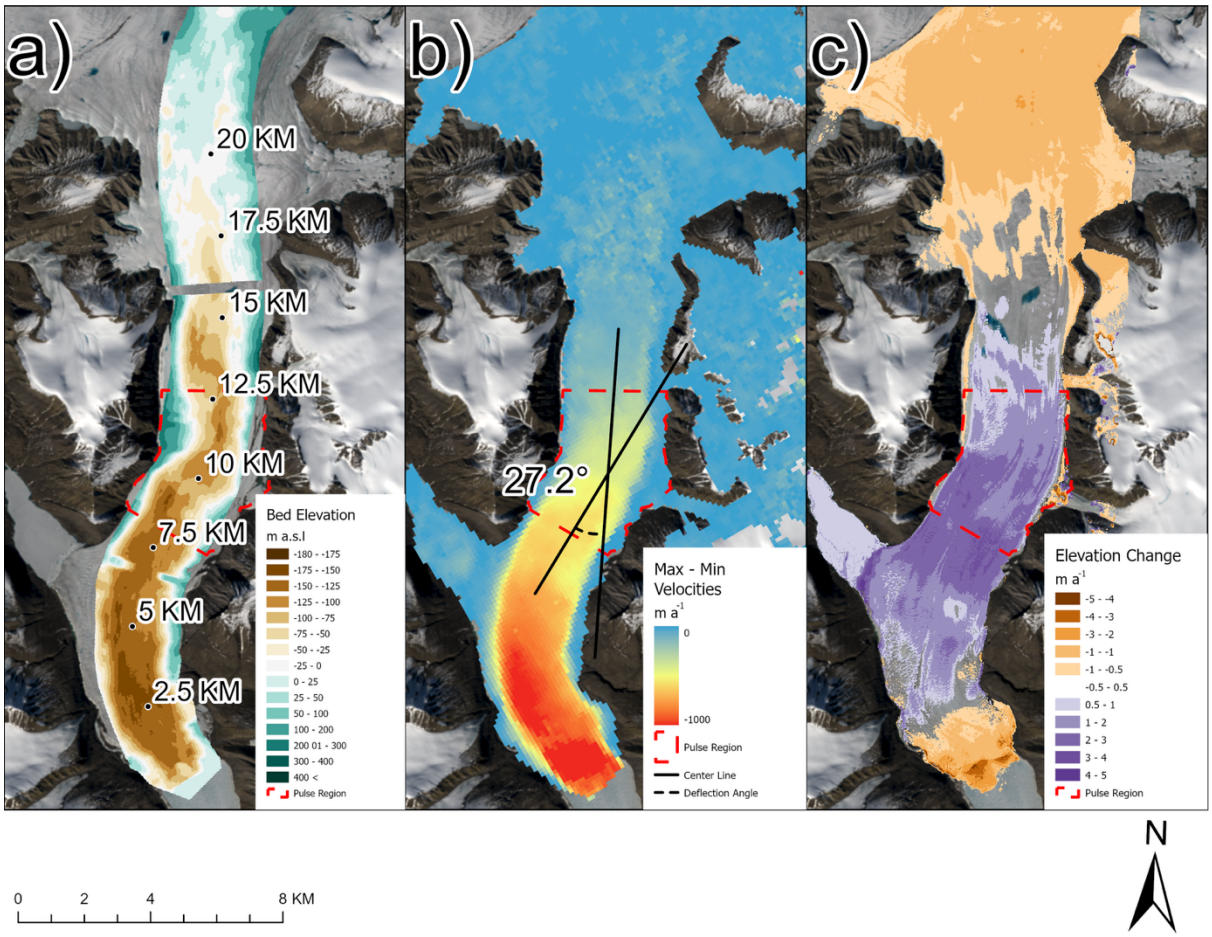


Figure 5-3: Velocity variability, bed geometry and decadal elevation differences of the bottom 15 km of Parrish Glacier. Velocity variability was collected from the maximum and minimum velocities experienced across the annual velocity records. Markers along the centerline of the glacier are placed at 2.5 km intervals. Overlayed on Landsat Imagery (June 2, 2019).

When evaluating the evolving terminus positions and glacier velocities, Parrish Glacier's pulse event can be temporally defined as occurring from 2004 to 2010 (Figure 5-4). As seen in Figure 5-4, the terminus of Parrish Glacier experienced retreat from 1959 to 2003 but transitioned into a period of advance in 2004. During 2003, the bottom 5 km of Parrish began to accelerate to 200 m a^{-1}, while in previous years, ice velocities were 50 – 100 m a^{-1} (Van Wychen et al, 2016). 2004 is when the bottom 10 km from the terminus began to accelerate, with the region reaching velocities of 400 m a^{-1}. In response to higher velocities, the terminus of Parrish Glacier then advances nearly 400 m. In the two following years, the

velocities of the bottom 10 km of the glacier continue to accelerate, peaking at 1000 m a^{-1} by 2007. While the bottom 5 km of the glacier slowed down by 2010, the terminus continued to slightly advance, reaching peak extent in 2012, and then began to retreat. Throughout the 6-year pulse period, Parrish Glacier advanced ~2.5 km, with velocities exceeding 1000 m a^{-1}, all while the upper regions of the glacier remained at speeds experienced during quiescence.

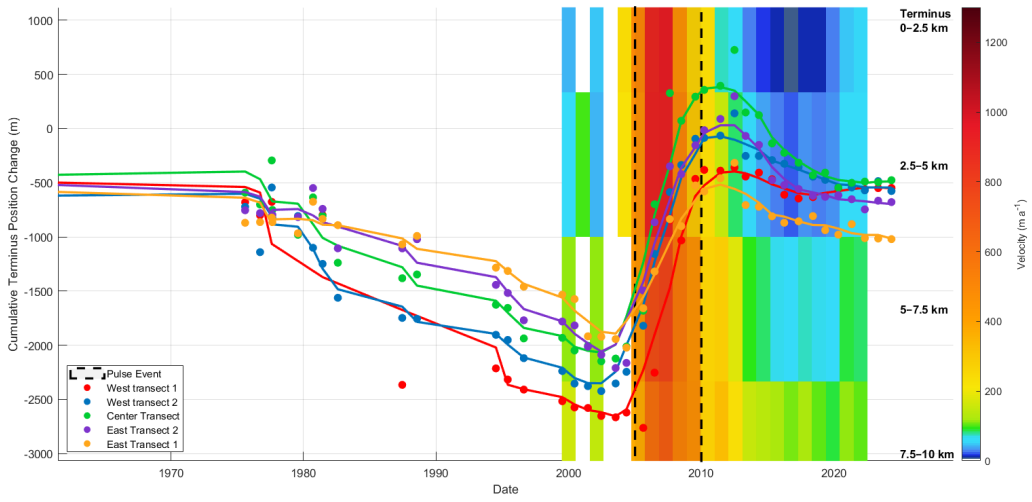


Figure 5-4: The terminus evolution of Parrish Glacier from 1959 to 2024, overlaid on the annual surface ice velocity extracted every 2.5 km along the centerline of Parrish Glacier. The active phase of the pulse is denoted by the black dashed line.

5.1.3 Eugenie Glacier 'Pulse' Event

The pulse region of Eugenie Glacier is slightly different from that of the other two study glaciers but is spatially defined as the area located between 7.5 km and 13 km from the terminus (Figure 5-5). The bed topography has two notable features: two subglacial depressions dipping to -75 m a.s.l at 10 km and at 15 km from the terminus (Figure 5-5a). These channels are roughly 2 km long, with elevations reaching sea level at both ends. The two subglacial channels are interrupted by a 70.5° turn in the valley (Figure 5-5 b), where bed elevations reach sea level and then rise above sea level. Downglacier of this bend is the area where there is the greatest amount of variability in glacier flow speed between pulse periods and quiescent periods. With velocities reaching 500 m a^{-1} following the subglacial sill and roughly maintaining that surface

ice velocity through to the terminus (Figure 5-5b). At the bend and subglacial sill, elevation change is 3.5 m a^{-1} and increases on the lee side of the sill at a rate of 4 m a^{-1} (Figure 5-5c).

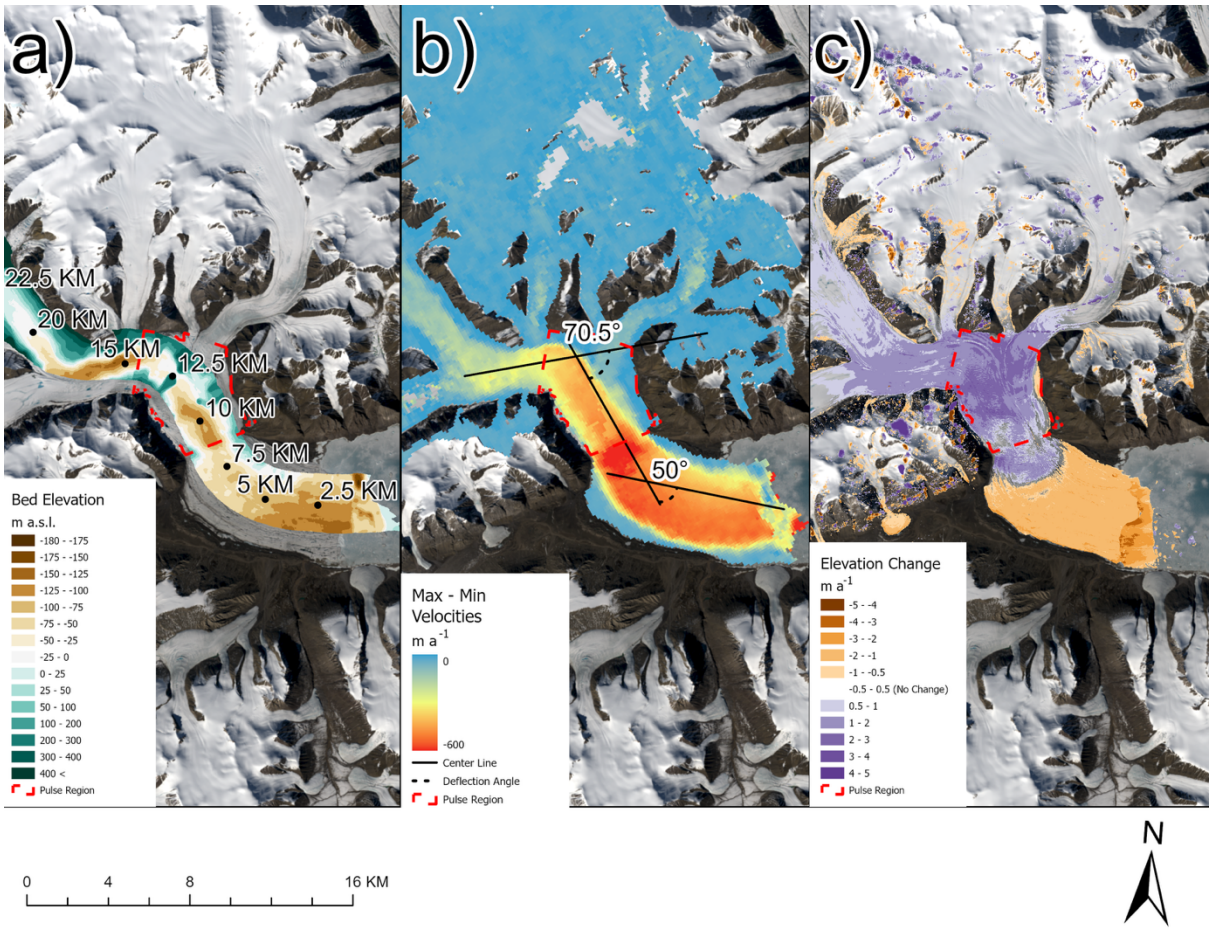


Figure 5-5: Velocity variability, bed geometry and decadal elevation differences of the bottom 15 km of Eugenie Glacier. Velocity variability was collected from the maximum and minimum velocities experienced across the annual velocity records. Markers along the centerline of the glacier are placed at 2.5 km intervals. Overlayed on Landsat Imagery (June 2, 2019).

Based on the terminus positional change analysis and the glacier velocity record, it is determined that Eugenie Glacier experienced a pulse event sometime between the late 1980s and 2000, ending in 2008. The velocity data and the terminus evolution graph suggest that by the time imagery used in this study was acquired, a pulse event was already underway, as a terminus advance of 2-4 km occurred between 1987 and 2000. While the terminus advances from 2000 to 2003 across northern sections, the rest of the glacier remained stable. From 2000 to 2008, the bottom 10 km also experienced higher velocities at 500 m a^{-1}. No observable peak in velocities was observed within the bottom 10 km of the glacier, with velocities remaining at

roughly 500 m a^{-1}, between the pulse region and the terminus. Following 2008, the terminus began to retreat while surface ice velocities in the bottom 7.5 km of the glacier decelerated to 100 m a^{-1}. In 2009 and 2010, the deceleration of ice velocities was highest at the terminus, with a slight decrease farther up the glacier. Although the beginning of the pulse is not identifiable, it began pulsing before 2000 and ended in 2008.

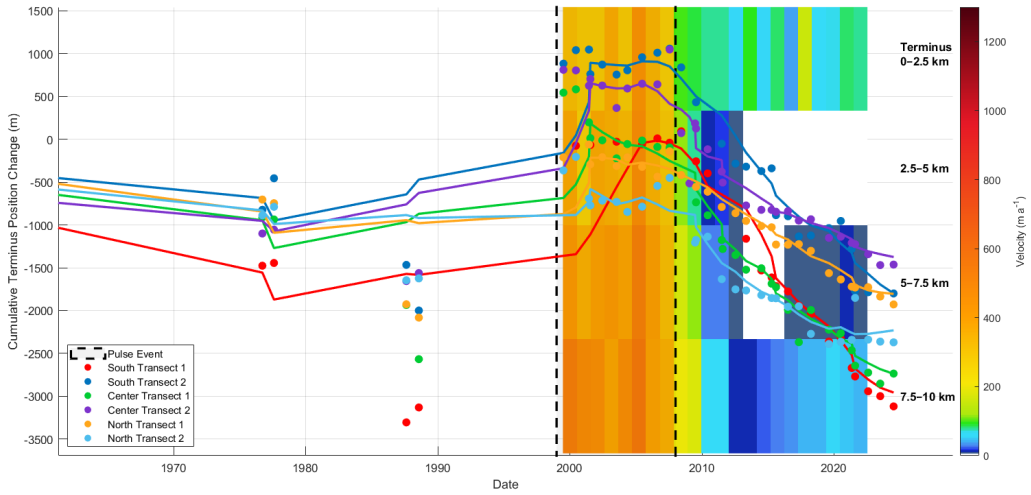


Figure 5-6: The terminus evolution of Eugenie Glacier from 1959 to 2024. Overlaid on the annual surface ice velocity extracted every 2.5 km along the centerline of the glacier. The active phase of the pulse is denoted by the black dashed line.

5.1.4 Dynamic event summary

Pulse initiation regions on each glacier have been identified as shown in Figure 5-7. Dobbin Bay Glacier's pulse initiation region is present from 6 km to 10 km from the terminus, Parrish Glacier's pulse initiation region is present from 7.5 km to 12 km from the terminus, and Eugenie Glacier's pulse initiation region is present from 8 km from the terminus to 13 km from the terminus. Notably, subglacial sills were present within the pulse region of each glacier and during quiescence, the highest rates of surface elevation gain were recorded over the sills. Furthermore, during the pulse phase, the sill locations seem to be an important subglacial feature given that surface ice velocities would begin to increase downglacier of the sill.

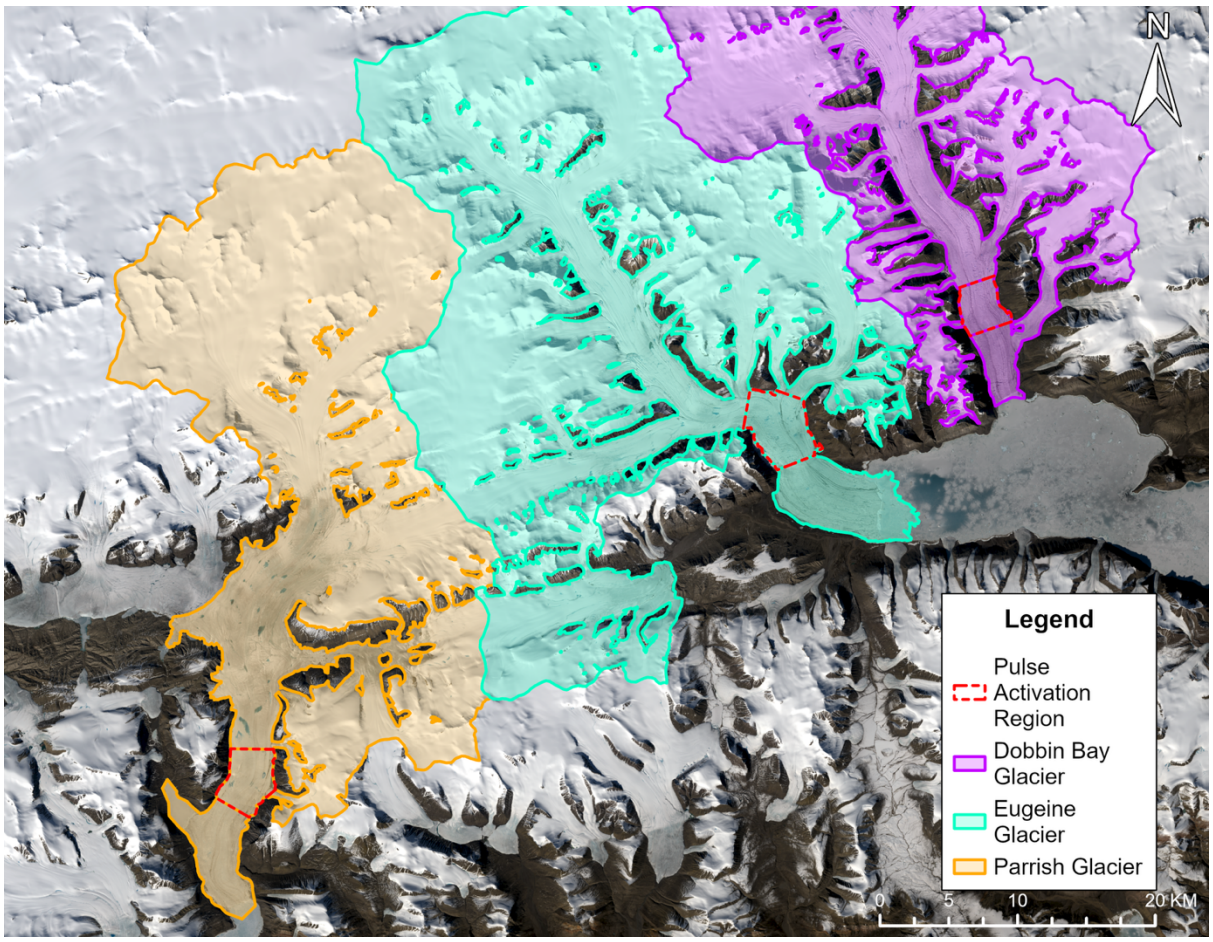


Figure 5-7: Pulse Activation Regions of the study glaciers: Dobbin Bay, Parrish, and Eugenie. Overlayed on Landsat 8 Imagery (June 2, 2019).

As shown in Figure 5-8, the pulse phases for the study glaciers are as follows: Dobbin Bay Glacier from 2004 to 2008, Parrish Glacier from 2004 to 2010 and Eugenie Glacier from before 2000 to 2008. In all study glaciers, the pulse region experienced heightened velocities and advancing terminus during these times. Outside pulse events, glacier velocities were slower than those experienced upglacier of the pulse region.

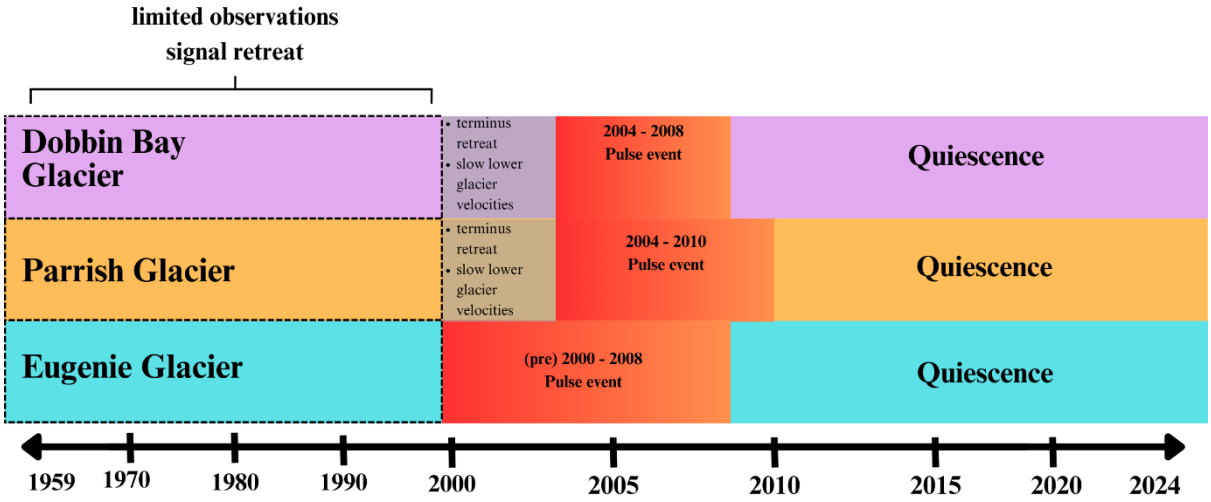


Figure 5-8: Summary of interpreted pulse-type activity for Dobbin Bay Glacier (purple), Eugenie Glacier (blue) and Parrish Glacier (orange), from 1959 to 2024.

5.2 Comparisons of 'Pulse' Dynamics

To further understand pulse dynamics, the dynamic behaviour will be compared and contrasted between the three study glaciers.

5.2.1 Similarities between all study glaciers

The primary common feature between the three study glaciers is the presence of a subglacial ridge or bump in the area where the greatest amount of dynamic variability is observed. On Dobbin Bay Glacier, the subglacial bump is present at 7 km from the terminus; for Parrish Glacier, the subglacial ridge is present at 10 km from the terminus; and for Eugenie Glacier, the ridge is present at 12.5 km from the terminus (Figure 5-9).

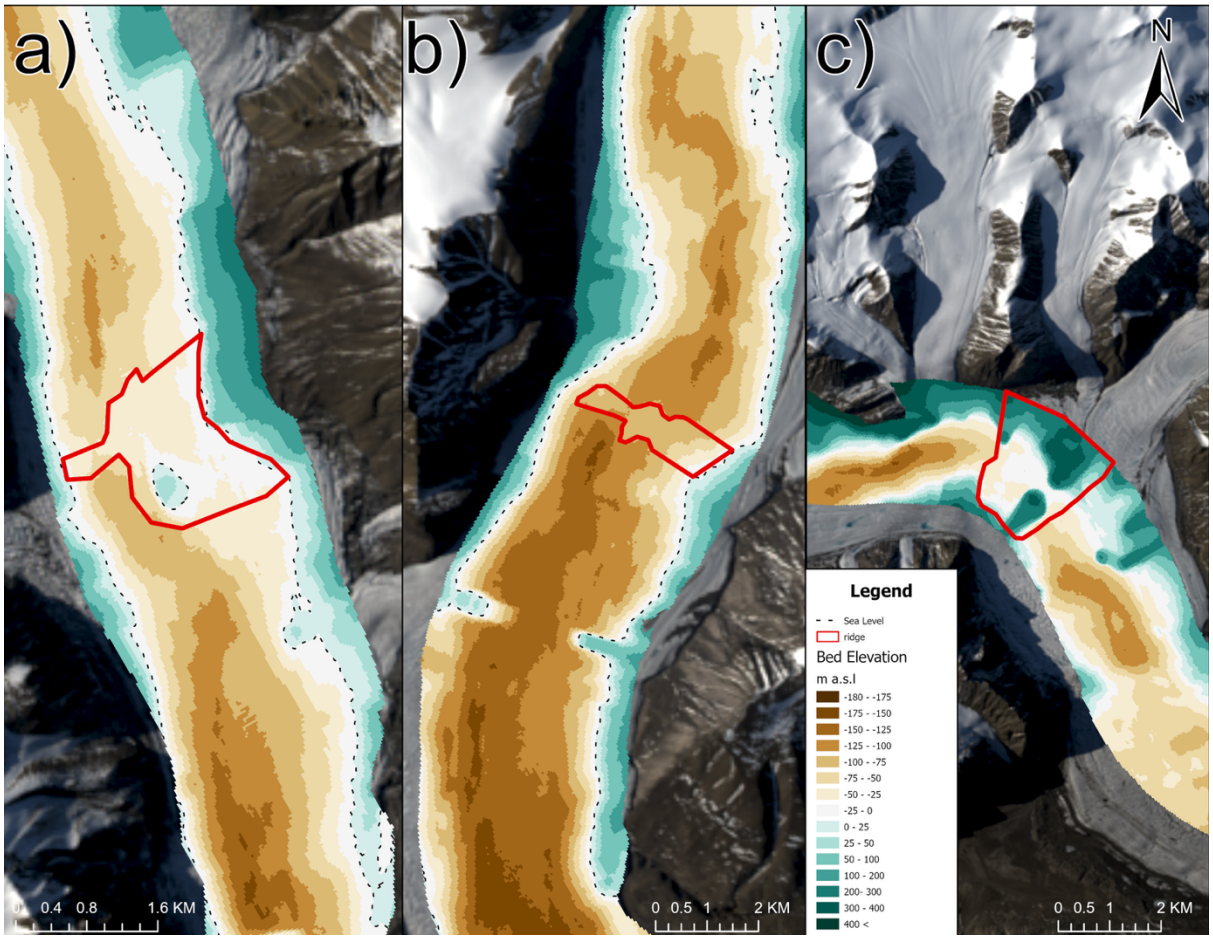


Figure 5-9: bed topography with highlights of subglacial ridges of: a) Dobbin Bay glacier, b) Parrish Glacier, c) Eugenie Glacier. Overlayed on Landsat Imagery (June 2, 2019).

Dobbin Bay Glacier's subglacial bump reaches an elevation of 25 m a.s.l., Parrish Glacier's ridge reaches an elevation of -25 m a.s.l., and Eugenie Glacier's ridge reaches an elevation of 0 m a.s.l. For all three study glaciers, this subglacial feature interrupts subglacial topography that is relatively deep. These abrupt changes in subglacial elevation are where irregular dynamics are most highly concentrated and are also where there are significant differences between surface elevation thinning and thickening. As shown in Figure 5-10, surface ice velocities decrease at the subglacial sill during quiescence and then accelerate during the pulse phase. This is primarily seen in Figure 5-3 for Dobbin Bay and Figure 5-5 for Parrish glaciers. Finally, during quiescence, the terminus regions of all three glaciers approach stagnation, flowing at surface ice velocities <20 m a^{-1}. The stagnant region varies in length on each glacier, occurring in Dobbin Bay Glacier's lowest 5 km, Parrish Glacier's bottom 2.5 km,

and Eugenie Glacier's bottom 7.5 km. All of these regions are present downglacier of the high-elevation subglacial feature. As velocities fall to near-stagnant levels during quiescence, the subglacial features in pulse-type glaciers seemingly act as barriers, preventing ice flow into the lower regions of the glacier. This pattern was similarly identified in Van Wychen et al., (2016) where it was observed that the velocity variability was not transferred upglacier of the subglacial sills of Dobbin Bay and Parrish Glacier. Here it was similarly suggested that the subglacial sill act as a hinge point preventing the spread of elevated surface velocities upglacier (Van Wychen et al., 2016).

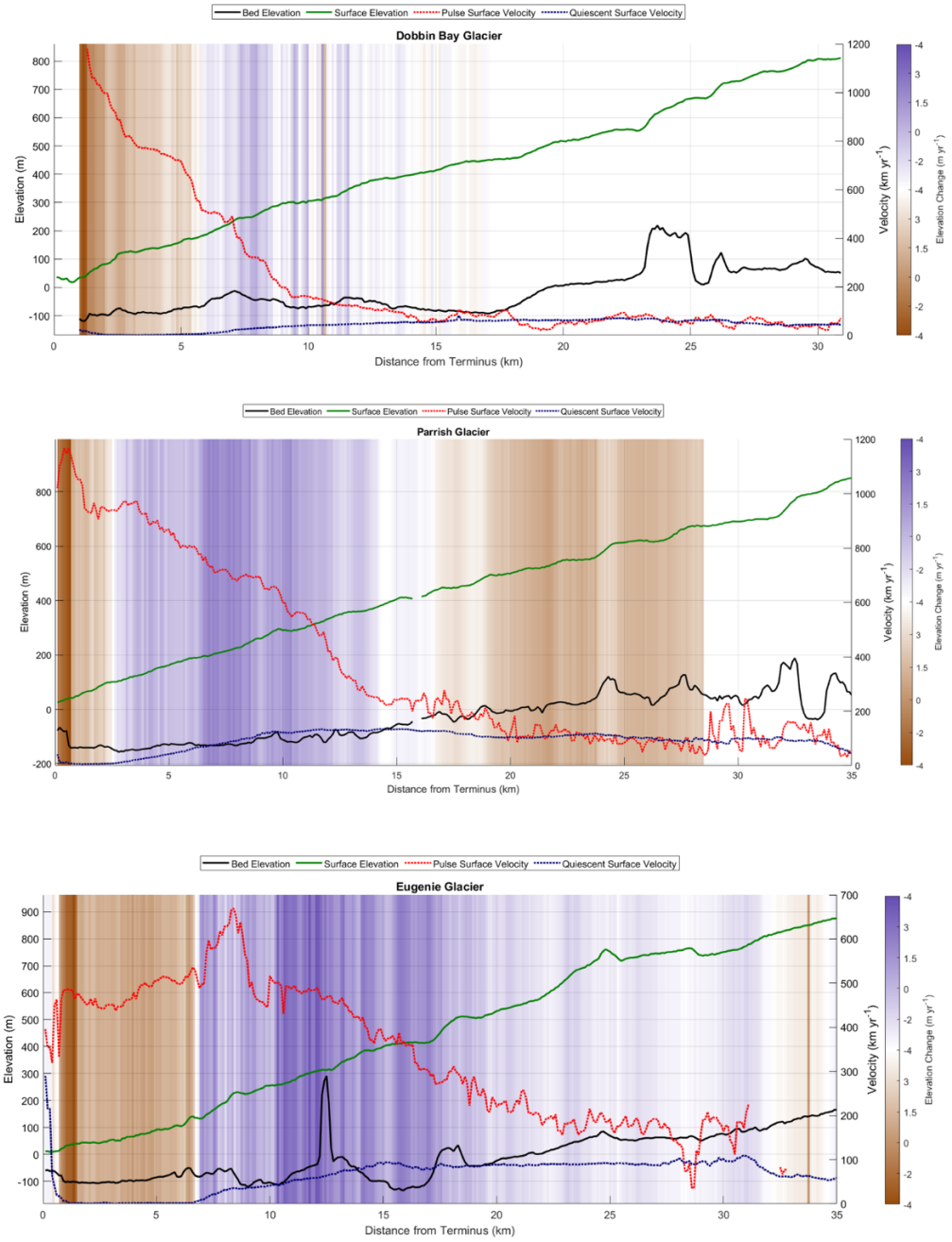


Figure 5-10: Graphs for each study glacier, comparing bed elevation to decadal elevation change and surface ice velocities during pulse and quiescence. All values were pulled along the centerline of the glacier, which is tracked along the x-axis. The left y-axis provides the elevation reading of the surface (green line) and bed(black line) of the glacier. Surface ice velocities are tracked along the right y-axis, with the dotted red line representing velocities during a pulse event and the dotted black line representing quiescent velocities. The decadal elevation change is represented by the colour map scaling from brown to purple.

5.2.2 Similarities between Dobbin Bay and Parrish Glaciers

Between the three study glaciers, Dobbin Bay Glacier and Parrish Glacier are more similar to each other, with both glaciers reaching speeds faster than 1000 m a^{-1}. These active phase velocities are relatively high compared with those of regional surge-type glaciers (Short and

Gray (2005) and Van Wychen et al. (2016)), but velocities exceeding 1000 m a^{-1} have been observed (Copland et al., 2024; Lauzon et al., 2023, 2024). Dobbin Bay Glacier reaches these flow speeds about 1 km from the terminus, while Parrish Glacier reaches these speeds around 2.5 km from the terminus. Both glaciers' top speeds are observed slightly offset from the centerline flow over the deepest portions of the bed topography. Both glaciers also have similar pulse lengths: 4 years for Dobbin Bay Glacier and 6 years for Parrish Glacier. While the pulse region is located at different distances from the terminus, the transition region between the pulse region and the upper glacier is of a similar length. On Dobbin Bay Glacier, this transition zone persists from 7.5 km to 10 km, and on Parrish Glacier, the zone persists from 10 km to 12.5 km. These transition zones experience slight accelerations during the pulse phase and slight elevation growth during quiescence.

5.2.3 Similarities between Parrish and Eugenie Glaciers

While Eugenie Glacier is the most different in terms of pulse dynamics, it does share a common feature with Parrish Glacier. Throughout the pulse region of both glaciers, a bend in the valley and ice flow occur. As seen in Figure 5-11, Parrish Glacier experiences a 27° offset in valley flow, and Eugenie Glacier experiences a 70.5° turn in the valley.

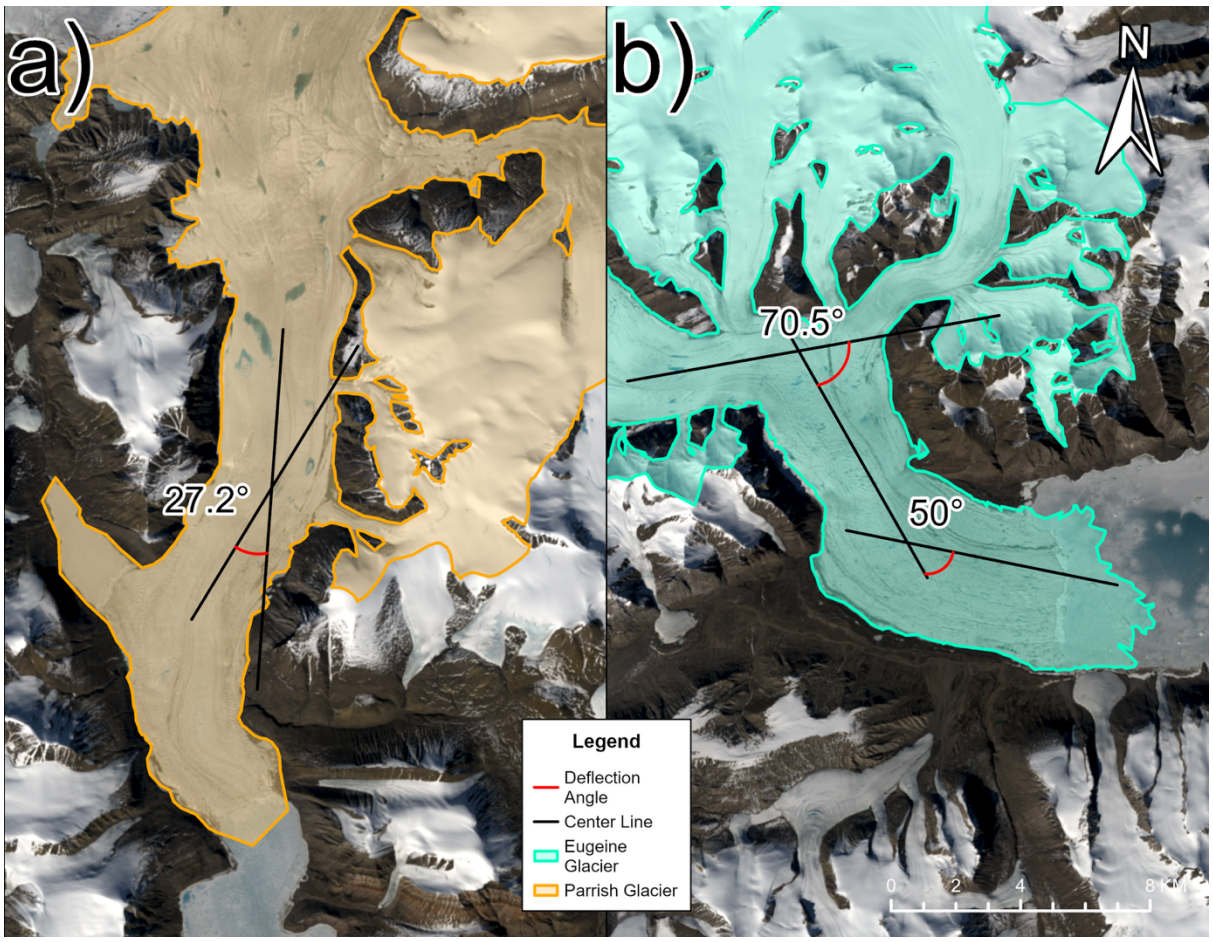


Figure 5-11: Deflection angle of the valley experienced by a) Parrish Glacier and b) Eugenie Glacier. Overlayed on Landsat Imagery (June 2, 2019).

Glacier geometry has previously been linked to potential controls of surge-type glaciers, with surge-type glaciers more likely to have multiple branches or tributaries (Jiskoot et al., 2000; Jiskoot et al., 2017; Lovell et al., 2026). The presence of a turn in ice flow due to topography could lead to higher friction between the ice and bed which may contribute to the pulse behaviour observed on these glaciers. As seen in Figure 5.3 and Figure 5.5, surface ice velocities deviate following major turns in each glacier's morphology while mass buildup begins before these bends. Given this, these constrictions in the glacier valley may contribute to, or enhance, pulse dynamics and may work together with sills to modulate ice flow behaviours.

5.2.4 Eugenie Glacier Differences

Eugenie Glacier is the most distinct from the other three study glaciers in terms of pulse dynamics. For example, Eugenie Glacier experiences both slower ice velocities during the active phase at 500 m a^{-1} and a longer pulse period lasting more than 8 years. These speeds of 500 m a^{-1} are maintained across the entire terminus region, which is notably different than the other glaciers included in the study, which sped up closer to the terminus. Although the onset of the pulse was not captured, this trend of consistent surface ice velocity persisted across all 8 years. Another notable difference is the valley morphology of Eugenie Glacier, while Parrish shares a bend in the pulse region, Eugenie's valley shape resembles more of a 'Z' Pattern creating more potential constriction points along its length. The valley experiences three regions where the flow of the ice changes direction two times over a relatively short distance, and this appears to affect the dynamics of the glacier, as both surface ice velocity and elevation change records vary at each turn in the glacier valley, more prominently during quiescence. As seen from Figure 5-8, Eugenie Glacier experiences different ice flow conditions along each turn. The upper glacier behaves similarly to both Dobbin Bay and Parrish glaciers, both in and out of pulse events. The transverse trunk portion of the valley experiences increased surface ice velocity during a pulse event but also exhibits the same velocity as the upper trunk during quiescence. The surface ice velocities of the transverse trunk, 100 m a^{-1}, are maintained up to the subglacial ridge and bend. Following this the speeds halve to 50 m a^{-1} throughout the lower trunk. Finally, velocities decrease to near stagnant levels in the bottom 7.5 km of the glacier during quiescence.

Eugenie Glacier also has the longest observed pulse phase, lasting more than 8 years. This timeframe aligns more with the active-phase periods of surge-type glaciers than with the shorter proposed pulse phases (Van Wychen et al., 2016). Compared to the other study glaciers, Eugenie Glacier's pulse phase is at least 2 years longer than Parrish glaciers' 6-year pulse phase.

Although the pulse phase is the longest among the study glaciers, Eugenie Glacier's surface ice velocity was the slowest during pulsing. This would indicate that the amount of mass moved during the pulse event may be similar, but it took longer to move through the system.

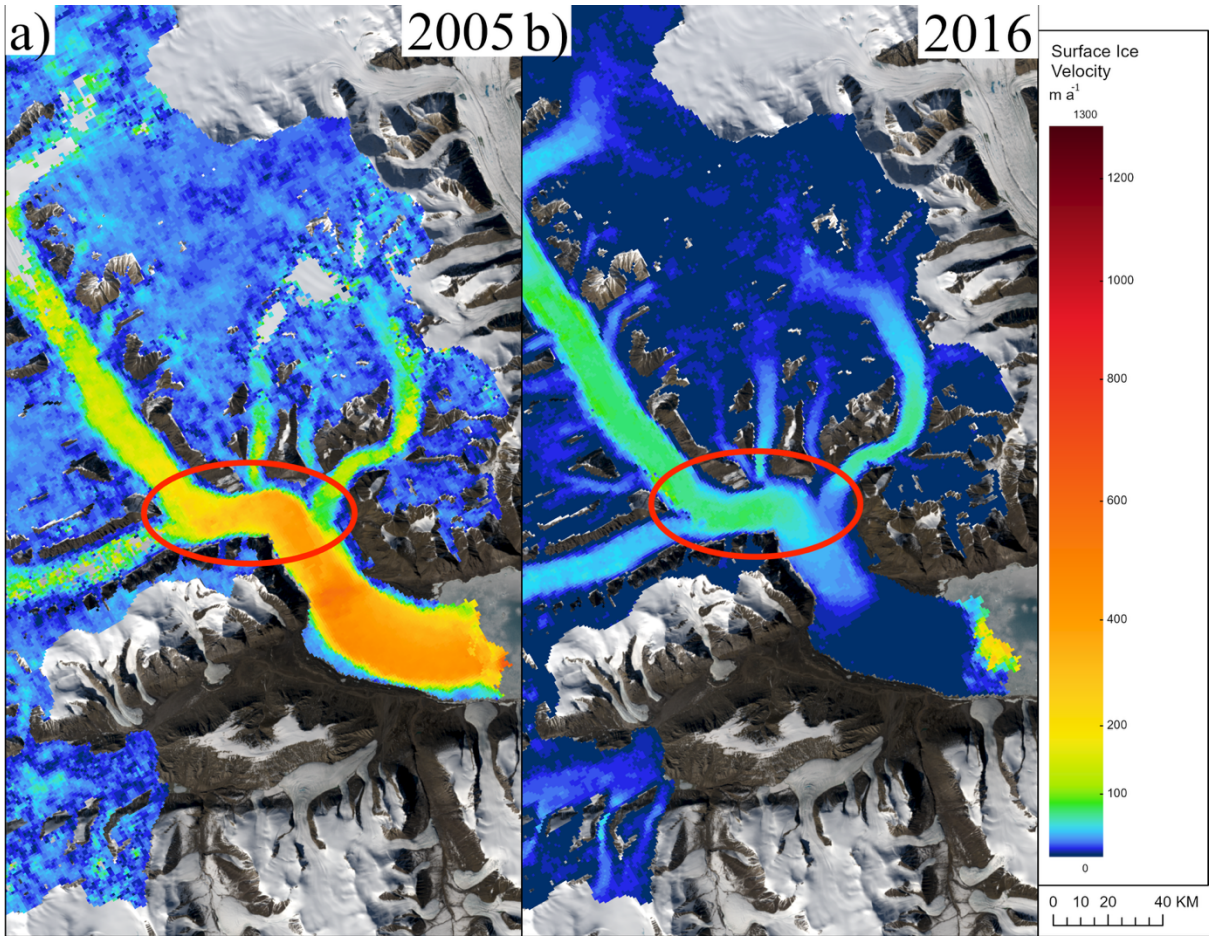


Figure 5-12: Highlight of the surface ice velocity of Eugenie Glacier's pulse region during the pulse phase a), 2005 and during quiescence b), 2016. Overlayed on Landsat Imagery (June 2, 2019).

5.2.5 Summary

All three glaciers exhibit somewhat similar dynamics, with much of the variations in ice motion occurring around subglacial sills. From a process perspective, upglacier ice seems to flow at a rate between 50 m a^{-1} to 110 m a^{-1} until reaching the subglacial sill in each glacier. During quiescence, ice mass then seems to build up at the subglacial sill as mass is prevented from flowing down the glacier from this pinning point. This causes mass losses, expressed as surface elevation lowering and terminus retreat in the lower termini of these glaciers, as mass is restricted from moving downglacier. During the pulse phase, the built-up ice on the

subglacial sill accelerates downglacier, pushing the terminus forward. For Dobbin Bay Glacier and Parrish Glacier, velocities reached speeds of 1000 m a^{-1}, while Eugenie Glacier reaches velocities of 500 m a^{-1}. Due to the irregular dynamics located at the subglacial sills, it is theorized that these bed features are driving factors in pulse-type activity, which has been previously suggested by Van Wychen et al. (2016). As exemplified by Parrish Glacier and Eugenie Glacier, the glacier's valley turn may also affect pulse-type activity. As the valley turns, friction not only builds up on the subglacial sill but also on the turns of the valley walls.

In terms of dynamics, Dobbin Bay Glacier and Parrish Glacier should be considered as prime examples of pulse-type glacier behaviour as described by Van Wychen et al. (2016). As these two glaciers experience high-velocity variability downglacier of their subglacial sills during a pulse event, they also have a relatively short pulse cycle. Eugenie Glacier, while exhibiting pulse dynamics, is slightly less clear but can be considered an edge case of a pulse-type glacier.

5.3 Contextualizing 'Pulse-Type' Glaciers with Surge-Type Glaciers

Pulse-type glaciers have only recently been reported within the wider field of glaciology, having been described only in the Canadian Arctic by Van Wychen et al, (2016) and Dalton et al. (2022). In Van Wychen et al. (2016) and Dalton et al. (2022), pulse-type glaciers were defined as having variable velocity confined to the portion of the glacier grounded below sea level. While both papers recognized and highlighted the potential importance of subglacial sills, their definitions focused more on the region where variable velocity occurs rather than identifying the constraining topography as the reason for the irregular dynamics. Based on the limited previous literature, the definition of pulse-type glaciers will be further refined based on this study in the following sections. Following this, further distinctions between surge-type glaciers and pulse-type glaciers will be made. Finally,

pulse-type glaciers and their dynamics will be contextualized within the wider understanding of irregular glacier dynamics.

5.3.1 Pulse-Type Glacier Definition

Based on the findings of Van Wychen et al (2016), Dalton et al (2022) and the findings from this study, the definition of pulse-type glaciers could be further refined to the following: *Pulse-type glaciers experience irregular dynamics downglacier of high-friction topography. Resulting in two regions of unique motion across the glacier during periods of quiescent / slowed flow, and active/fast flow*. All three pulse-type glaciers in this study exhibit nominal ice flow in line with regional averages upglacier of the constraining topography, due to a subglacial sill with potentially highly sinuous valley conditions. As a result of constraining topography, here it is suggested that the flow of ice is compressed and forced upward, increasing surface elevation on the stoss side of the feature. As this ice mass does not flow into the remaining downglacier region, this results in near-stagnant ice motion, elevation loss, and terminus recession. During quiescence, pulse-type glaciers experience two distinct ice regimes: the relatively normal flow upglacier of the constraining topography and the stagnating flow downglacier of the constraining feature. Over time, enough mass accumulates at the constraining topography to cause a kind of failure, triggering a pulse event. Pulse-type glaciers experience two different regions of ice motion during both the active and quiescent phases. In both the quiescent and active phases, velocities upstream of the sill remain at relatively normal speeds. Downglacier of the subglacial sill, velocities are stagnant during quiescence and enhanced during the active phase.

This study suggests two potential mechanisms in which pulse events are initiated: 1) enhanced basal melting and 2) critical failure. As suggested in Dalton et al (2022), as mass builds up on the stoss side of the sill, the effective melting point increases as basal pressure builds under thickening ice. This leads to localized enhanced basal meltwater production on

the stoss side of the sill. As water collects, this would decrease friction at the sill and eventually cause ice mass to flow forward, initiating a pulse event. As mass flows past the sill, so does the water that was held behind the subglacial sill. During the pulse event, the velocities increase throughout the glacier below the subglacial sill, while the region upglacier of the sill maintains relatively regular flow speeds. Eventually, the built-up mass at the sill is depleted, and high flow velocities deliver glacier mass to the terminus, eventually reaching a point where the ice is thinned enough that it is held back by the subglacial sill, terminating the pulse. To provide an analogy for the dynamics, pulse-type glaciers act like a dam and reservoir. The dam blocks water from flowing downstream, eventually causing the reservoir to overfill. Once the mass exceeds a critical threshold, the dam bursts, with water flowing rapidly downstream. Once all the water has flowed out, the dam blocks the flow, and the reservoir begins to fill again.

5.3.2 Comparing Pulse-Type Glaciers to Regional Surge-Type Glaciers

Throughout this thesis, surge-type glacier concepts have been used to describe the dynamics and mechanics observed on the study glaciers of Dobbin Bay Glacier, Parrish Glacier and Eugenie Glacier. This is because they exhibit similar irregular dynamics, with active and quiescent phases in which the glacier experiences periods of speed-up and slow-down. While exhibiting these dynamics, the results presented in this thesis, along with the results of Van Wychen et al. (2016), show that velocity variability is limited downglacier by highly constraining topography. While eight pulse-type glaciers have been identified in the CAA, it is important to understand the context of the irregular dynamics observed on the study glaciers relative to both typical and surge-type glaciers, as well as glaciers that exhibit other types of irregular dynamics in the region.

Compared with other glaciers in the CAA that exhibit irregular dynamics, surge-type glaciers have been more widely studied for a longer period of time, with regionally extensive studies such as Copland et al. (2003), Short and Gray (2005) and Van Wychen (2016). These

studies helped create an inventory and understanding of glaciers, which experience irregular dynamics throughout the CAA. In recent years, studies such as Copland et al., 2024; Lauzon et al., 2023, 2024, 2026; Medrzycka et al., 2019; and Van Wychen et al., 2022, 2025 have furthered understanding of how irregular dynamics manifest in the CAA. These studies document a wide range of irregular dynamics, which have been defined as surge-type, slow-surge, constant-acceleration, or pulse-type glaciers. While the study glaciers of this thesis have been identified as pulse-type glaciers, the observed characteristics occur in glaciers that experience different forms across a spectrum of irregular dynamics in the CAA. In terms of spatial patterns of velocity variation, the study glaciers in this thesis are most similar to the Southeast (SE-1 & SE-2) Glaciers of the Devon Ice Cap reported by Lauzon et al. (2024). In the most recent surge of SE-2, the lowermost 10 km of the glacier experienced heightened velocities, accelerating to 350 m a^{-1}, compared to the region's typical 75 m a^{-1} (Figure 5-13). This acceleration occurred gradually over 4 years, starting in 2020 and continuing through 2024. Comparing the spatial variability of heightened velocities during active phases, SE-2 experiences an expanding region that becomes activated by fast flow, whereas the study glaciers in this thesis have a fixed region of variability constrained by subglacial sills. This is because pulse events are initiated at the subglacial sill and flow downglacier, whereas SE-2 is a surge-type glacier that initiates at the terminus and propagates upglacier.

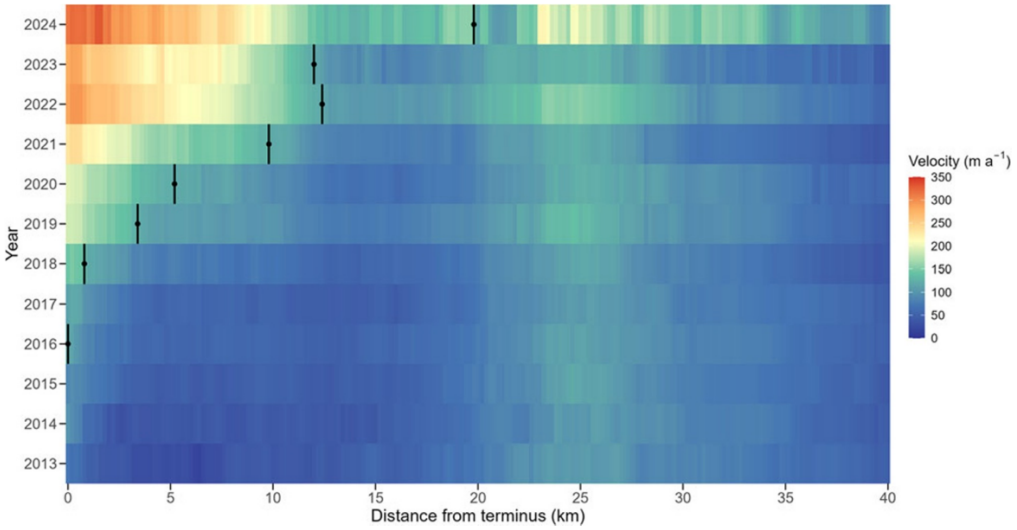


Figure 5-13: Centerline ice velocities of Southeast-2 Glacier from 2013 to 2024 derived from ITS_LIVE v2. Black markers indicate the upstream limit of fast flow >120 m a^{-1} within the glacier trunk (lower ~20 km), illustrating the upglacier propagation of the glacier over time (Lauzon et al. 2026).

The active phase of the SE glacier is proposed to be ~8-9 years, which is on the lower end of active phases in the CAA but is similar to the active phase of pulse-type glaciers. While SE-2's current active phase velocity peaks at 350 m a^{-1}, slower than the study glaciers, SE-2's surge from 1975-1984 exceeded 3000 m a^{-1}. The Southeast glaciers of the Devon Ice Cap were identified as surge-type glaciers but share spatial trends similar to those of pulse-type glaciers, differing primarily in how the surge propagates up the glacier.

Another recently published study of an up-propagating surge-type glacier is the study of Mittie Glacier (Copland et al. 2024). Mittie Glacier is a more typical surge-type glacier within the CAA, with a 15-year active phase, but uniquely had a peak velocity of 4800 m a^{-1} in 1996. The average velocity of the glacier while it was building up to its maximum surge velocity was between 500 m a^{-1} and 1000 m a^{-1} (Figure 5-14). Mittie Glacier's region of velocity variability was observed only in the lowermost 30 km of the glacier; velocity variability occurred only downglacier of a subglacial ridge at 30 km from the terminus. While the variable-velocity region is substantially larger than the study glaciers in this thesis, it is still bounded by subglacial topography. For most of Mittie Glacier's surge, the glacier exhibits velocities similar to those of Dobbin Bay and Parrish Glacier in this study. But Mittie Glacier

experiences the surge for 15 years compared to the active phase of the study glacier, which spans from 4- 6 years, exemplifying the difference in active phases of the two classes.

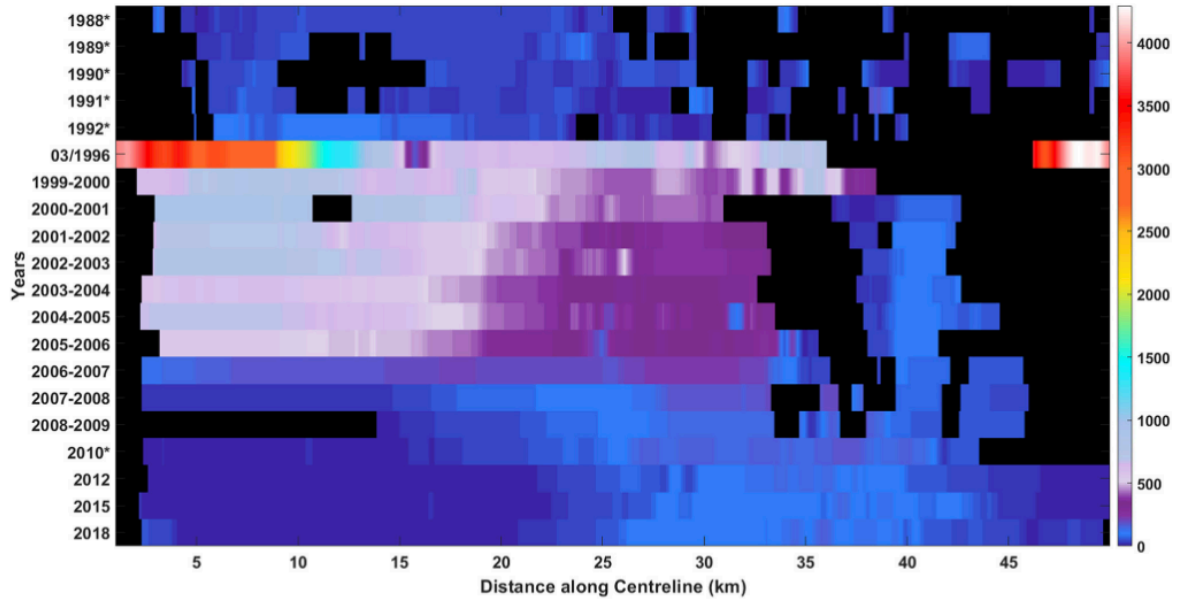


Figure 5-14: Centerline surface velocity (m a^{-1}) of Mittie Glacier from 1988 to 2018 along the centerline of the glacier. Years with an asterisk denote years where velocities were taken from ITS_LIVE; velocities for 1996 were derived from SAR offset tracking, while annual ranges were derived from optical image feature tracking (Copland et al, 2024).

While SE-1, SE-2 and Mittie Glaciers experience similarities in velocity variability, a study from Medrzycka et al, (2019) of Good Friday Glacier shows an extreme case of restrictive topography and its effect on glacier dynamics. Good Friday Glacier previously was a land-terminating glacier, but due to a steady 7.7 km advance of the terminus over 7 decades, the glacier is now marine-terminating. This provides an interesting case study of restrictive bed topography, as the previous push moraine of the glacier is a nunatak, or an exposed piece of bedrock, interacting with ice dynamics. As seen in Figure 5-15, velocities upstream of the nunatak range from 100 m a^{-1} to 200 m a^{-1}, but once past the restrictive topography at 9 km from the terminus, velocities increase. From the 2010s to 2018, as the glacier advanced, peak velocities at the terminus region were around 400 m a^{-1}. These dynamics of the Good Friday Glacier were found to result from stress buildup over the bedrock bump (Medrzycka et al., 2019). While not exactly what is occurring in Dobbin Bay Glacier, Parrish Glacier, and Eugenie

Glacier, Medrzycka et al. (2019) concluded that the reason for variations in the flow of the Good Friday Glacier was due to mechanisms similar to those presented in this study.

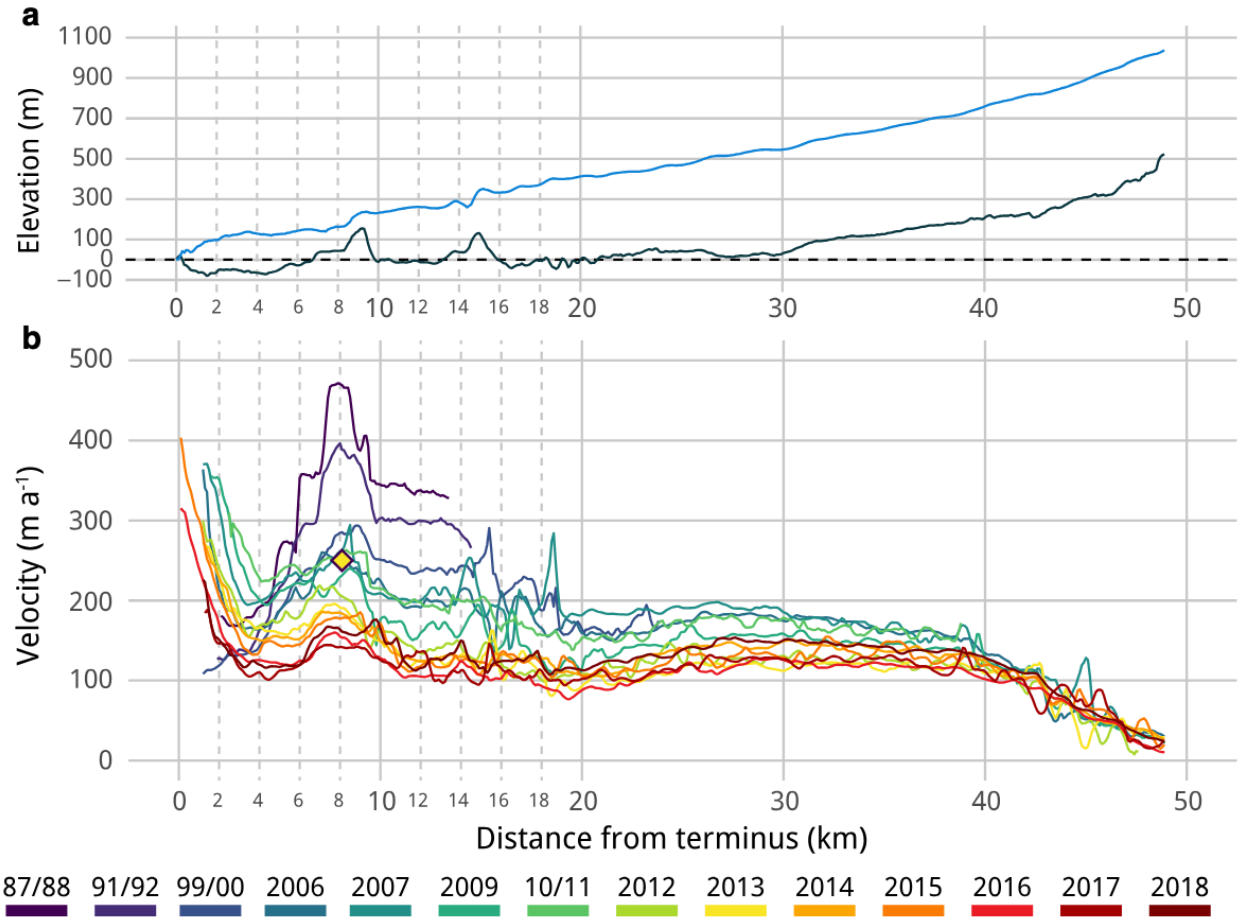


Figure 5-15: a) provides the surface topography (light blue) and basal topography (black) of Good Friday Glacier. B) provides the centerline ice surface velocities from 1987 to 2018. Velocities were derived through SAR speckle tracking. The yellow diamond indicates the velocities recorded at the terminus of Good Friday Glacier in 1959. (Medrzycka et al., 2019)

Similar to Good Friday Bay, the Chapman Glacier was identified as a slow surge glacier in Van Wychen et al., (2025). Notably different, though, is that Chapman Glacier has a dendritic flow, with a main trunk and tributary trunk. This convergence of flows seems to drive the surge within the glacier. Chapman Glacier's current surge began in 2001, as the main trunk of the glacier gradually accelerated from velocities of 75 m a^{-1} to 175 m a^{-1}. But in 2012, the tributary trunk activated, which at first disrupted the accelerating ice, but then contributed to heightened velocities of 225 m a^{-1} along the main trunk. Interestingly, in the context of this thesis, a bedrock bump is present at the section where the main and tributary trunks converge.

While the conclusions of Van Wychen et al. (2025) pointed more to the confluence of flows influencing surge activity, the presence of a bedrock bump may also influence local dynamics.

While the study glaciers of this thesis exhibit many similarities to other surge-type and slow-surge-type glaciers within the CAA, they do not fit into the definition of either category of glacier. The pulse-type glacier's variable velocity is constrained by highly constricted areas; while this occurs within Mittie Glacier and Chapman Glacier, it is either for the entire trunk of the glacier or temporary. The region of variable velocity also is restricted to the lower regions of the glacier, like the Southeast glaciers of Devon Ice Cap. But instead, pulse-type glaciers experience variable velocity across most of the region during most of the active phase, unlike SE-2, which is gradually propagating up the glacier. Pulse-type glaciers also only experience an active phase for a short period of time, around 4 - 6 years, compared to the longer active phases of typical surges, 10 - 15 years, and slow surges 15–100 years.

5.3.3 Pulse-type glacier categorization

As exemplified by the wide range of ways irregular dynamics manifest within the CAA in recent literature, our understanding of surge-type and other glaciers that exhibit irregular dynamics is shifting. Along with many of the conclusions of more recent studies such as Van Wychen et al. (2025), the understanding of surge-type glaciers in the CAA is moving to a wider scope of irregular dynamics. Pulse-type glaciers have been considered as a subclass in the wider context of irregular glacier dynamics (Lovell et al, 2026). But as our current understanding of glaciers in the CAA expands through further case studies, such as Van Wychen et al, (2025), surge-type glaciers are becoming a subcategory of the broader category of irregular dynamics in the CAA. As surge-type glaciers move away from being the broader term, pulse-type glaciers should be defined as a distinct set of activity within the understanding of irregular dynamics. While pulse-type glaciers should exist as their own class, they still need to be differentiated from surge-type glaciers and slow surge-type glaciers.

Table 5-1: Comparison of key dynamic characteristics between surge-type and pulse-type glaciers in the CAA

CAA Surge Type Glacier	**Pulse Type Glacier**	**CAA Slow Surge Type Glacier**
5-25 active phase	4 – 8 year active phase	26 – 100 active phase
Peak velocities of 3000 m a^{-1}	Peak velocities from 500 – 1100 m a^{-1}, which only occur downglacier of the subglacial sill	Peak velocities of ~200 m a^{-1} in slow surge
Active and quiescent phase experience throughout the glacier	Active and quiescent phase dynamics to downglacier of the sub glacier sill	Active and quiescent phase propagate up or downglacier gradually
Terminus expansion of >5 km	Terminus expansion of 2 to 3 km	Terminus expansion of >5 km
Dynamic thinning can occur during quiescence	Dynamic thinning of the downglacier region of the upglacier sill during quiescence	Thinning of trunk through quiescence
Thermal switch controlling irregular dynamics	Basal topography and hydraulic switch controlling irregular dynamics	Thermal switch controlling
~54 surge type glaciers	8 pulse type glaciers.	~6-10 Slow surge glaciers

5.3.3.1 Pulse-Type Glacier's Uniqueness

Pulse-type glaciers not only have unique regions of velocity variability but may also have different mechanics than surge-type glaciers in the CAA. Pulse-type glaciers exhibit irregular dynamics that occur only downglacier of high-friction topography, which, in the pulse glaciers of this study, is typically found 6-12 km from the terminus. For other pulse-type glaciers, Ekblaw and Cadogan, the subglacial sill is present at distances of 6.5 km and 7.5 km from the terminus, respectively (Dalton et al, 2022). Between the subglacial sill and terminus, velocities are nearly stagnant at 20 m a^{-1} during quiescence, while velocities upglacier of the sill flow at

~100 m a^{-1}. During the active phase, velocities increase to rates of 200 – 1100 m a^{-1}, a 10 to 55 times increase in velocity. All while surface velocities upglacier of the sill remain at ~100 m a^{-1}. The pulse phase lasts for at least 4 years on the short end, compared to the potential active phase of CAA surge glaciers, which spans from 5 – 70 years. Finally, pulse-type glaciers also exhibit different mechanics from CAA surge-type glaciers, with the subglacial sills of pulse-type glaciers as the controlling element, rather than basal thermal conditions.

5.3.3.2 Pulse-Type as a Subcategory of Irregular Dynamics Within the CAA

Based on recent literature and studies on unstable glaciers within the CAA, surge-type glaciers no longer serve as a blanket term for all unstable glaciers (Van Wychen et al., 2025, Lovell 2026). The CAA experiences a wide range of irregular dynamics, from constant acceleration to surge, pulse, and slow surge; each type of glacier has its own defined activity. But as exemplified by the Eugenie Glacier, not all glaciers will align perfectly with each definition. Pulse type glaciers share similar active phase velocities to surge type glaciers of ≥ 1000 m a^{-1}, such as Mittie and the Southeast glaciers of Devon Ice Cap. Pulse-type glaciers also share a similar quiescent phase of ≤ 25 m a^{-1}. But what makes pulse-type glaciers unique is that these velocities are only experienced downglacier of constrictive topography, while the upglacier portion of the trunk flows in line with regional glaciers. While only 8 pulse-type glaciers have been identified, the dynamics experienced on these glaciers are unique enough to be classified as their own distinct category within the broader spectrum of irregular dynamics within the CAA.

Chapter 6 - Conclusion

6.1 Summary and Primary Findings

Polar glaciers are losing mass at an accelerating rate due to climate change, which will continue to contribute to global sea level rise. To understand the global impact of glacier mass loss, models need to properly account for unstable glaciers. While accounting for only 1% of global glaciers, unstable glaciers contribute substantial mass to the ocean at irregular intervals. The driving forces and dynamics of these glaciers are not fully understood, as many types of unstable glacier activity have still yet to be fully defined. The primary goal of this thesis was to deepen understanding of pulse-type glaciers, an understudied category of unstable glaciers. Expanding on the work of Van Wychen et al. (2016), two identified pulse-type glaciers, Dobbin Bay Glacier and Parrish Glacier, were examined to better understand the dynamics which occur within pulse-type glaciers. Given the similar dynamics, the activity of Eugenie Glacier, located between Dobbin Bay Glacier and Parrish Glacier, was examined to quantify pulse-type dynamics. Pulse-type activity was quantified through a combination of optical and SAR imagery and DEM products to create a record of surface ice velocity, elevation change, and terminus evolution of three pulse-type glaciers. To achieve a better understanding of pulse-type glaciers, the objectives of this thesis were identified

1) Build a record of mass build-up, ice velocity and terminus position change using satellite imagery and data for Dobbin Bay Glacier, Eugenie Glacier and Parrish Glacier from 2000 to 2022.
2) Refine and define regions of pulse-type activity on the selected glaciers where pulse-type activities occur and compare these locations across the glacier basins.
3) Distinguish pulse-type signals from the three different basins to gauge an upper and lower bound of pulse-type dynamics within the region.

Research objective 1 was to build a record of mass buildup, ice velocity and terminus position change using satellite data for the identified study glaciers from 2000 to 2022. Mass build-up was quantified through comparing successive DEMs collected from ArcticDEM over the study glaciers. While the available data was only captured from 2010 to 2023, the observed elevation change captured informed dynamics throughout the quiescent period of the study glaciers. A record of ice velocity was compiled using both SAR and optical imagery tracking, spanning from 2000 to 2022. ITS_LIVE surface ice velocity data were obtained from NASA and compared with SAR feature-tracking data from 2021 to 2022 to ensure that velocities were consistent. Finally, terminus positions for all study glaciers were collected from 2000–2022, with sparse data from 1959–2000 included to further contextualize activity on the study glaciers. Terminus position evolution was derived from various optical imagery products including data from the Landsat series satellites, ASTER, SPOT, and aerial photographs. In collecting all the datasets, a record of activity was successfully built from 2000 – 2022, providing insight into the three study glaciers.

In completing objective 1, regions of the glacier where pulse-type activity occurs was defined on Dobbin Bay Glacier, Parrish Glacier and Eugenie Glacier. This was done primarily in combining the elevation change, surface ice velocity and bed topography. Pulse initiation regions were defined as regions where surface elevation rises and velocities slow in a quiescent phase. Then, in an active phase, that same region must experience an acceleration of surface ice velocities. These regions also must contain a piece of constrictive topography, either subglacial sill or a significant change in flow direction. The region of the glacier between the pulse initiation region and the terminus was then defined as the pulse region. On Dobbin Bay Glacier the pulse initiation region is located from 6 to 10 km from the terminus. On Parrish Glacier, the pulse initiation region is present from 7.5 to 12 km from the terminus. On Eugenie

Glacier, the pulse initiation region is present from 8 km to 13 km from the terminus. Between the three glaciers, Dobbin Bay Glacier and Parrish Glacier act the most similar to each other, with both glaciers reaching velocities of 1000 m a^{-1} in the pulse region, while also experiencing similar pulse phase lengths of 4-6 years. Eugenie Glacier was the most distinctive of the three, with slower ice velocities throughout the pulse region and a longer pulse phase.

Through further comparison of the study glaciers to each other, constrictive topography was identified as a relevant feature responsible for irregular dynamics. The highest rates of mass buildup occurred in locations where the topography of the glacier, either through subglacial bumps or sharp valley turns, potentially causes areas of high friction. At these same locations, especially in Dobbin Bay Glacier and Parrish Glacier, is where surface ice velocities begin to deviate. Variations in ice velocity propagate only slightly upglacier from constrictive features. In both the active and quiescent phases, constrictive topography affected the flow of ice through the trunk. Additionally, by comparing terminus evolution with surface ice velocity, it was determined that Dobbin Bay Glacier experienced a pulse from 2004 to 2008, Parrish Glacier from 2004 to 2010, and Eugenie Glacier from before 2000 to 2008. During a pulse event, velocities ranged from 200 m a^{-1} to 1100 m a^{-1} within the pulse region. During the same pulse events, velocities upglacier of the pulse initiation region remained between 75 m a^{-1} and 125 m a^{-1}. During the quiescent phase, velocities in the pulse region slowed to velocities of <30 m a^{-1}, while the upglacier regions remained at velocities from 75 m a^{-1} to 125 m a^{-1}. While the extent of terminus retreat during quiescence was not captured, terminus advance during a pulse event typically ranged from 2 to 3 km over a 4-6 year active phase.

Finally, this study also refined the previous pulse-type glacier definition presented in Van Wychen et al. (2016) to: *pulse-type glaciers experience irregular dynamics downglacier of high-friction topography. Resulting in two regions of unique motion across the glacier during periods of quiescent / slowed flow, and active/fast flow.* Additionally, under this definition,

pulse-type glaciers were identified as a distinct category within the broader, more modern understanding of irregular dynamics within the CAA.

6.2 Limitations

Many limitations exist in this study, primarily related to data availability, which affects both data quality and the study's timeframe. This is especially pertinent for optical imagery used to determine terminus positions. Due to data not being collected over the study area or not being available, large gaps in terminus positions exist from 1959 to 2000. As first hypothesized by Van Wychen (2016), pulse-type glaciers complete a pulse cycle on a shorter timeframe than surge-type glaciers. But due to the lack of pre-2000s data, it is possible that a short pulse event occurred within temporal gaps in the data. This is especially relevant to Eugenie Glacier velocity data, and elevation data for the study area were not collected before 2000, leaving the starting year of pulse activity on Eugenie Glacier unknown. Data availability also affected the results for elevation change. While the ArcticDEM data availability began in 2010, for many years, it had only one viable DEM annually. Temporal data sparsity specifically affecting the interannual elevation change products, with cloud coverage, satellite flight path, weather and system error impacting the interannual elevation change product.

Another limitation is the data that was not included within this study, being mass balance measurements and climate data. Mass balance data would have provided more accurate measurements of how much mass moved through and was trapped within the systems on yearly scales. While important for understanding changes within the studied glaciers, mass balance data were excluded because velocity and elevation change data provided similar insights at a higher spatial resolution. By combining data, pulse periods can be defined and irregular dynamics identified on the glacier, something that understanding the mass balance cannot do.

Climate data would have offered further information on how melt occurs on the study glaciers. Climate data could also be used to further demonstrate that the glaciers' irregular

dynamics result from the surrounding topography. This data could have been obtained from regional weather stations or climate analysis data, such as ERA-5. Regional weather stations were excluded because they were not close enough to individual glaciers and regions within them. Reanalysis climate data was not chosen due to the system's low spatial resolution. Understanding annual climate may have provided further insight into pulse onset and termination, but compared with other studies in the region, climate data were not found to directly affect surge dynamics. Comparing multiple glaciers' dynamics also allows regional climate data to be better characterized, as the glaciers had similar rates of motion and thinning and were all nearby to each other.

Finally, surface features of the study glaciers were not analysed to determine whether these glaciers exhibit responses to irregular dynamics, as in Copland et al. (2003). Identifying surface features, such as looped moraines and crevassing, helps determine whether glaciers exhibit irregular dynamics, such as surging. While this is the first focused study on the glaciers, Parrish Glacier and Dobbin Bay Glacier have been included in regional assessments of irregular dynamics in the CAA. Copland et al. (2003) provided evidence that these glaciers exhibited these features and suggested that they were potentially surge-type. Surface surge features would also only confirm whether these glaciers exhibit irregular dynamics and would not provide a temporal or spatial understanding more accurate than the already included methods.

6.3 Next Steps

Future studies should further examine pulse-type glaciers and investigate the effects of subglacial sills on glacial systems. First, the remaining pulse-type glaciers identified in Van Wychen et al. (2016) that have not been systematically studied need to be further investigated. Glaciers requiring research are Antoinette Glacier, Tuborg Glacier, Cañon Glacier and Sydkap Glacier. With the remaining glaciers, the definition presented in this study can be further refined or validated. Furthermore, an analysis of other glaciers with subglacial sills or other

locations which present constrictive topography should be investigated and noted for potential cases of future pulse-type activity. Additionally, identified pulse-type glaciers should continue to be monitored for future pulse events. Further monitoring will allow for identification that pulse events are cyclical and will allow for a definition of the quiescent phase of pulse-type glaciers to be made. Future in situ studies should also be conducted on identified pulse-type glaciers to further understand the pulse initiation region. This will allow the mechanics presented in this study to be understood, enabling the formation of an understanding of the driving forces of pulse initiation. Finally, the study of individual unstable glaciers should be continued to better understand the cause of irregular dynamics within the CAA.

References

Benn, D. I., & Evans, D. J. A. (2013). *Glaciers and Glaciation, 2nd edition* (2nd ed.). Routledge. https://doi.org/10.4324/9780203785010

Benn, D. I., Fowler, A. C., Hewitt, I., & Sevestre, H. (2019). A general theory of glacier surges. *Journal of Glaciology*, *65*(253), 701–716. https://doi.org/10.1017/jog.2019.62

Benn, D. I., Hulton, N. R. J., & Mottram, R. H. (2007). 'Calving laws', 'sliding laws' and the stability of tidewater glaciers. *Annals of Glaciology*, *46*, 123–130. https://doi.org/10.3189/172756407782871161

Boulton, G. S. (1996). Theory of glacial erosion, transport and deposition as a consequence of subglacial sediment deformation. *Journal of Glaciology*, *42*(140), 43–62. https://doi.org/10.3189/S0022143000030525

Clarke, G. K. C., Collins, S. G., & Thompson, D. E. (1984). Flow, thermal structure, and subglacial conditions of a surge-type glacier. *Canadian Journal of Earth Sciences*, *21*(2), 232–240. https://doi.org/10.1139/e84-024

Cogley, J. G., & Adams, W. P. (1998). Mass balance of glaciers other than the ice sheets. *Journal of Glaciology*, *44*(147), 315–325. https://doi.org/10.3189/S0022143000002641

Cook, A. J., Copland, L., Noël, B. P. Y., Stokes, C. R., Bentley, M. J., Sharp, M. J., Bingham, R. G., & van den Broeke, M. R. (2019). Atmospheric forcing of rapid marine-terminating glacier retreat in the Canadian Arctic Archipelago. *Science Advances*, *5*(3), eaau8507. https://doi.org/10.1126/sciadv.aau8507

Copland, L., Sharp, M. J., & Dowdeswell, J. A. (2003). The distribution and flow characteristics of surge-type glaciers in the Canadian High Arctic. *Annals of Glaciology*, *36*, 73–81. https://doi.org/10.3189/172756403781816301

Copland, L., Hallé, D., Wychen, W. V., Lauzon, B., Dowdeswell, J. A., & Davis, J. (2024). Characteristics of the 15-year surge of Mittie Glacier, SE Ellesmere Island, Canadian Arctic. *Annals of Glaciology*, *65*, e30. https://doi.org/10.1017/aog.2024.31

Cuffey, K. M., & Paterson, W. S. B. (2010). *The Physics of Glaciers*. Academic Press.

Danielson, B., & Sharp, M. (2013). Development and application of a time-lapse photograph analysis method to investigate the link between tidewater glacier flow variations and supraglacial lake drainage events. *Journal of Glaciology*, *59*(214), 287–302. https://doi.org/10.3189/2013JoG12J108

Davies, B. (2020, June 22). Glacier accumulation and ablation. *AntarcticGlaciers.Org*. https://www.antarcticglaciers.org/glacier-processes/mass-balance/glacier-accumulation-and-ablation/

Dunse, T., Schellenberger, T., Hagen, J. O., Kääb, A., Schuler, T. V., & Reijmer, C. H. (2015). Glacier-surge mechanisms promoted by a hydro-thermodynamic feedback to summer melt. *The Cryosphere*, *9*(1), 197–215. https://doi.org/10.5194/tc-9-197-2015

Duval, P., Montagnat, M., Grennerat, F., Weiss, J., Meyssonnier, J., & Philip, A. (2010). Creep and plasticity of glacier ice: A material science perspective. *Journal of Glaciology*, *56*(200), 1059–1068. https://doi.org/10.3189/002214311796406185

Eisen, O., Harrison, W. D., & Raymond, C. F. (2001). The surges of variegated glacier, Alaska, U.S.A., and their connection to climate and mass balance. *Journal of Glaciology*, *47*(158), Article 158. https://doi.org/10.3189/172756501781832179

Fowler, A. C. (2010). Weertman, Lliboutry and the development of sliding theory. *Journal of Glaciology*, *56*(200), 965–972. https://doi.org/10.3189/002214311796406112

Gardner, A. S., Greene, C. A., Kennedy, J. H., Fahnestock, M. A., Liukis, M., López, L. A., Lei, Y., Scambos, T. A., & Dehecq, A. (2025). ITS_LIVE global glacier velocity data in near-real time. *The Cryosphere*, *19*(9), 3517–3533. https://doi.org/10.5194/tc-19-3517-2025

Hugonnet, R., McNabb, R., Berthier, E., Menounos, B., Nuth, C., Girod, L., Farinotti, D., Huss, M., Dussaillant, I., Brun, F., & Kääb, A. (2021). Accelerated global glacier mass loss in the early twenty-first century. *Nature*, *592*(7856), Article 7856. https://doi.org/10.1038/s41586-021-03436-z

Huss, M. (2013). Density assumptions for converting geodetic glacier volume change to mass change. *The Cryosphere*, *7*(3), 877–887. https://doi.org/10.5194/tc-7-877-2013

Intergovernmental Panel on Climate Change (IPCC). (2022). *The Ocean and Cryosphere in a Changing Climate: Special Report of the Intergovernmental Panel on Climate Change* (1st ed.). Cambridge University Press. https://doi.org/10.1017/9781009157964

Intergovernmental Panel On Climate Change (IPCC). (2022a). *The Ocean and Cryosphere in a Changing Climate: Special Report of the Intergovernmental Panel on Climate Change* (1st ed.). Cambridge University Press. https://doi.org/10.1017/9781009157964

Intergovernmental Panel On Climate Change (IPCC). (2022b). *The Ocean and Cryosphere in a Changing Climate: Special Report of the Intergovernmental Panel on Climate Change* (1st ed.). Cambridge University Press. https://doi.org/10.1017/9781009157964

ITS_LIVE a NASA MEaSURES Program | NASA JPL. (n.d.). Retrieved March 10, 2025, from https://its-live.jpl.nasa.gov/

Jennings, S. J. A., & Hambrey, M. J. (2021). Structures and Deformation in Glaciers and Ice Sheets. *Reviews of Geophysics*, *59*(3), e2021RG000743. https://doi.org/10.1029/2021RG000743

Jezek, K., Wu, X., Paden, J., & Leuschen, C. (2013). Radar mapping of Isunnguata Sermia, Greenland. *Journal of Glaciology*, *59*(218), 1135–1146. https://doi.org/10.3189/2013JoG12J248

Jiskoot, H., Boyle, P., & Murray, T. (1998). The incidence of glacier surging in Svalbard: Evidence from multivariate statistics. *Computers & Geosciences*, *24*(4), 387–399. https://doi.org/10.1016/S0098-3004(98)00033-8

Jiskoot, H., Murray, T., & Boyle, P. (2000). Controls on the distribution of surge-type glaciers in Svalbard. *Journal of Glaciology*, *46*(154), 412–422. https://doi.org/10.3189/172756500781833115

Jiskoot, H., Fox, T. A., & Van Wychen, W. (2017). Flow and structure in a dendritic glacier with bedrock steps. *Journal of Glaciology*, *63*(241), 912–928. https://doi.org/10.1017/jog.2017.58

Kamb, B. (1987). Glacier surge mechanism based on linked cavity configuration of the basal water conduit system. *Journal of Geophysical Research: Solid Earth*, *92*(B9), 9083–9100. https://doi.org/10.1029/JB092iB09p09083

Kochtitzky, W., Jiskoot, H., Copland, L., Enderlin, E., Mcnabb, R., Kreutz, K., & Main, B. (2019). Terminus advance, kinematics and mass redistribution during eight surges of Donjek Glacier, St. Elias Range, Canada, 1935 to 2016. *Journal of Glaciology*, *65*(252), 565–579. https://doi.org/10.1017/jog.2019.34

Landsat 8—NASA Science. (2023, June 15). https://science.nasa.gov/mission/landsat-8/

Lauzon, B., Copland, L., Van Wychen, W., Kochtitzky, W., & McNabb, R. (2023). Evolution of the dynamics of Airdrop Glacier, western Axel Heiberg Island, over a seven-decade-long advance. *Arctic Science*. https://doi.org/10.1139/as-2022-0045

Lauzon, B., Copland, L., & Van Wychen, W. (2026). Recurrent surge dynamics and ongoing acceleration at Devon Ice Cap's Southeast basin, Canadian Arctic. *Journal of Glaciology*, *72*, e35. https://doi.org/10.1017/jog.2026.10149

Li, B., Zhang, X., Tang, H., & Tsubaki, R. (2018). Influence of deflection angles on flow behaviours in openchannel bends. *Journal of Mountain Science*, *15*(10), 2292–2306. https://doi.org/10.1007/s11629-018-4848-y

Lovell, H., Benn, D. I., Jiskoot, H., Stokes, C. R., Flowers, G. E., Guillet, G., Mannerfelt, E. S., Falaschi, D., Kääb, A., King, O., Benediktsson, Í. Ö., Bhambri, R., Lv, M., Muhammad, S., & Luckman, A. (2026). Glacier surging and surge-related hazards in a changing climate. *Nature Reviews Earth & Environment*, 1–19. https://doi.org/10.1038/s43017-025-00757-9

Medrzycka, D., Copland, L., Van Wychen, W., & Burgess, D. (2019). Seven decades of uninterrupted advance of Good Friday Glacier, Axel Heiberg Island, Arctic Canada. *Journal of Glaciology*, *65*(251), 440–452. https://doi.org/10.1017/jog.2019.21

Meier, W. N. & Stewart, J. S. (2023). Arctic and Antarctic Regional Masks for Sea Ice and Related Data Products. (NSIDC-0780, Version 1). [Boulder, Colorado USA. NASA National Snow and Ice Data Center Distributed Active Archive Center. https://doi.org/10.5067/CYW3O8ZUNIWC.

Mortimer, C. A., Sharp, M., & Van Wychen, W. (2018). Influence of recent warming and ice dynamics on glacier surface elevations in the Canadian High Arctic, 1995–2014. *Journal of Glaciology*, *64*(245), 450–464. https://doi.org/10.1017/jog.2018.37

Noël, B., van de Berg, W. J., Lhermitte, S., Wouters, B., Schaffer, N., & van den Broeke, M. R. (2018a). Six Decades of Glacial Mass Loss in the Canadian Arctic Archipelago. *Journal of*

Geophysical Research: Earth Surface, *123*(6), 1430–1449. https://doi.org/10.1029/2017JF004304

Noël, B., van de Berg, W. J., Lhermitte, S., Wouters, B., Schaffer, N., & van den Broeke, M. R. (2018b). Six Decades of Glacial Mass Loss in the Canadian Arctic Archipelago. *Journal of Geophysical Research: Earth Surface*, *123*(6), 1430–1449. https://doi.org/10.1029/2017JF004304

Nuth, C., & Kääb, A. (2011). Co-registration and bias corrections of satellite elevation data sets for quantifying glacier thickness change. *The Cryosphere*, *5*(1), 271–290. https://doi.org/10.5194/tc-5-271-2011

Pfeffer, W. T., Arendt, A. A., Bliss, A., Bolch, T., Cogley, J. G., Gardner, A. S., Hagen, J.-O., Hock, R., Kaser, G., Kienholz, C., Miles, E. S., Moholdt, G., Mölg, N., Paul, F., Radić, V., Rastner, P., Raup, B. H., Rich, J., Sharp, M. J., & Consortium, T. R. (2014). The Randolph Glacier Inventory: A globally complete inventory of glaciers. *Journal of Glaciology*, *60*(221), 537–552. https://doi.org/10.3189/2014JoG13J176

Prokopiak, C., Leuschen, C., Rodriguez-Morales, F., Ledford, J., Blake, W., Hoch, A., & Barbour, H. (2011). Multi-node Network Based Control and Data Acquisition System for a VHF Radar Depth Sounder. *2011 IEEE 35th Annual Computer Software and Applications Conference*, 182–183. https://doi.org/10.1109/COMPSAC.2011.124

Radar Guide · Wiki · openpolarradar / opr · GitLab. (2025, August 11). GitLab. https://gitlab.com/openpolarradar/opr/-/wikis/Radar-Guide

Rantanen, M., Karpechko, A. Y., Lipponen, A., Nordling, K., Hyvärinen, O., Ruosteenoja, K., Vihma, T., & Laaksonen, A. (2022). The Arctic has warmed nearly four times faster than the globe since 1979. *Communications Earth & Environment*, *3*(1), 1–10. https://doi.org/10.1038/s43247-022-00498-3

Raymond, C. F. (1987). How do glaciers surge? A review. *Journal of Geophysical Research: Solid Earth*, *92*(B9), 9121–9134. https://doi.org/10.1029/JB092iB09p09121

RGI Consortium. (2023). *Randolph Glacier Inventory—A Dataset of Global Glacier Outlines, Version 7* [Dataset]. NASA National Snow and Ice Data Center Distributed Active Archive Center. https://doi.org/10.5067/F6JMOVY5NAVZ

Schellenberger, T., Van Wychen, W., Copland, L., Kääb, A., & Gray, L. (2016). An Inter-Comparison of Techniques for Determining Velocities of Maritime Arctic Glaciers, Svalbard, Using Radarsat-2 Wide Fine Mode Data. *Remote Sensing*, *8*(9), Article 9. https://doi.org/10.3390/rs8090785

Schoof, C. (2010). Ice-sheet acceleration driven by melt supply variability. *Nature*, *468*(7325), 803–806. https://doi.org/10.1038/nature09618

Sevestre, H., & Benn, D. I. (2015). Climatic and geometric controls on the global distribution of surge-type glaciers: Implications for a unifying model of surging. *Journal of Glaciology*, *61*(228), 646–662. https://doi.org/10.3189/2015JoG14J136

Sevestre, H., Benn, D. I., Luckman, A., Nuth, C., Kohler, J., Lindbäck, K., & Pettersson, R. (2018). Tidewater Glacier Surges Initiated at the Terminus. *Journal of Geophysical Research: Earth Surface*, *123*(5), 1035–1051. https://doi.org/10.1029/2017JF004358

Sharp, M., Burgess, D. O., Cawkwell, F., Copland, L., Davis, J. A., Dowdeswell, E. K., Dowdeswell, J. A., Gardner, A. S., Mair, D., Wang, L., Williamson, S. N., Wolken, G. J., & Wyatt, F. (2014). Remote sensing of recent glacier changes in the Canadian Arctic. In J. S. Kargel, G. J. Leonard, M. P. Bishop, A. Kääb, & B. H. Raup (Eds.), *Global Land Ice Measurements from Space* (pp. 205–228). Springer. https://doi.org/10.1007/978-3-540-79818-7_9

Short, N. H., & Gray, A. L. (2005). Glacier dynamics in the Canadian High Arctic from RADARSAT-1 speckle tracking. *Canadian Journal of Remote Sensing*, *31*(3), 225–239. https://doi.org/10.5589/m05-010

Tedesco, M. (2015). *Remote Sensing of the Cryosphere*. John Wiley & Sons, Incorporated. http://ebookcentral.proquest.com/lib/waterloo/detail.action?docID=1866576

Thoman, R. L., Moon, T. A., & Druckenmiller, M. L. (2023). *NOAA Arctic Report Card 2023: Executive Summary*. https://doi.org/10.25923/5VFA-K694

Turrin, J. B., & Forster, R. R. (2014). *A conceptual model of cyclical glacier flow in overdeepenings*. https://doi.org/10.5194/tcd-8-4463-2014

Vallot, D., Pettersson, R., Luckman, A., Benn, D. I., Zwinger, T., Pelt, W. J. J. V., Kohler, J., Schäfer, M., Claremar, B., & Hulton, N. R. J. (2017). Basal dynamics of Kronebreen, a fast-flowing tidewater glacier in Svalbard: Non-local spatio-temporal response to water input. *Journal of Glaciology*, *63*(242), 1012–1024. https://doi.org/10.1017/jog.2017.69

Van Wychen, W., Copland, L., & Burgess, D. (2020). Ice Masses of the Eastern Canadian Arctic Archipelago. In O. Slaymaker & N. Catto (Eds.), *Landscapes and Landforms of Eastern Canada* (pp. 297–314). Springer International Publishing. https://doi.org/10.1007/978-3-030-35137-3_13

Van Wychen, W., Davis, J., Burgess, D. O., Copland, L., Gray, L., Sharp, M., & Mortimer, C. (2016). Characterizing interannual variability of glacier dynamics and dynamic discharge (1999-2015) for the ice masses of Ellesmere and Axel Heiberg Islands, Nunavut, Canada: GLACIER DYNAMICS OF THE CANADIAN ARCTIC. *Journal of Geophysical Research: Earth Surface*, *121*(1), 39–63. https://doi.org/10.1002/2015JF003708

Van Wychen, W. V., Burgess, D., Kochtitzky, W., Nikolic, N., Copland, L., & Gray, L. (2020). *RADARSAT-2 Derived Glacier Velocities and Dynamic Discharge Estimates for the Canadian High Arctic: 2015–2020*.

Van Wychen, W., Hallé, D. A. M., Copland, L., & Gray, L. (2022). Anomalous surface elevation, velocity, and area changes of Split Lake Glacier, western Prince of Wales Icefield, Canadian High Arctic. *Arctic Science*, *8*(4), 1288–1304. https://doi.org/10.1139/as-2021-0039

Van Wychen, W., Jiskoot, H., Shannon, K., & Gorwill, C. (2025). The long multiphase trunk–tributary surge history of the high-Arctic Chapman Glacier, 1959–2023. *Arctic, Antarctic, and Alpine Research*, *57*(1), 2441541. https://doi.org/10.1080/15230430.2024.2441541

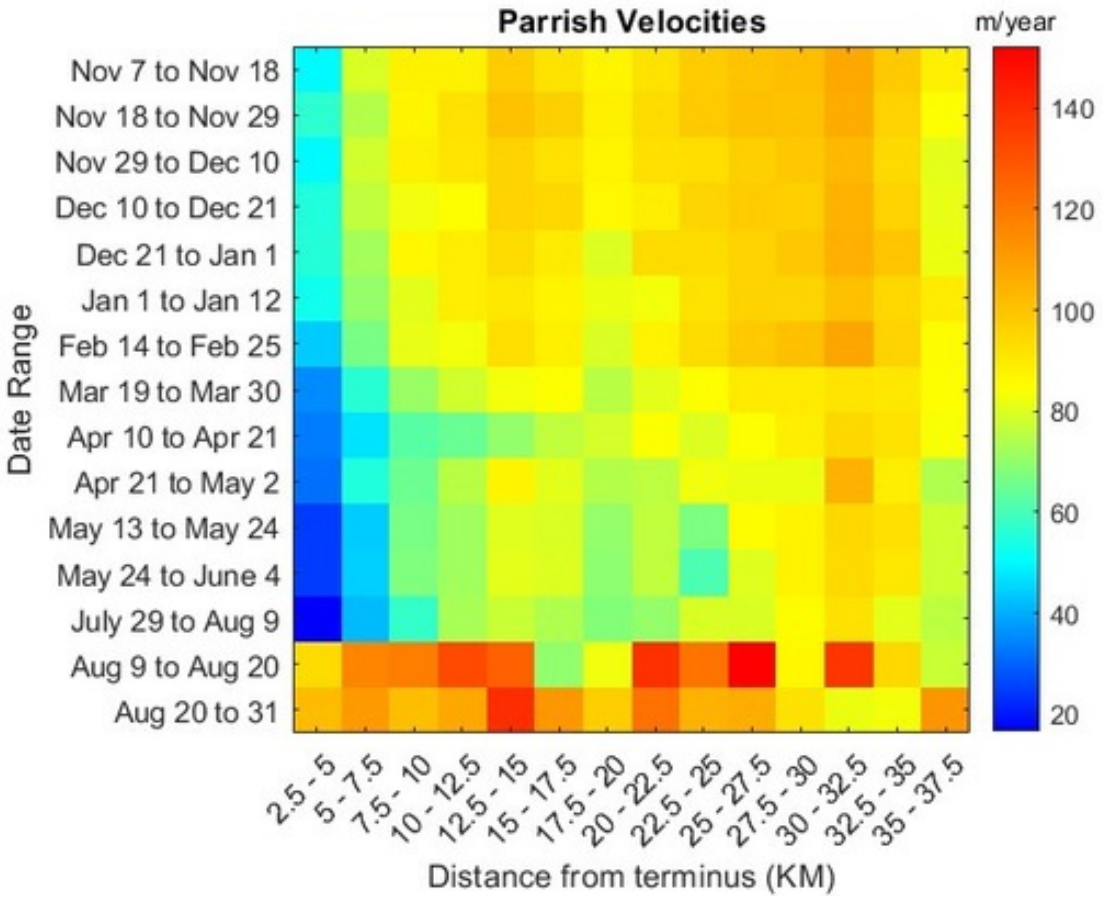
Woodhouse, I. H. (2006). *Introduction to microwave remote sensing*. Taylor&Francis.

Wouters, B., Gardner, A. S., & Moholdt, G. (2019). Global Glacier Mass Loss During the GRACE Satellite Mission (2002-2016). *Frontiers in Earth Science*, *7*. https://doi.org/10.3389/feart.2019.00096

Appendices

A – 1: SAR offset tracking of Parrish Glacier:

Figure A-1 presents surface ice velocities through the end of 2021 to the summer of 2022 over Parrish Glacier. These velocities were obtained via SAR offset tracking, as described in section 3.2.2. When comparing preliminary surface ice velocity results with annual ITS_LIVE surface ice velocity products, the two were in line. Within the terminus region, velocities decrease from 50 m a^{-1} at the terminus to 20 m a^{-1} by August 9th. Upglacier of 7.5-10 km from the terminus surface ice velocities exceed 80 m a^{-1}, reaching maximum speeds of 110 m a^{-1}. The results from August 9th to August 31 are interlaced with error due to the presence of water on the glacier's surface and are therefore untrustworthy.

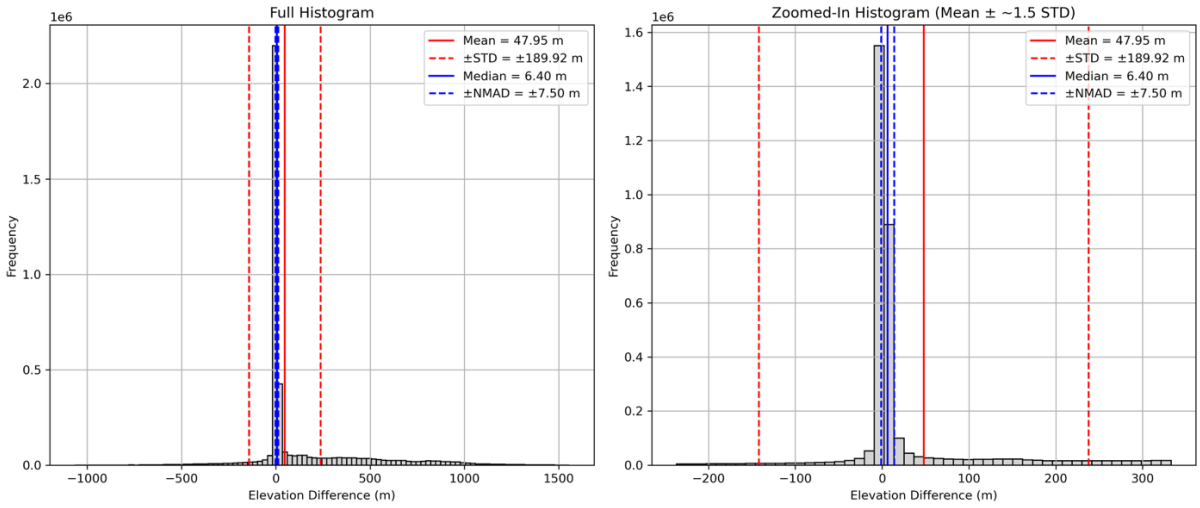


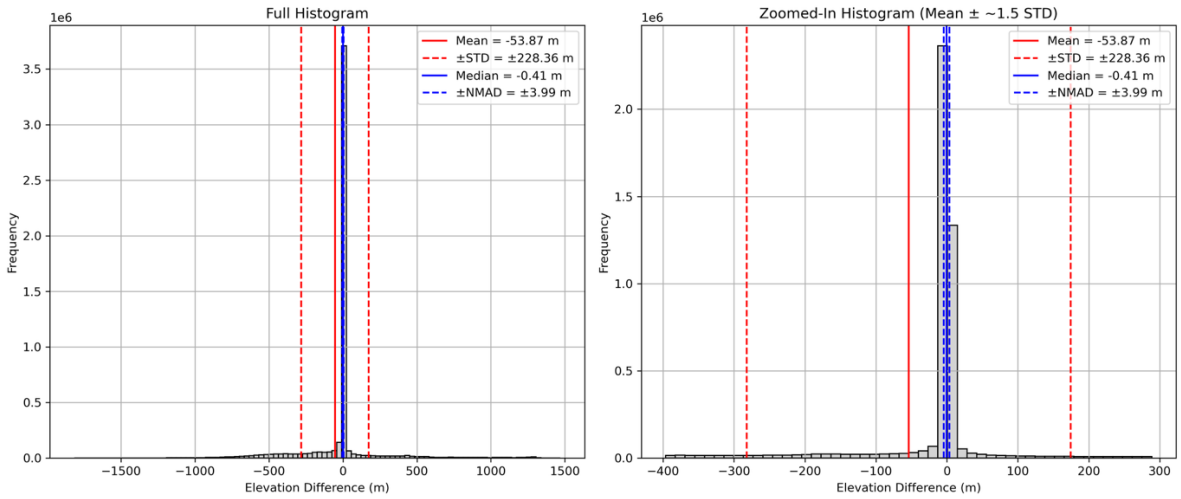
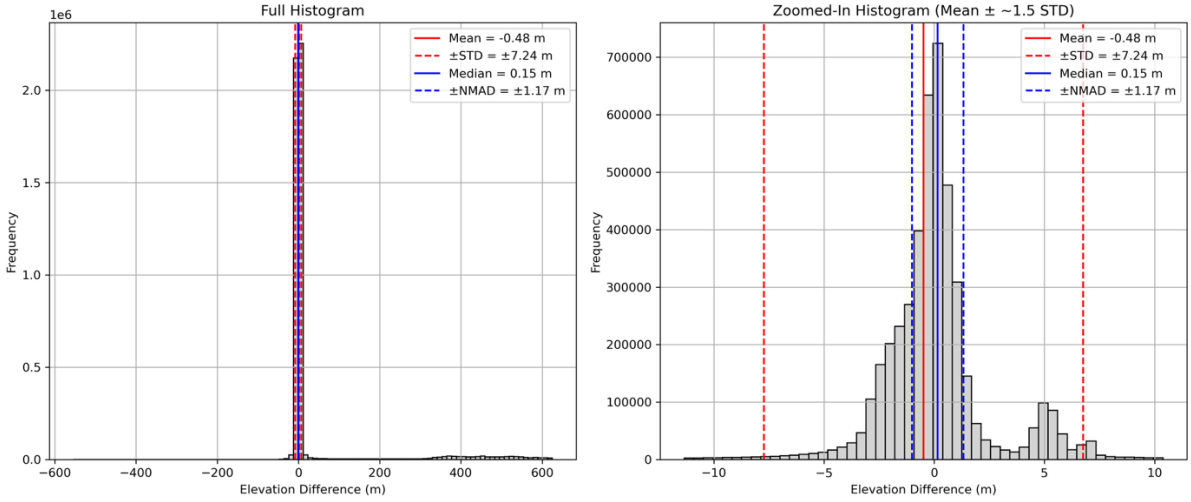
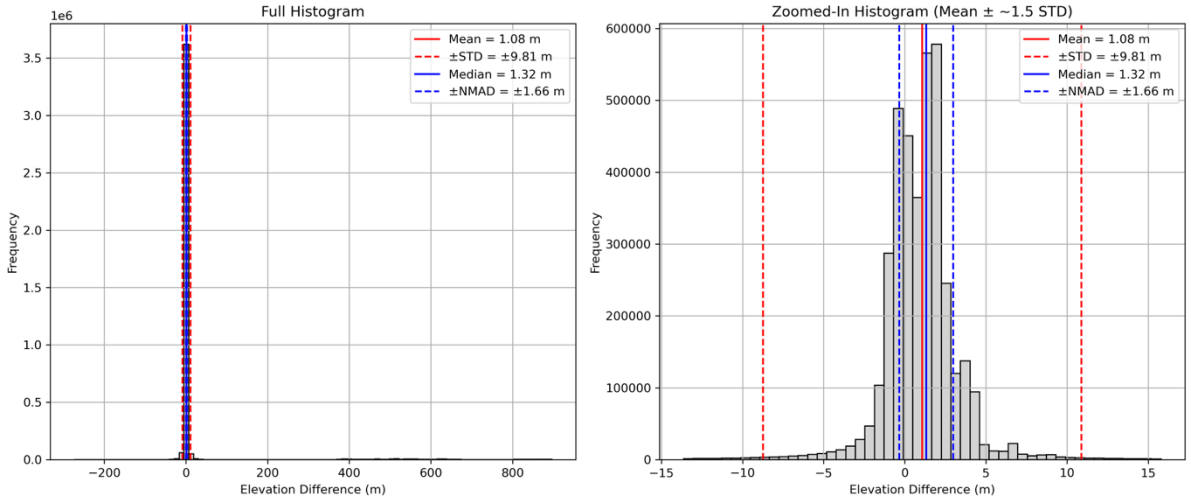
Supplementary figure - 1: Velocity heatmap of Parrish Glacier from November 7, 2021, to August 2022, produced using SAR offset tracking.

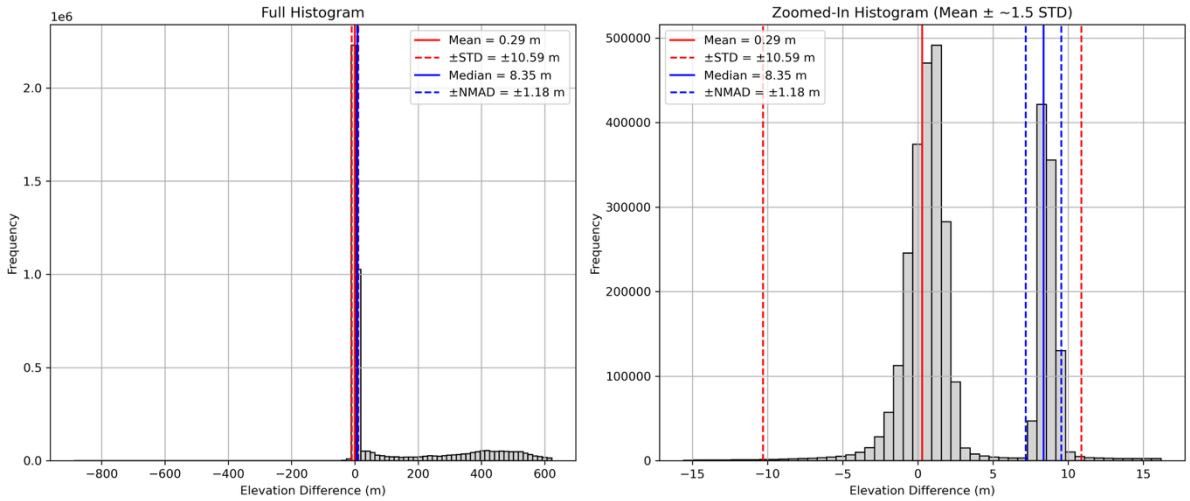
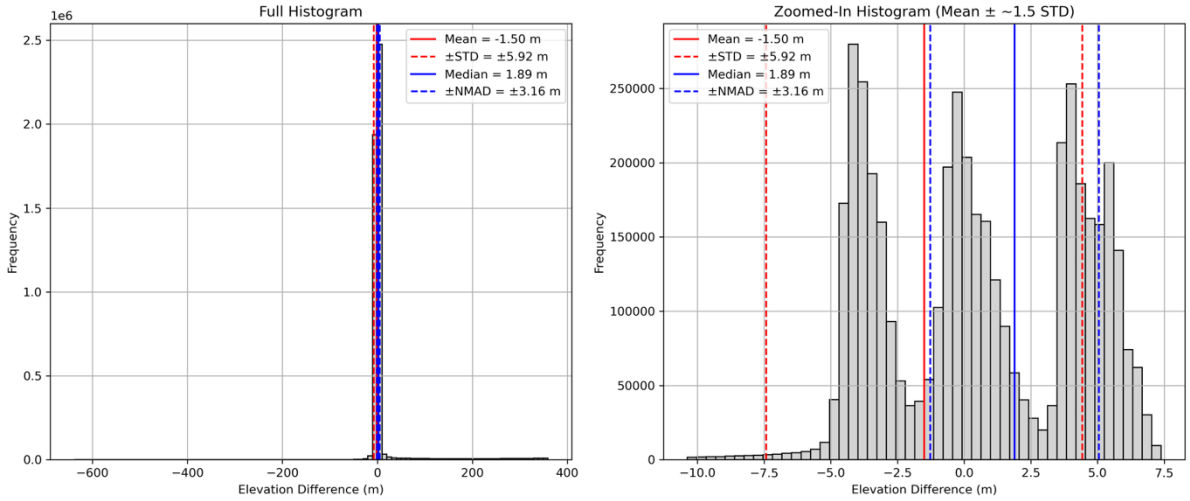
A – 2: DEM UNCERTAINITY

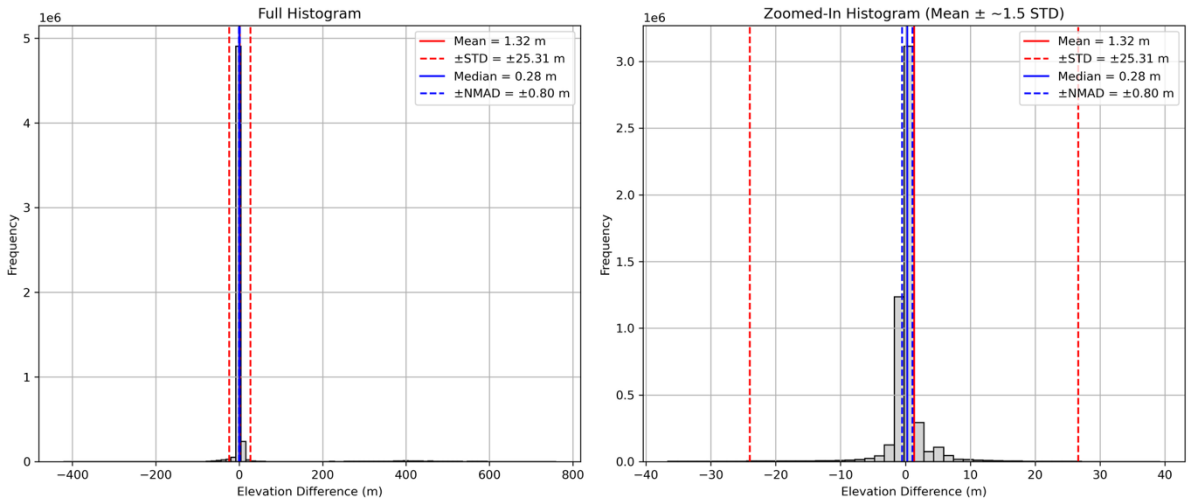
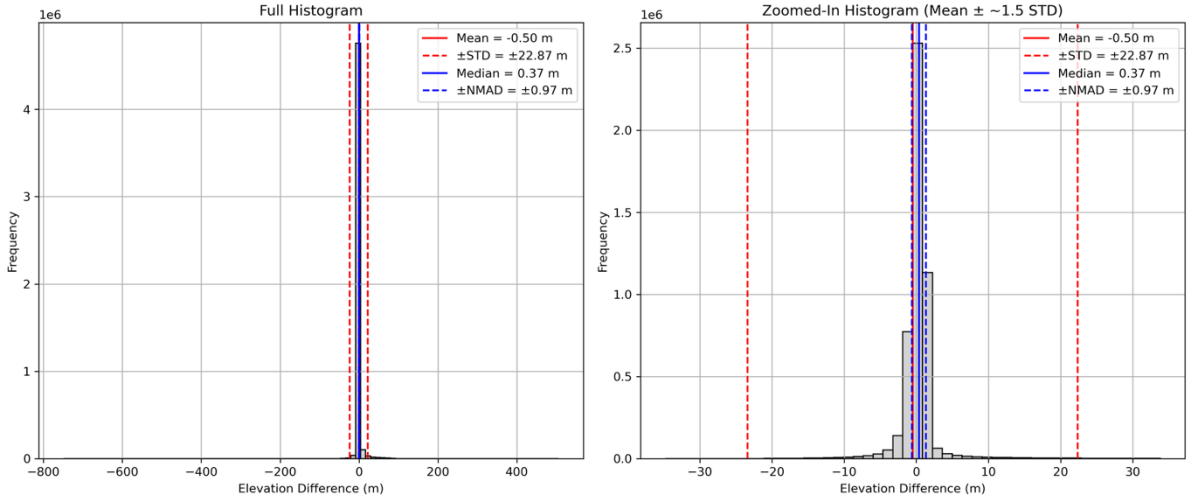
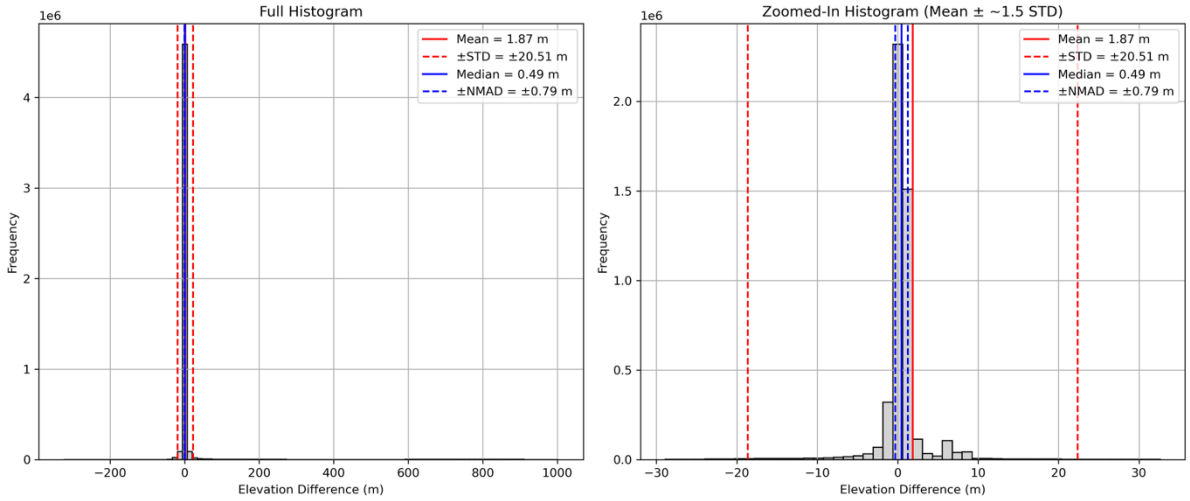
Along with the elevation products created through the methodology described in section 3.1, a bar graph representing the spread of the data was also produced. These figures plot the mean, standard deviation, median, and NMAD of the co-registration process. The statistics were then used to evaluate the viability of the product. A median close to zero with a low +/- NMAD was designated as a more viable elevation differencing product (Hugonnet et al., 2021). While the mean and standard deviation were not used for evaluation directly, they were still plotted to better represent the spread of the data within the graph.

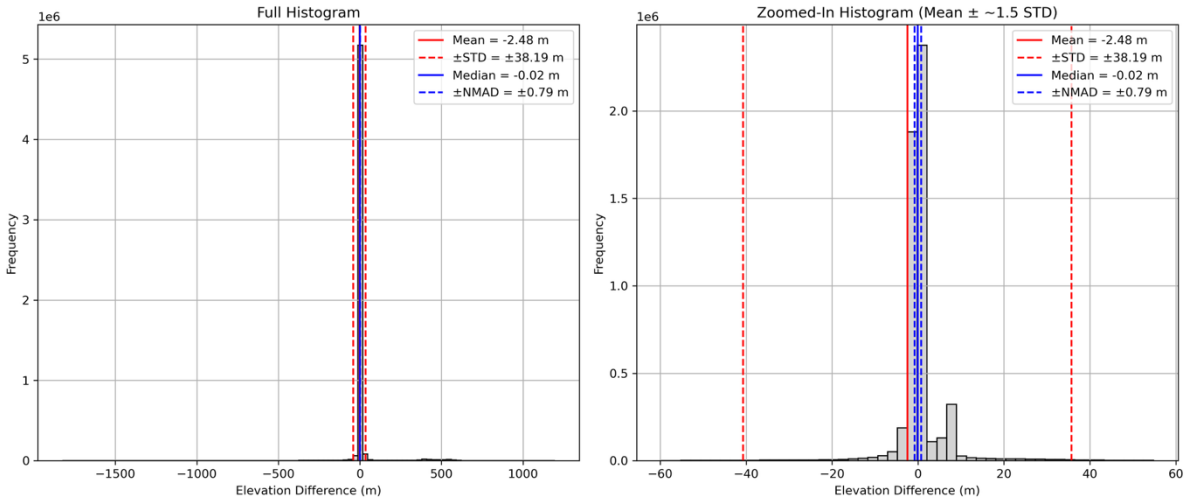
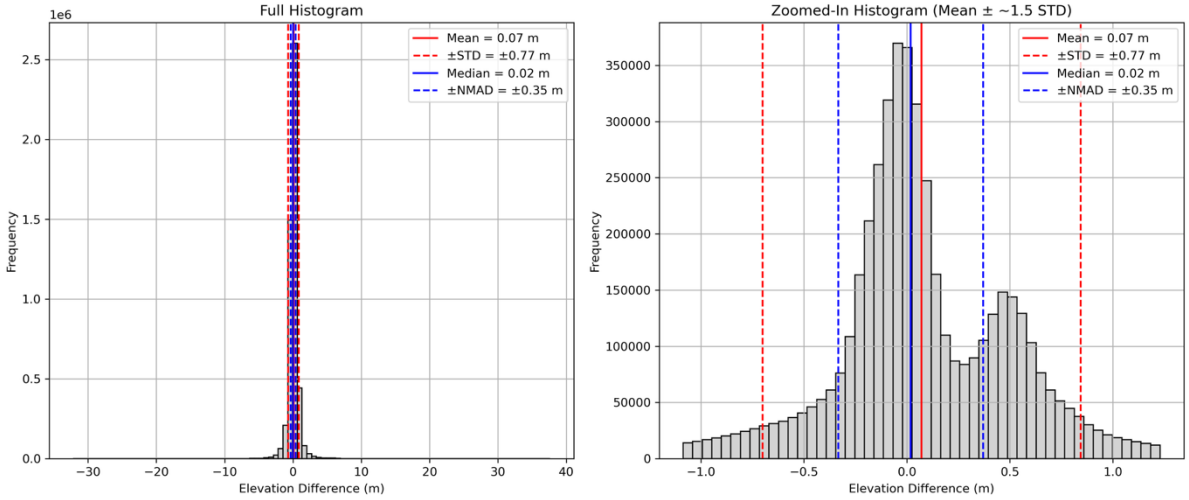
Table A-1: Table of figures of elevation change statistical spread.

Dobbin Bay Glacier Elevation Change Products Statistics	
2012 To 2013	 *Supplementary figure 2: Two histograms showing the spread of elevation values of the finalized elevation change maps. The left graph provides the full range of data, while the right graph is clipped to +/- 1.5 standard deviation. The mean (red line), standard deviation (red dotted line), median (blue line), and NMAD (dotted blue line) are provided, with their values shown in the top right.*

2013 To 2014	 *Supplementary figure 3: Two histograms showing the spread of elevation values of the finalized elevation change maps. The left graph provides the full range of data, while the right graph is clipped to +/- 1.5 standard deviation. The mean (red line), standard deviation (red dotted line), median (blue line), and NMAD (dotted blue line) are provided, with their values shown in the top right.*
2014 To 2015	 *Supplementary figure 4: Two histograms showing the spread of elevation values of the finalized elevation change maps. The left graph provides the full range of data, while the right graph is clipped to +/- 1.5 standard deviation. The mean (red line), standard deviation (red dotted line), median (blue line), and NMAD (dotted blue line) are provided, with their values shown in the top right.*
2015 To 2016	

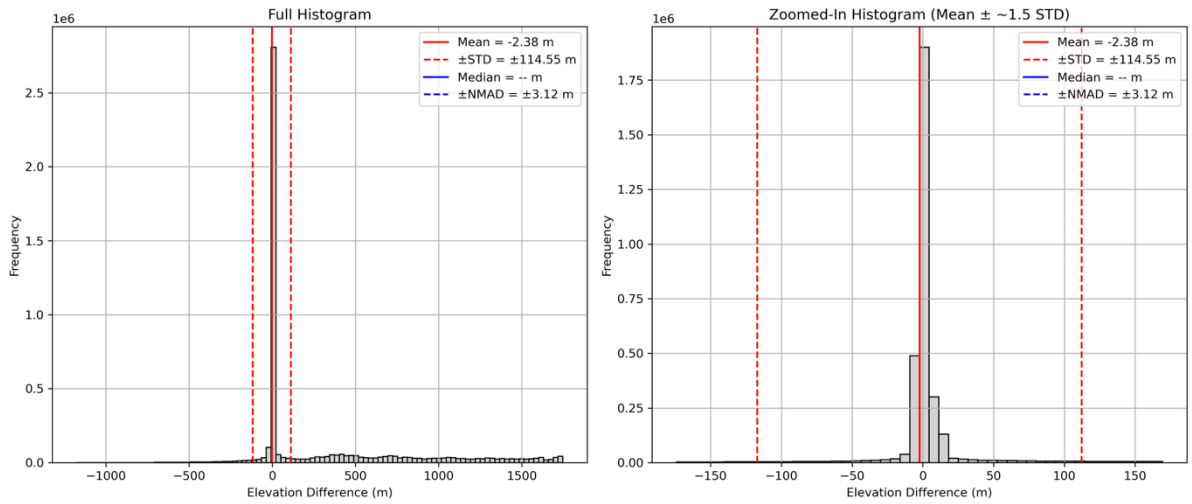
	Supplementary figure 5: Two histograms showing the spread of elevation values of the finalized elevation change maps. The left graph provides the full range of data, while the right graph is clipped to +/- 1.5 standard deviation. The mean (red line), standard deviation (red dotted line), median (blue line), and NMAD (dotted blue line) are provided, with their values shown in the top right.
2016 to 2017	 *Supplementary figure 6: Two histograms showing the spread of elevation values of the finalized elevation change maps. The left graph provides the full range of data, while the right graph is clipped to +/- 1.5 standard deviation. The mean (red line), standard deviation (red dotted line), median (blue line), and NMAD (dotted blue line) are provided, with their values shown in the top right.*
2017 to 2018	 *Supplementary figure 7: Two histograms showing the spread of elevation values of the finalized elevation change maps. The left graph provides the full range of data, while the right graph is clipped to +/- 1.5 standard deviation. The mean (red line), standard deviation (red dotted line), median (blue line), and NMAD (dotted blue line) are provided, with their values shown in the top right.*

2018 to 2019	 *Supplementary figure 8: Two histograms showing the spread of elevation values of the finalized elevation change maps. The left graph provides the full range of data, while the right graph is clipped to +/- 1.5 standard deviation. The mean (red line), standard deviation (red dotted line), median (blue line), and NMAD (dotted blue line) are provided, with their values shown in the top right.*
2019 to 2020	 *Supplementary figure 9: Two histograms showing the spread of elevation values of the finalized elevation change maps. The left graph provides the full range of data, while the right graph is clipped to +/- 1.5 standard deviation. The mean (red line), standard deviation (red dotted line), median (blue line), and NMAD (dotted blue line) are provided, with their values shown in the top right.*
2020 to 2021	

	Supplementary figure 10: Two histograms showing the spread of elevation values of the finalized elevation change maps. The left graph provides the full range of data, while the right graph is clipped to +/- 1.5 standard deviation. The mean (red line), standard deviation (red dotted line), median (blue line), and NMAD (dotted blue line) are provided, with their values shown in the top right.
2021 to 2022	 *Supplementary figure 11: Two histograms showing the spread of elevation values of the finalized elevation change maps. The left graph provides the full range of data, while the right graph is clipped to +/- 1.5 standard deviation. The mean (red line), standard deviation (red dotted line), median (blue line), and NMAD (dotted blue line) are provided, with their values shown in the top right.*
2012 to 2020	 *Supplementary figure 12: Two histograms showing the spread of elevation values of the finalized elevation change maps. The left graph provides the full range of data, while the right graph is clipped to +/- 1.5 standard deviation. The mean (red line), standard deviation (red dotted line), median (blue line), and NMAD (dotted blue line) are provided, with their values shown in the top right.*

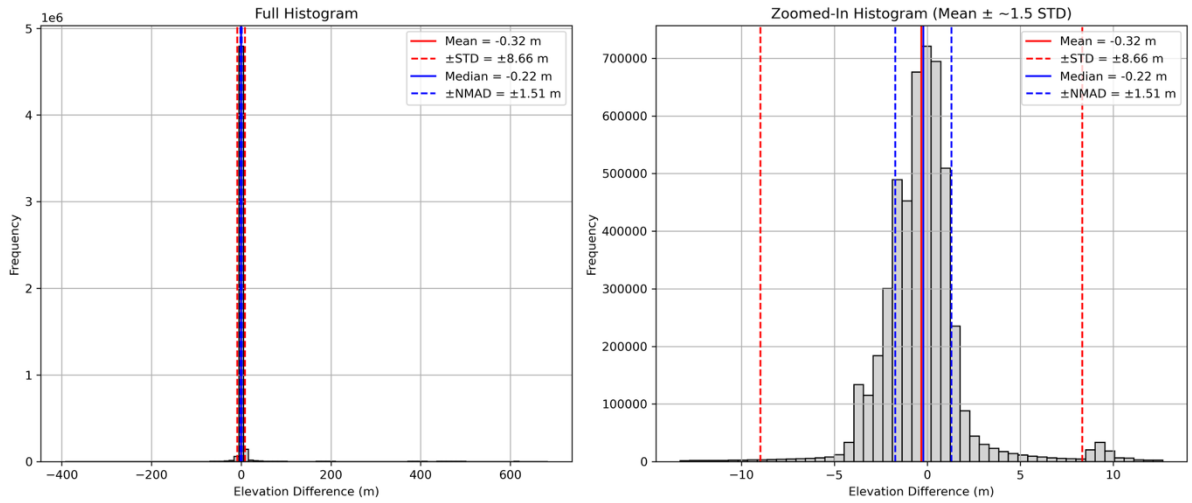
Parrish Glacier Elevation Change Products Statistics

2011 To 2012

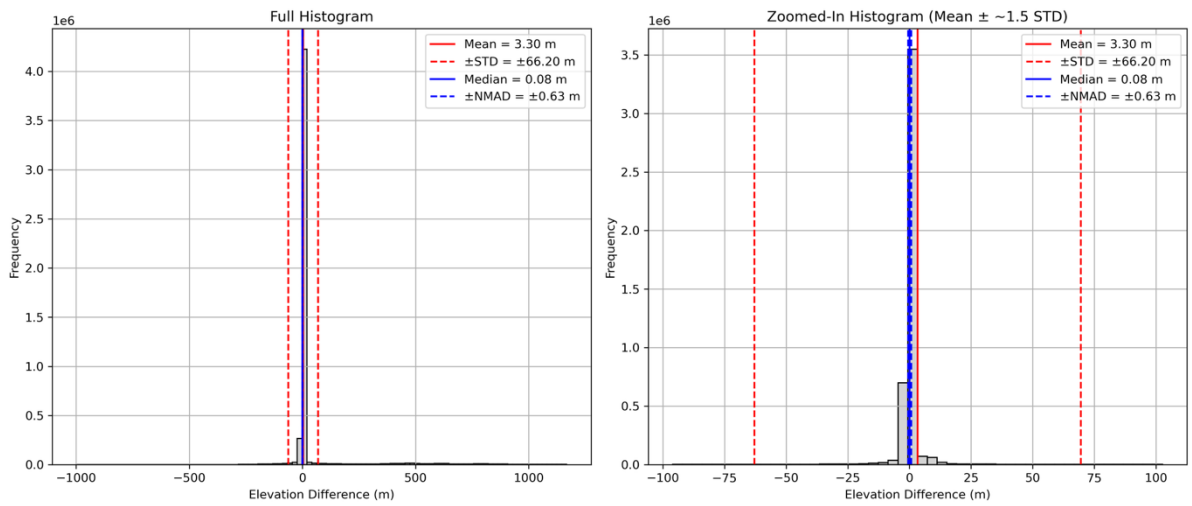
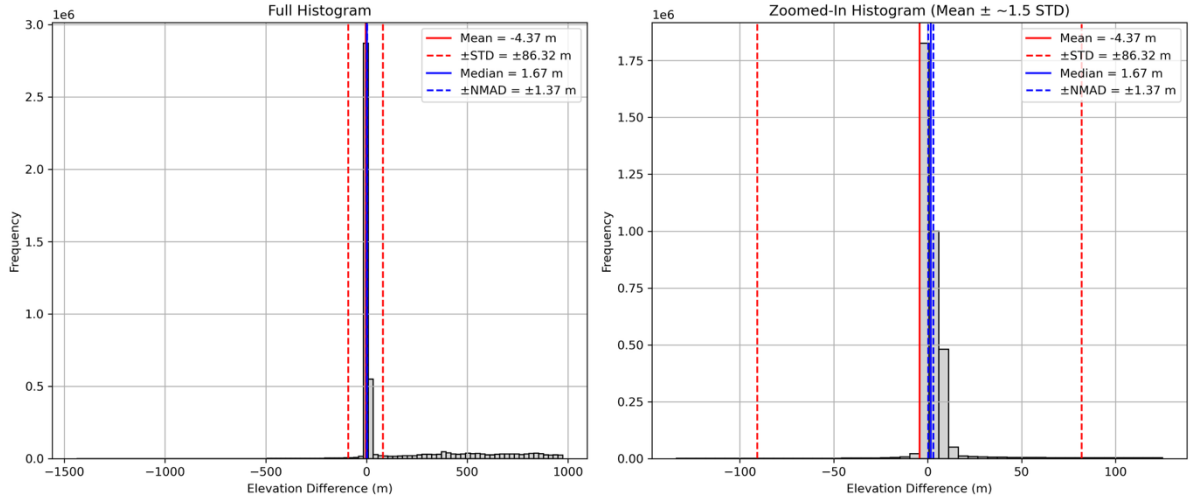
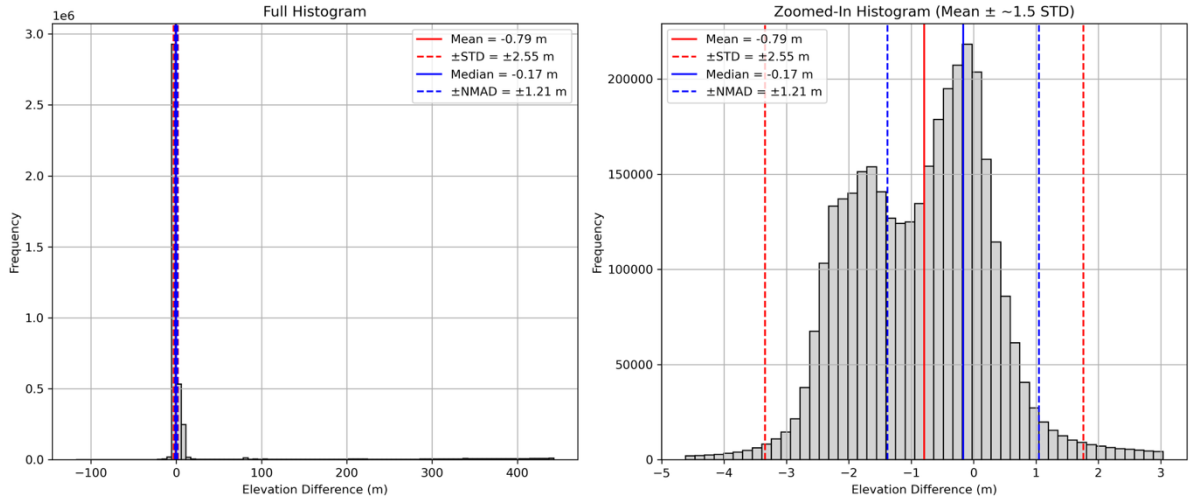


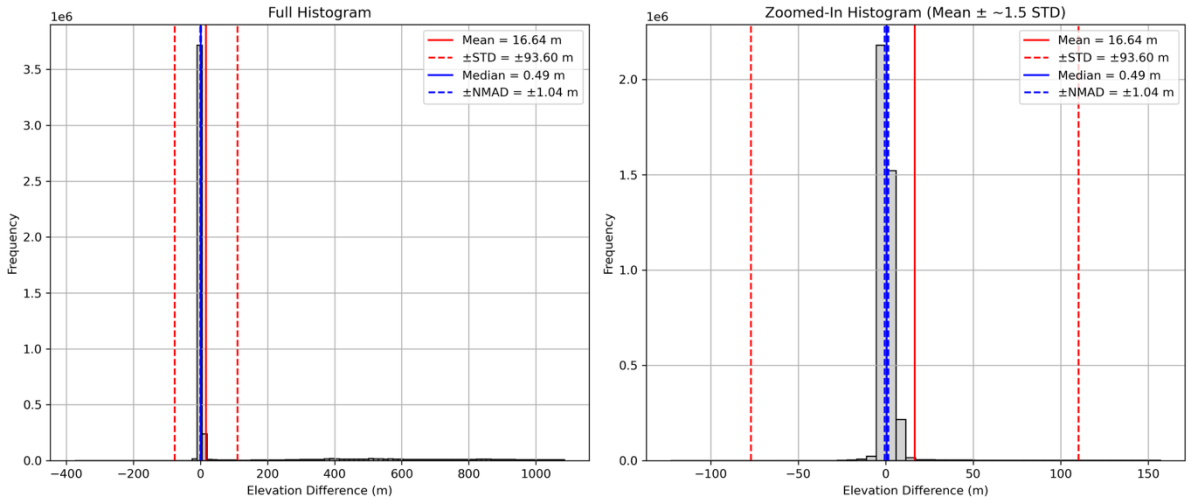
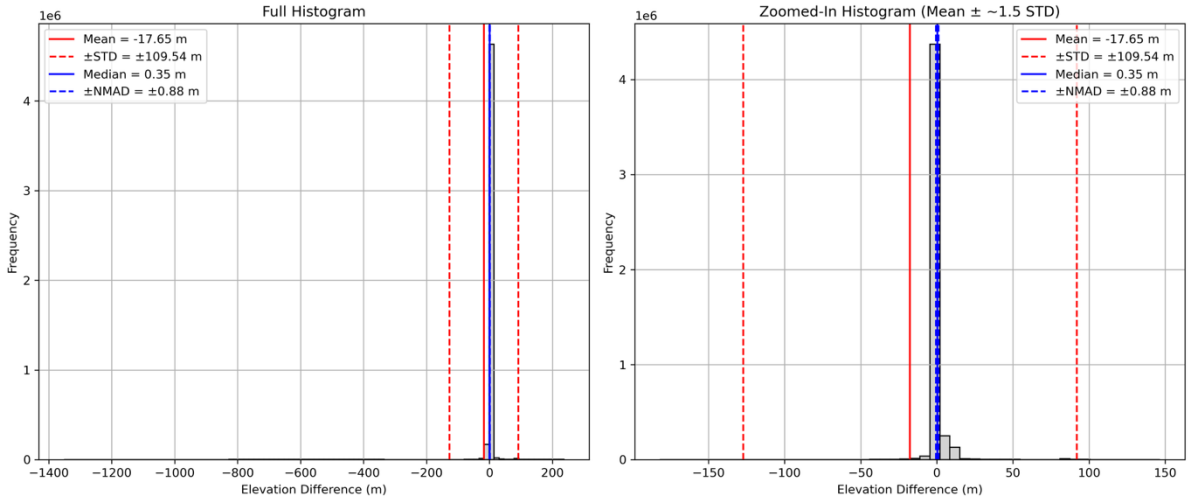
Supplementary figure 13: Two histograms showing the spread of elevation values of the finalized elevation change maps. The left graph provides the full range of data, while the right graph is clipped to +/- 1.5 standard deviation. The mean (red line), standard deviation (red dotted line), median (blue line), and NMAD (dotted blue line) are provided, with their values shown in the top right.

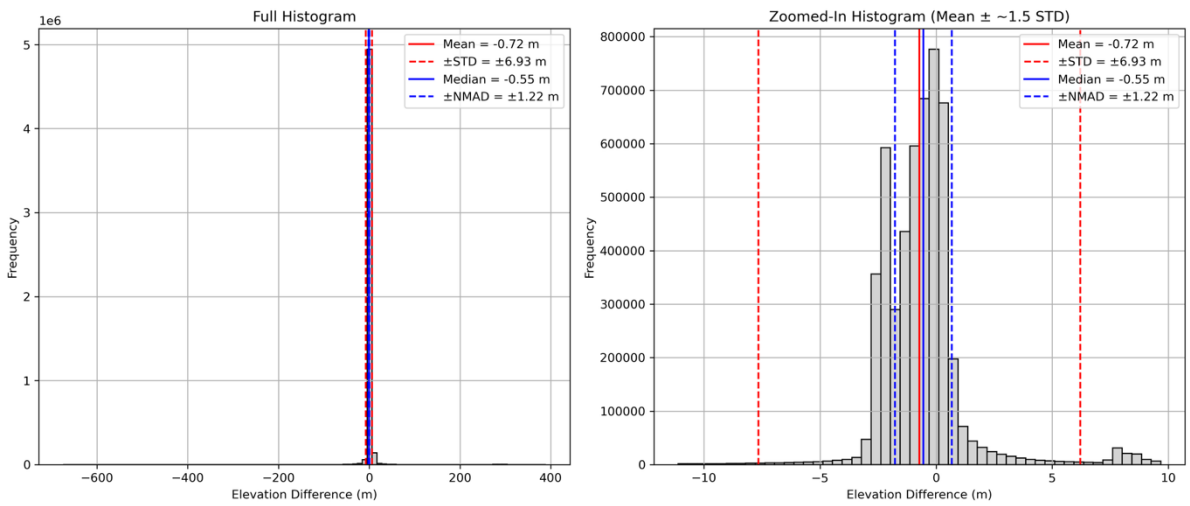
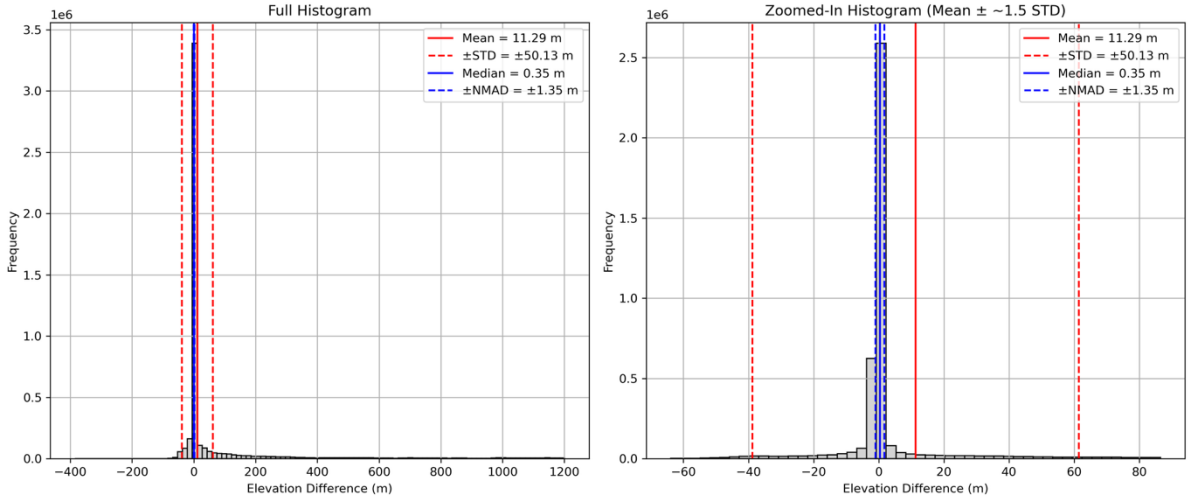
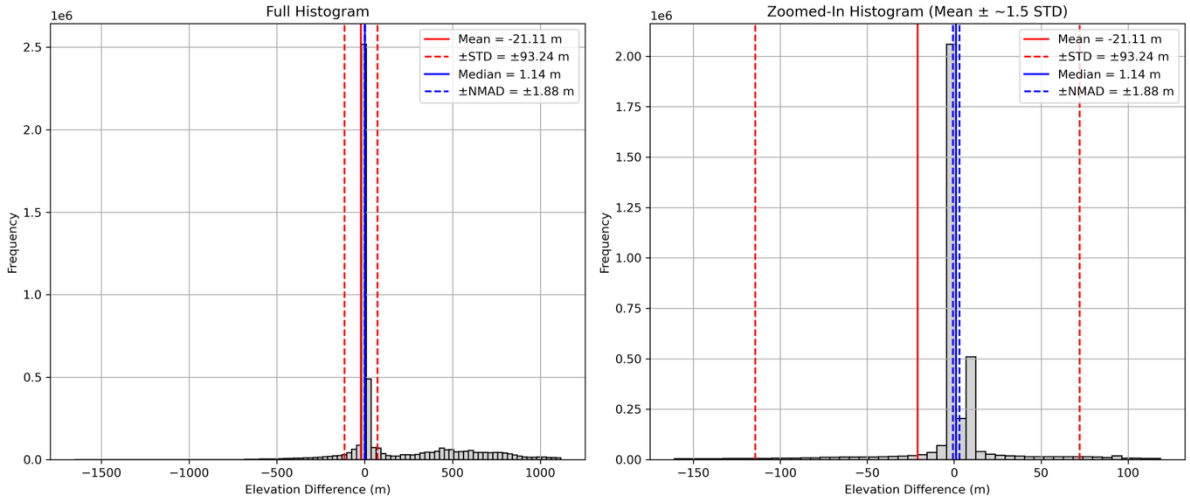
2012 to 2013

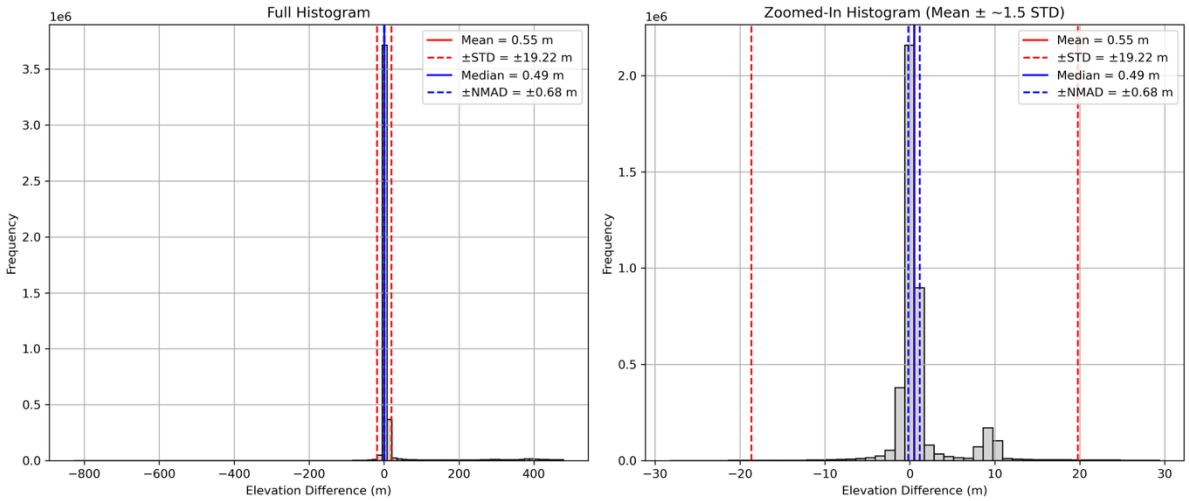
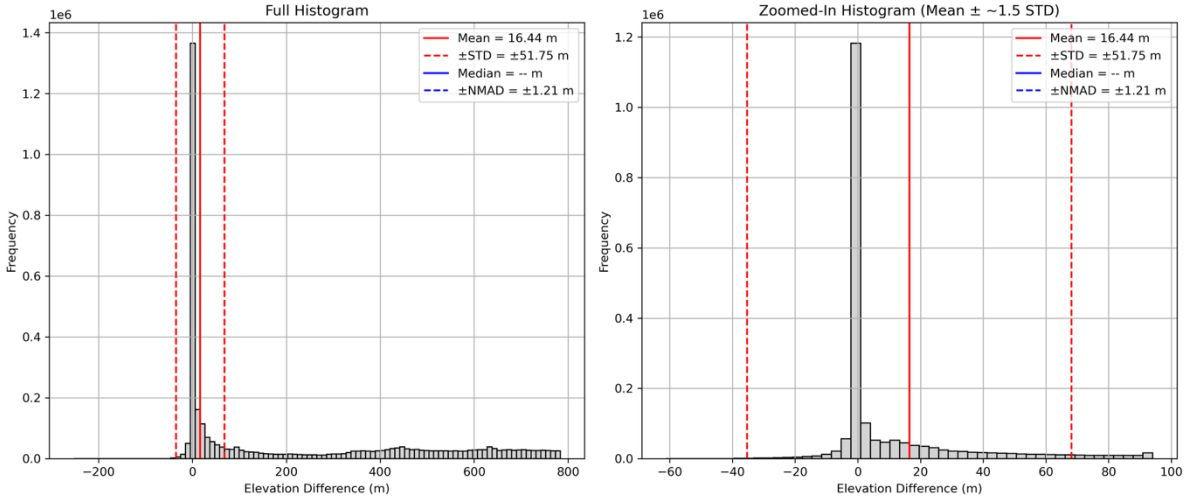


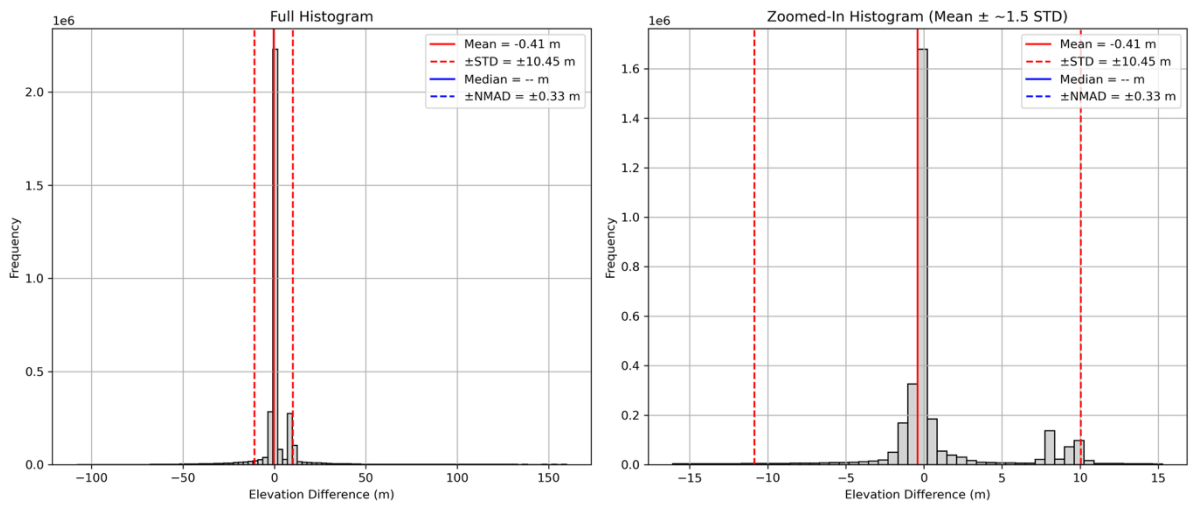
Supplementary figure 14: Two histograms showing the spread of elevation values of the finalized elevation change maps. The left graph provides the full range of data, while the right graph is clipped to +/- 1.5 standard deviation. The mean (red line), standard deviation (red dotted line), median (blue line), and NMAD (dotted blue line) are provided, with their values shown in the top right.

2013 to 2014	 *Supplementary figure 15: Two histograms showing the spread of elevation values of the finalized elevation change maps. The left graph provides the full range of data, while the right graph is clipped to +/- 1.5 standard deviation. The mean (red line), standard deviation (red dotted line), median (blue line), and NMAD (dotted blue line) are provided, with their values shown in the top right.*
2014 to 2015	 *Supplementary figure 16: Two histograms showing the spread of elevation values of the finalized elevation change maps. The left graph provides the full range of data, while the right graph is clipped to +/- 1.5 standard deviation. The mean (red line), standard deviation (red dotted line), median (blue line), and NMAD (dotted blue line) are provided, with their values shown in the top right.*
2015 to 2016	

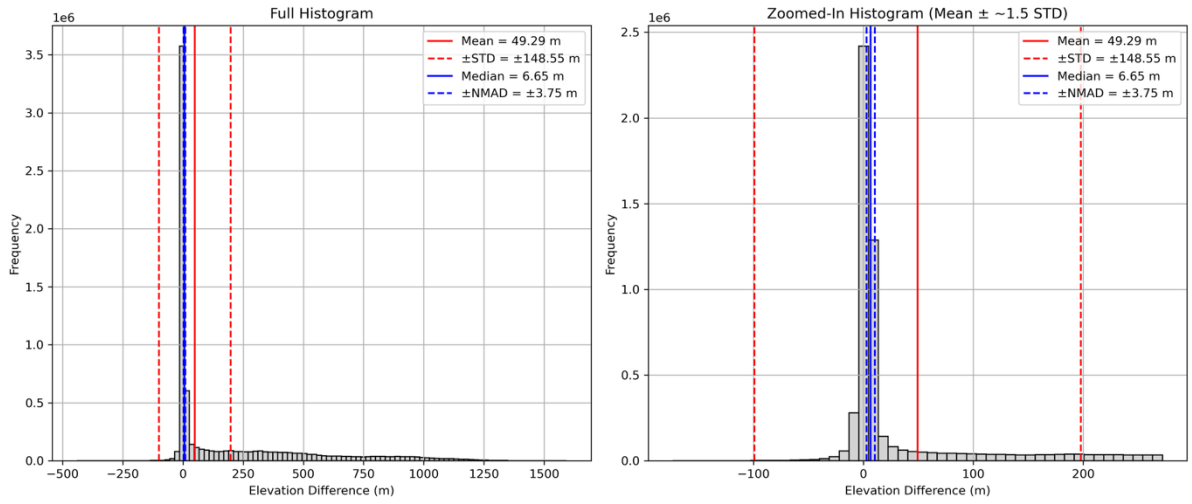
	Supplementary figure 17: Two histograms showing the spread of elevation values of the finalized elevation change maps. The left graph provides the full range of data, while the right graph is clipped to +/- 1.5 standard deviation. The mean (red line), standard deviation (red dotted line), median (blue line), and NMAD (dotted blue line) are provided, with their values shown in the top right.
2016 to 2017	 *Supplementary figure 18: Two histograms showing the spread of elevation values of the finalized elevation change maps. The left graph provides the full range of data, while the right graph is clipped to +/- 1.5 standard deviation. The mean (red line), standard deviation (red dotted line), median (blue line), and NMAD (dotted blue line) are provided, with their values shown in the top right.*
2017 to 2018	 *Supplementary figure 19: Two histograms showing the spread of elevation values of the finalized elevation change maps. The left graph provides the full range of data, while the right graph is clipped to +/- 1.5 standard deviation. The mean (red line), standard deviation (red dotted line), median (blue line), and NMAD (dotted blue line) are provided, with their values shown in the top right.*

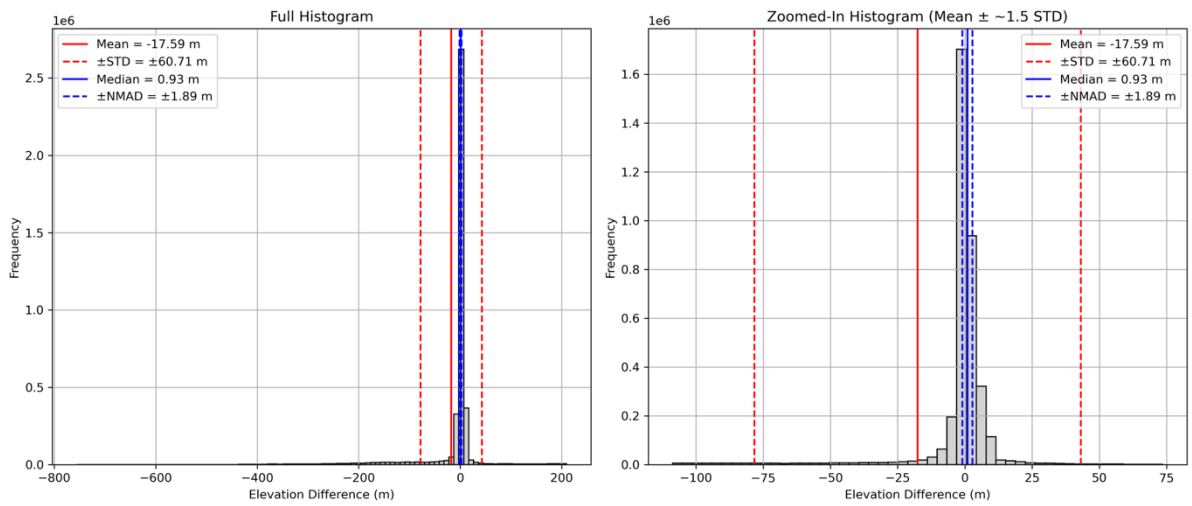
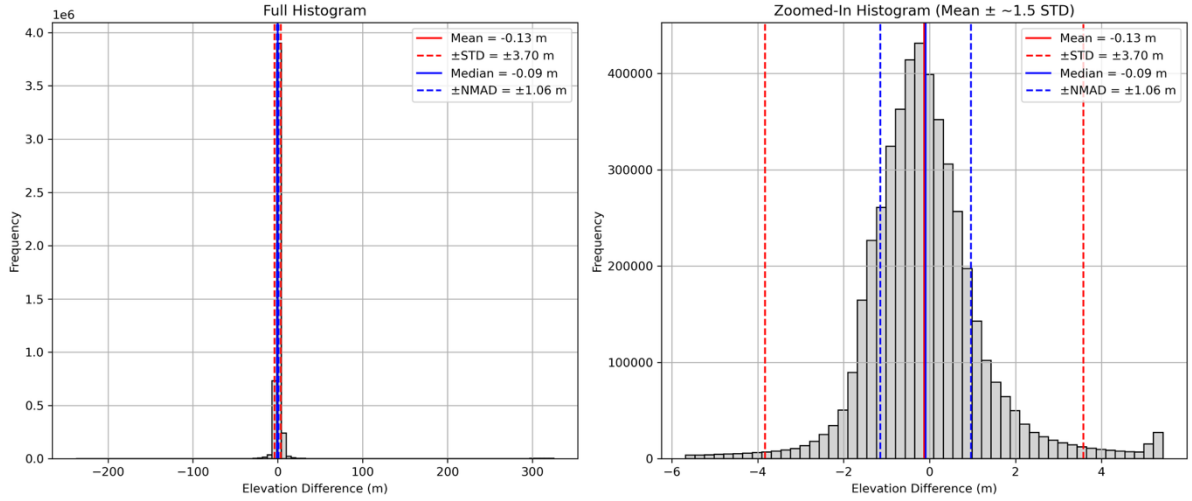
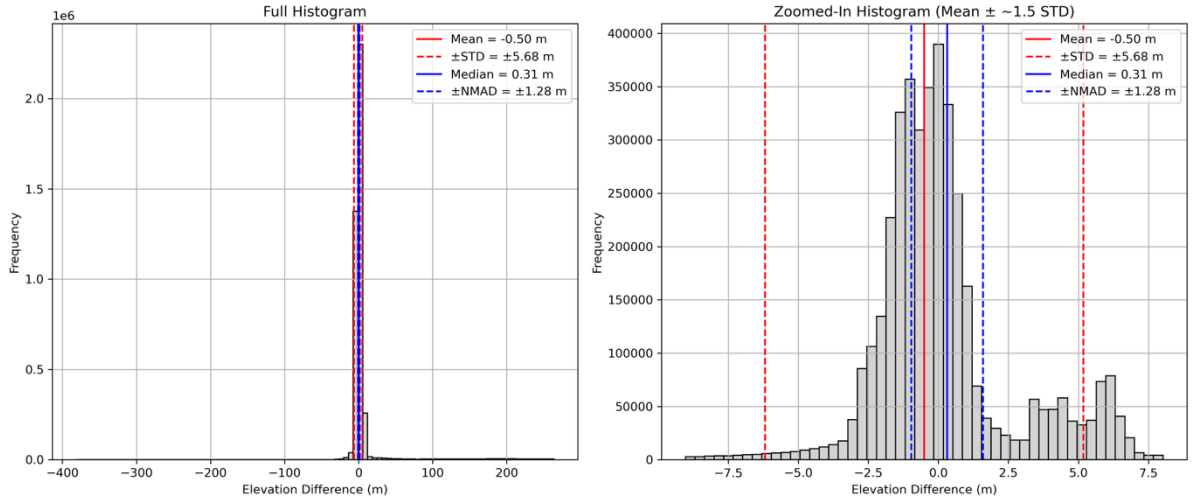
2018 to 2019	 *Supplementary figure 20: Two histograms showing the spread of elevation values of the finalized elevation change maps. The left graph provides the full range of data, while the right graph is clipped to +/- 1.5 standard deviation. The mean (red line), standard deviation (red dotted line), median (blue line), and NMAD (dotted blue line) are provided, with their values shown in the top right.*
2019 to 2020	 *Supplementary figure 21: Two histograms showing the spread of elevation values of the finalized elevation change maps. The left graph provides the full range of data, while the right graph is clipped to +/- 1.5 standard deviation. The mean (red line), standard deviation (red dotted line), median (blue line), and NMAD (dotted blue line) are provided, with their values shown in the top right.*
2020 to 2021	

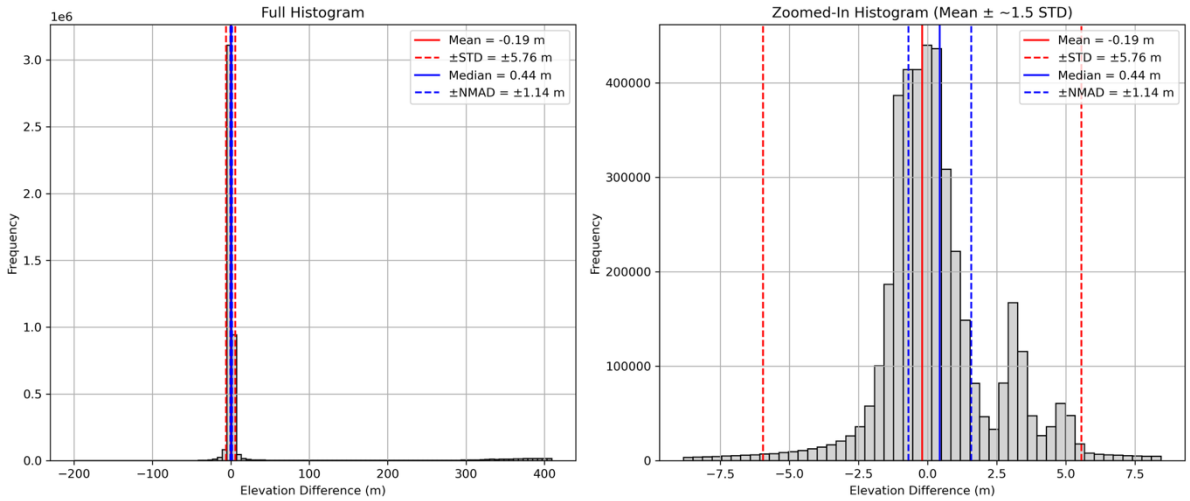
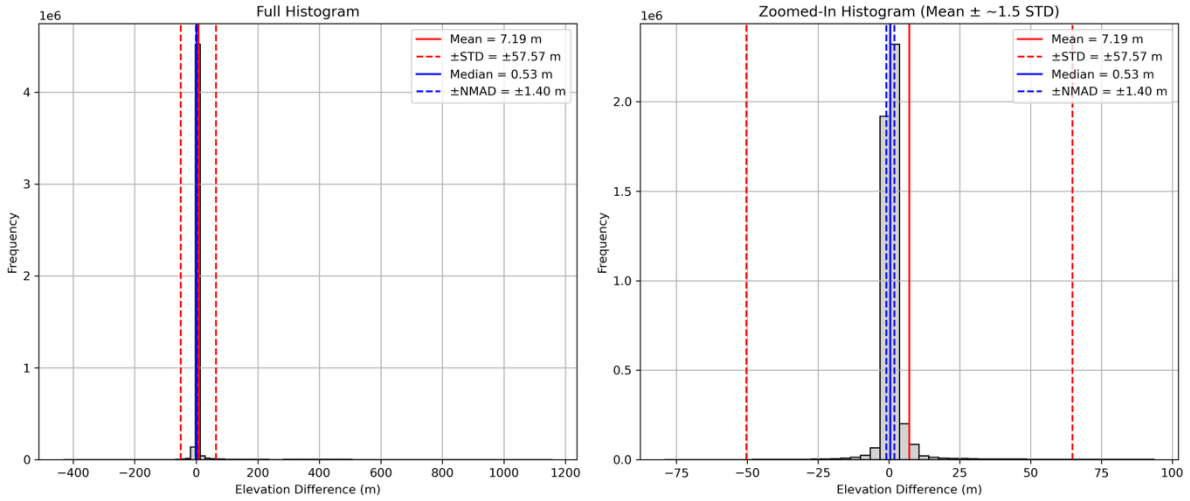
	Supplementary figure 22: Two histograms showing the spread of elevation values of the finalized elevation change maps. The left graph provides the full range of data, while the right graph is clipped to +/- 1.5 standard deviation. The mean (red line), standard deviation (red dotted line), median (blue line), and NMAD (dotted blue line) are provided, with their values shown in the top right.
2021 to 2022	 *Supplementary figure 23: Two histograms showing the spread of elevation values of the finalized elevation change maps. The left graph provides the full range of data, while the right graph is clipped to +/- 1.5 standard deviation. The mean (red line), standard deviation (red dotted line), median (blue line), and NMAD (dotted blue line) are provided, with their values shown in the top right.*
2022 to 2023	 *Supplementary figure 24: Two histograms showing the spread of elevation values of the finalized elevation change maps. The left graph provides the full range of data, while the right graph is clipped to +/- 1.5 standard deviation. The mean (red line), standard deviation (red dotted line), median (blue line), and NMAD (dotted blue line) are provided, with their values shown in the top right.*

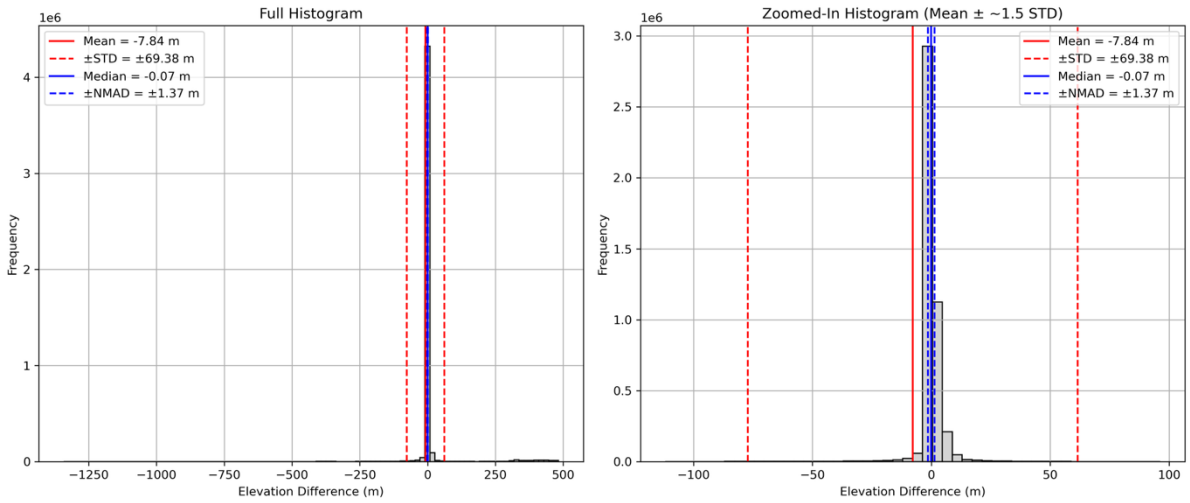
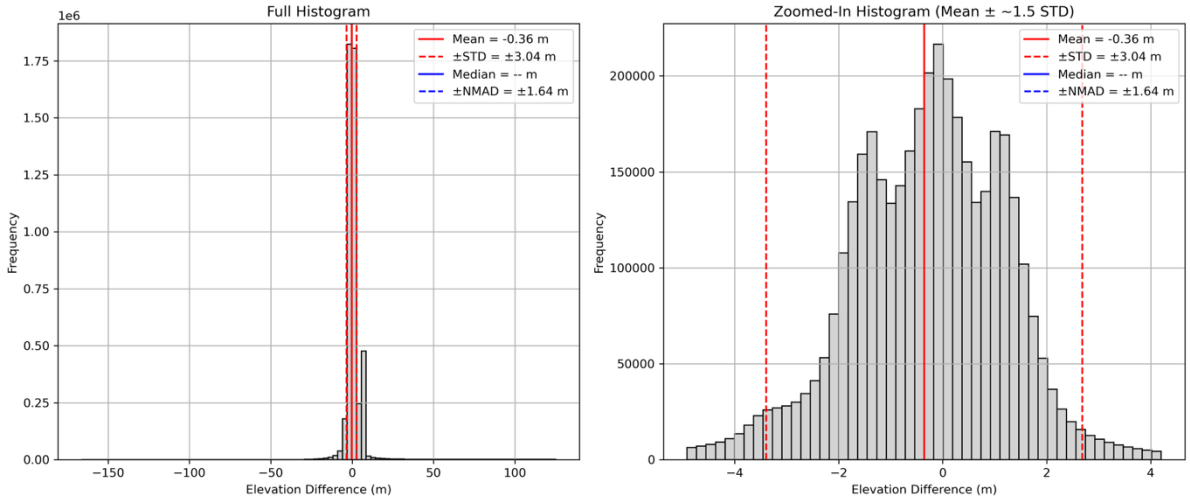
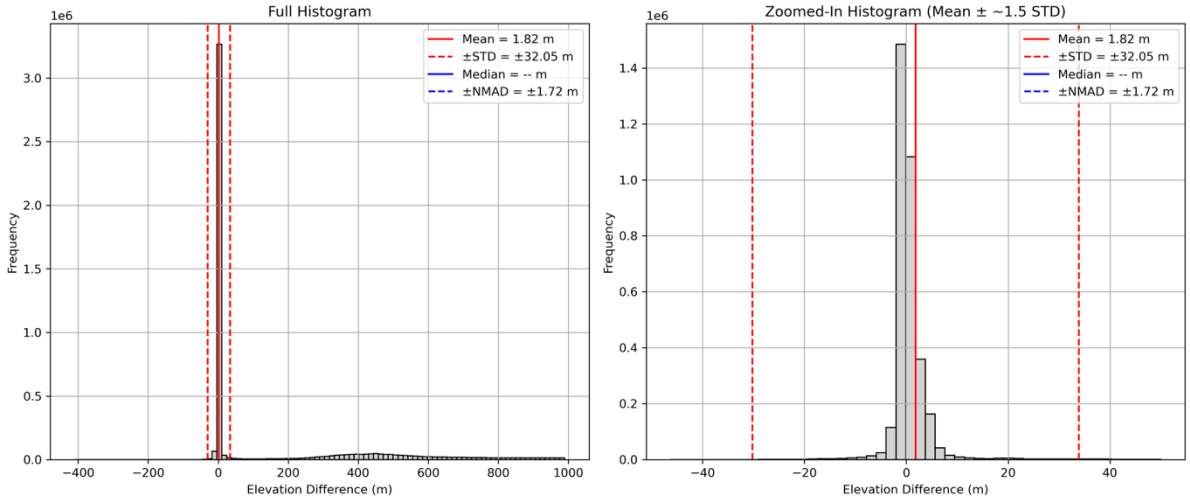
2011 to 2021	 *Supplementary figure 25: Two histograms showing the spread of elevation values of the finalized elevation change maps. The left graph provides the full range of data, while the right graph is clipped to +/- 1.5 standard deviation. The mean (red line), standard deviation (red dotted line), median (blue line), and NMAD (dotted blue line) are provided, with their values shown in the top right.*

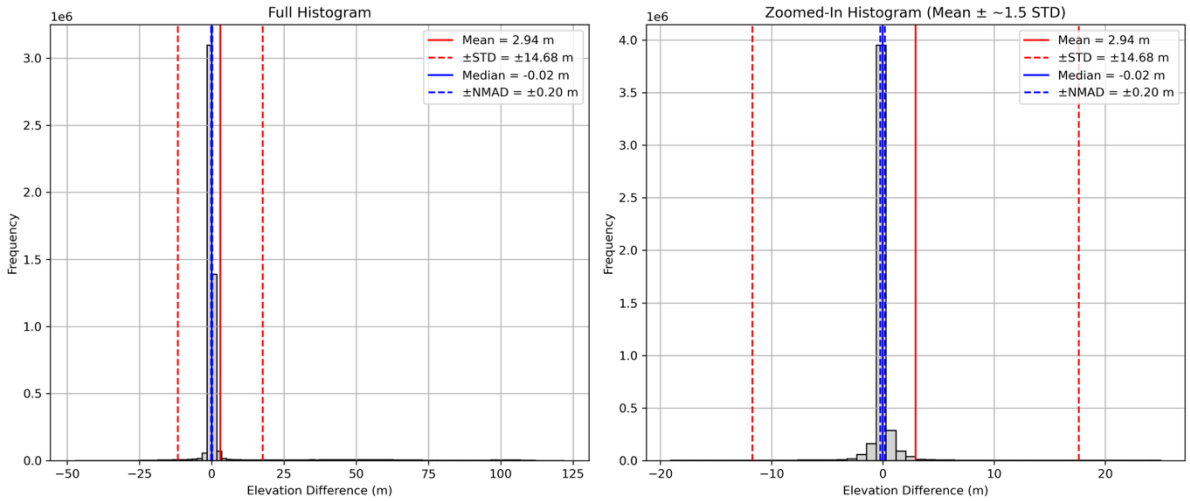
Eugenie Glacier Lower Elevation Change products statistics

2012 To 2013	 *Supplementary figure 26: Two histograms showing the spread of elevation values of the finalized elevation change maps. The left graph provides the full range of data, while the right graph is clipped to +/- 1.5 standard deviation. The mean (red line), standard deviation (red dotted line), median (blue line), and NMAD (dotted blue line) are provided, with their values shown in the top right.*

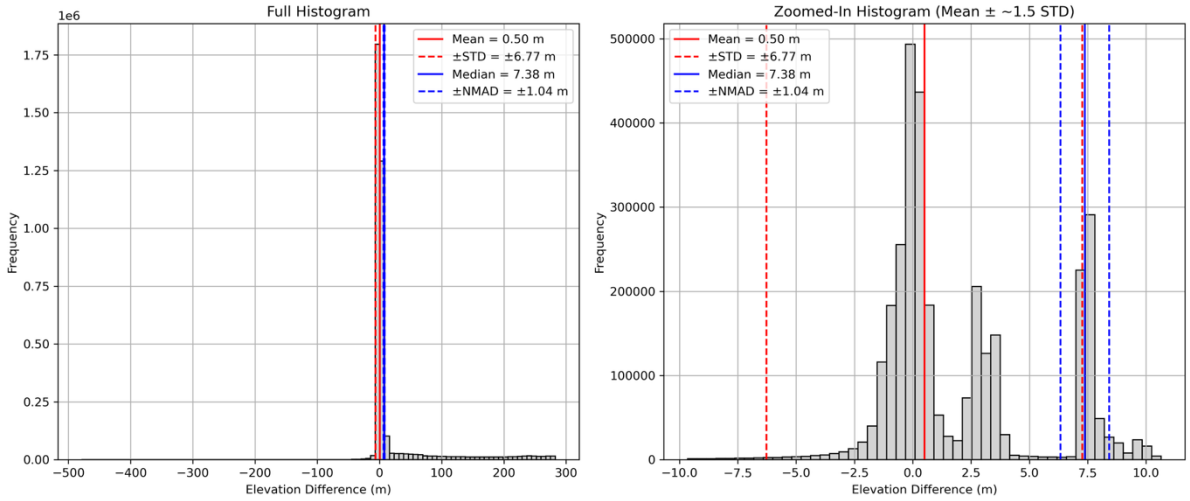
2013 to 2015	 *Supplementary figure 27: Two histograms showing the spread of elevation values of the finalized elevation change maps. The left graph provides the full range of data, while the right graph is clipped to +/- 1.5 standard deviation. The mean (red line), standard deviation (red dotted line), median (blue line), and NMAD (dotted blue line) are provided, with their values shown in the top right.*
2015 to 2016	 *Supplementary figure 28: Two histograms showing the spread of elevation values of the finalized elevation change maps. The left graph provides the full range of data, while the right graph is clipped to +/- 1.5 standard deviation. The mean (red line), standard deviation (red dotted line), median (blue line), and NMAD (dotted blue line) are provided, with their values shown in the top right.*
2016 to 2017	

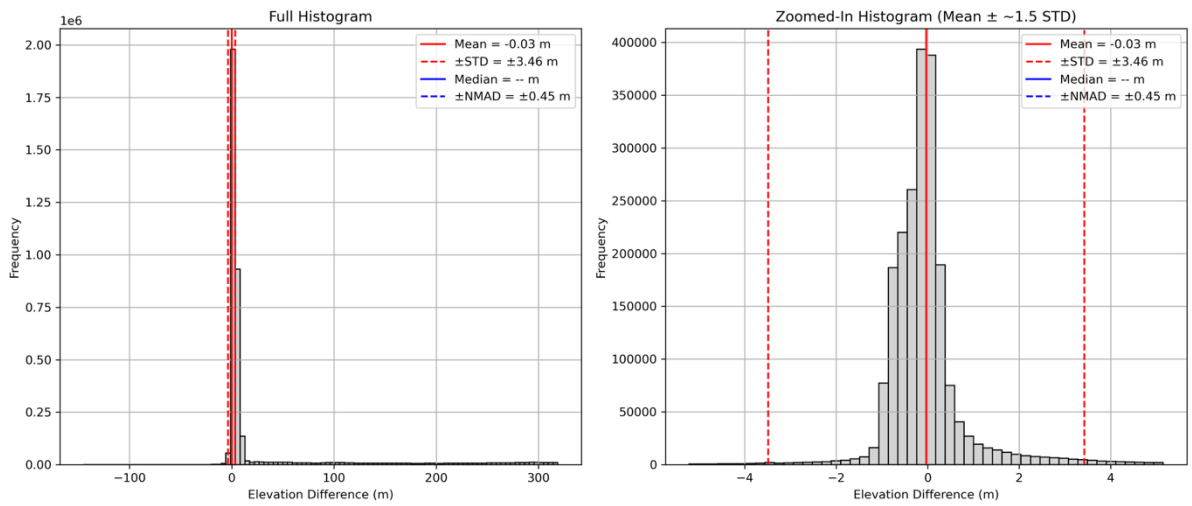
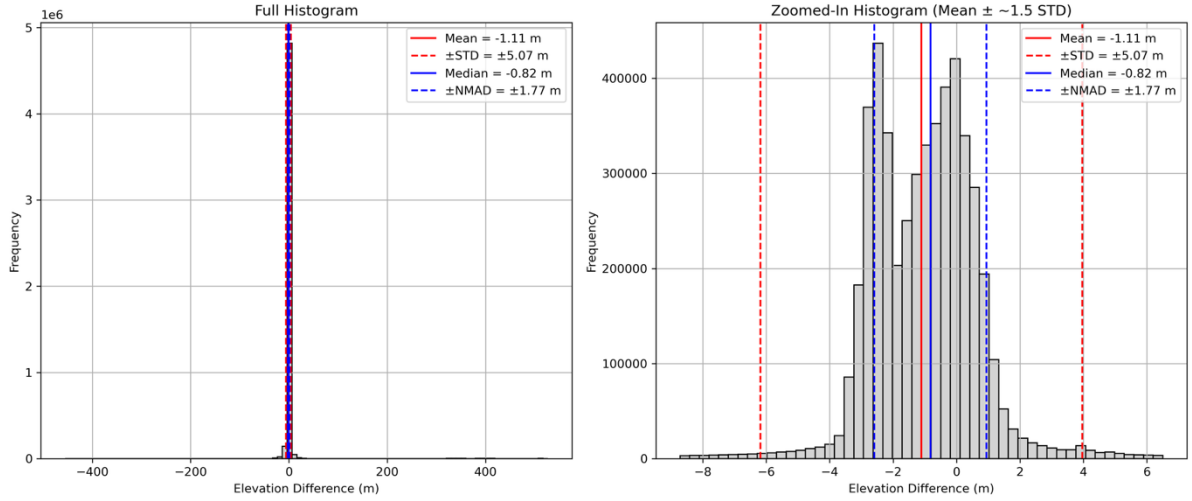
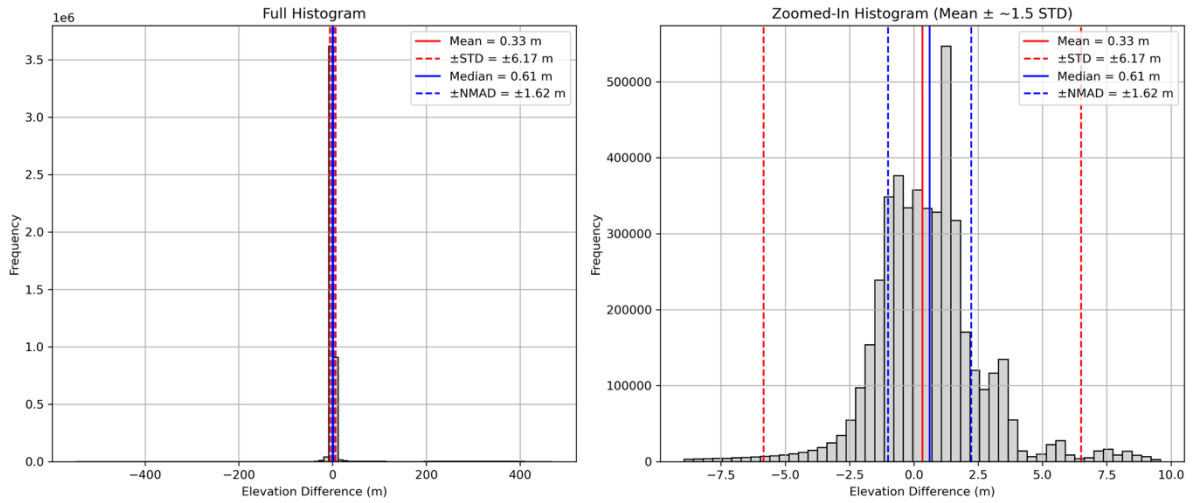
	Supplementary figure 29: Two histograms showing the spread of elevation values of the finalized elevation change maps. The left graph provides the full range of data, while the right graph is clipped to +/- 1.5 standard deviation. The mean (red line), standard deviation (red dotted line), median (blue line), and NMAD (dotted blue line) are provided, with their values shown in the top right.
2017 to 2018	 *Supplementary figure 30: Two histograms showing the spread of elevation values of the finalized elevation change maps. The left graph provides the full range of data, while the right graph is clipped to +/- 1.5 standard deviation. The mean (red line), standard deviation (red dotted line), median (blue line), and NMAD (dotted blue line) are provided, with their values shown in the top right.*
2018 to 2019	 *Supplementary figure 31: Two histograms showing the spread of elevation values of the finalized elevation change maps. The left graph provides the full range of data, while the right graph is clipped to +/- 1.5 standard deviation. The mean (red line), standard deviation (red dotted line), median (blue line), and NMAD (dotted blue line) are provided, with their values shown in the top right.*

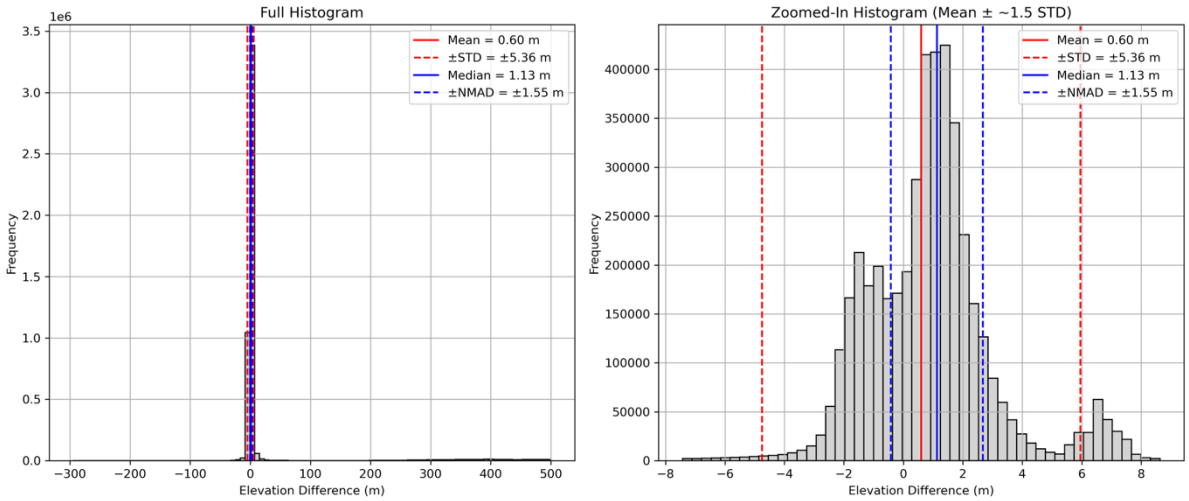
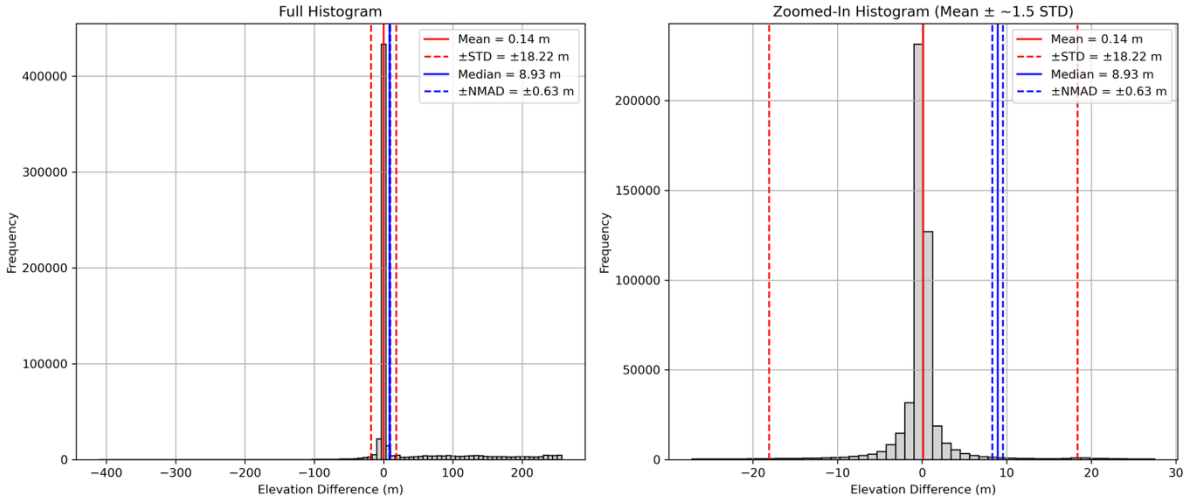
2019 to 2020	 *Supplementary figure 32: Two histograms showing the spread of elevation values of the finalized elevation change maps. The left graph provides the full range of data, while the right graph is clipped to +/- 1.5 standard deviation. The mean (red line), standard deviation (red dotted line), median (blue line), and NMAD (dotted blue line) are provided, with their values shown in the top right.*
2020 to 2021	 *Supplementary figure 33: Two histograms showing the spread of elevation values of the finalized elevation change maps. The left graph provides the full range of data, while the right graph is clipped to +/- 1.5 standard deviation. The mean (red line), standard deviation (red dotted line), median (blue line), and NMAD (dotted blue line) are provided, with their values shown in the top right.*
2021 to 2022	

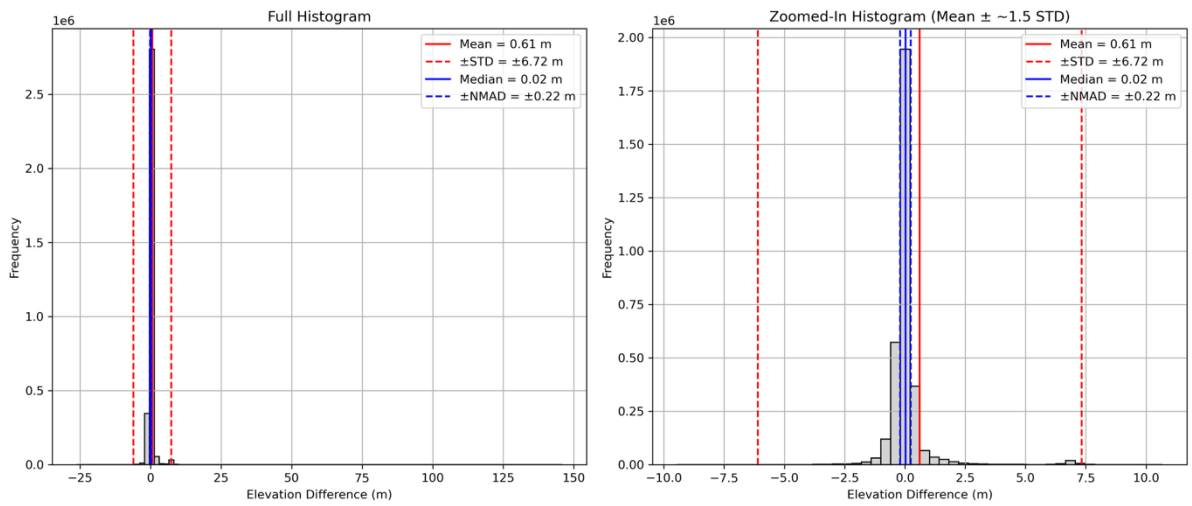
	Supplementary figure 34: Two histograms showing the spread of elevation values of the finalized elevation change maps. The left graph provides the full range of data, while the right graph is clipped to +/- 1.5 standard deviation. The mean (red line), standard deviation (red dotted line), median (blue line), and NMAD (dotted blue line) are provided, with their values shown in the top right.
2012 to 2022	 *Supplementary figure 35: Two histograms showing the spread of elevation values of the finalized elevation change maps. The left graph provides the full range of data, while the right graph is clipped to +/- 1.5 standard deviation. The mean (red line), standard deviation (red dotted line), median (blue line), and NMAD (dotted blue line) are provided, with their values shown in the top right.*

Eugenie Glacier Upper Elevation Change

2012 to 2013	 *Supplementary figure 36: Two histograms showing the spread of elevation values of the finalized elevation change maps. The left graph provides the full range of data, while the right graph is clipped to +/- 1.5 standard deviation. The mean (red line), standard deviation (red dotted line), median (blue line), and NMAD (dotted blue line) are provided, with their values shown in the top right.*

2013 to 2015	 *Supplementary figure 37: Two histograms showing the spread of elevation values of the finalized elevation change maps. The left graph provides the full range of data, while the right graph is clipped to +/- 1.5 standard deviation. The mean (red line), standard deviation (red dotted line), median (blue line), and NMAD (dotted blue line) are provided, with their values shown in the top right.*
2015 to 2016	 *Supplementary figure 38: Two histograms showing the spread of elevation values of the finalized elevation change maps. The left graph provides the full range of data, while the right graph is clipped to +/- 1.5 standard deviation. The mean (red line), standard deviation (red dotted line), median (blue line), and NMAD (dotted blue line) are provided, with their values shown in the top right.*
2016 to 2017	

	Supplementary figure 39: Two histograms showing the spread of elevation values of the finalized elevation change maps. The left graph provides the full range of data, while the right graph is clipped to +/- 1.5 standard deviation. The mean (red line), standard deviation (red dotted line), median (blue line), and NMAD (dotted blue line) are provided, with their values shown in the top right.
2017 to 2018	 *Supplementary figure 40: Two histograms showing the spread of elevation values of the finalized elevation change maps. The left graph provides the full range of data, while the right graph is clipped to +/- 1.5 standard deviation. The mean (red line), standard deviation (red dotted line), median (blue line), and NMAD (dotted blue line) are provided, with their values shown in the top right.*
2018 to 2019	 *Supplementary figure 41: Two histograms showing the spread of elevation values of the finalized elevation change maps. The left graph provides the full range of data, while the right graph is clipped to +/- 1.5 standard deviation. The mean (red line), standard deviation (red dotted line), median (blue line), and NMAD (dotted blue line) are provided, with their values shown in the top right.*

2012 to 2022	

Supplementary figure 42: Two histograms showing the spread of elevation values of the finalized elevation change maps. The left graph provides the full range of data, while the right graph is clipped to +/- 1.5 standard deviation. The mean (red line), standard deviation (red dotted line), median (blue line), and NMAD (dotted blue line) are provided, with their values shown in the top right.

A – 3: Satellite Imagery for Terminus Delineation

Table a-2: Summary of optical imagery utilized by this study to delineate terminus positions for each of the study glaciers.

Date	Image Name	Sensor	Coverage
19590705	A16616_055.tif_1959_07_05	Air Photo	Dobbin
19590705	A16616_056.tif_1959_07_05	Air Photo	Eugenie
19590715	A16721_085.tif	Ariel Photo	Parrish
19750806	LM01_L1TP_055002_19750806_20200908_02_T2_refl.tif	Landsat1	Parrish
19760921	Multispectral_LM01_L1TP_053002_19760921_20200907_02_T2_MTL	LandSat1	Dobbin, Parrish
19770809	LM01_L1TP_054002_19770809_20200907_02_T2_refl.tif	Landsat1	Parrish
19770826	LM01_L1TP_053002_19770826_20200907_02_T2_refl.tif	Landsat1	Parrish
19790731	Multispectral_LM02_L1TP_061001_19790731_20200906_02_T2_MTL	Landsat2	Parrish
19800918	Multispectral_LM02_L1TP_062001_19800918_20200905_02_T2_MTL	Landsat2	Parrish
19810609	Multispectral_LM02_L1TP_056002_19810609_20200905_02_T2_MTL	Landsat2	Parrish
19820803	Multispectral_LM03_L1TP_053002_19820803_20200904_02_T2_MTL	Landsat3	Parrish

19870612	004-005_S1_085-136-0_1987-06-12-18-39-16_HRV-1_P_E2_TT	SPOT	Parrish
19870816	c1987_08_16_ProjectRaster	SPOT	Dobbin, Eugenie
19880723	001-001_S1_084-136-0_1988-07-23-01-12-43_HRV-1_X_E2_KK	SPOT	Parrish
19880727	c1988_07_27_ProjectRaster	SPOT	Eugenie
19890723	c1989_07_23_ProjectRaster	SPOT	Dobbin
19940705	021-023_S3_085-136-0_1994-07-05-18-32-01_HRV-1_X_DT_KK	SPOT	Parrish
19950527	013-015_S3_086-137-0_1995-05-27-19-02-17_HRV-1_X_E1_TT	SPOT	Parrish
19960811	015-015_S3_085-136-0_1996-08-11-19-01-32_HRV-1_X_E1_TT	SPOT	Parrish
19990707	Multispectral_LE07_L1TP_044003_19990707_20200918_02_T1_MTL	Landsat7	Eugenie, Parrish
19990709	Multispectral_LE07_L1TP_042003_19990709_20200918_02_T1_MTL	Landsat7	Dobbin
20000609	Multispectral_LE07_L1TP_042003_20000609_20201020_02_T1_MTL	Landsat7	Parrish
20000616	Multispectral_LE07_L1TP_043003_20000616_20200918_02_T1_MTL	Landsat7	Dobbin, Eugenie
20010612	Multispectral_LE07_L1TP_042003_20010612_20201020_02_T1_MTL	Landsat7	Eugenie, Parrish
20010721	Multispectral_LE07_L1TP_043003_20010721_20200917_02_T1_MTL	Landsat7	Dobbin, Eugenie
20020615	Multispectral_LE07_L1TP_042003_20020615_20200916_02_T1_MTL	Landsat7	Dobbin, Eugenie, Parrish
20030716	Multispectral_LE07_L1TP_046002_20030716_20200916_02_T1_MTL	Landsat7	Dobbin, Eugenie, Parrish
20040509	AST_L1T_00305092004193957_20150504095832_27020_V.tif	Aster	Dobbin, Eugenie
20040509	AST_L1T_00305092004194006_20150504095839_41300_V.tif	Aster	Parrish
20050621	AST_L1T_00306212005234333_20150510002850_53266_V.tif	Aster	Dobbin, Eugenie
20050814	AST_L1T_00308142005195133_20150510183333_45201_V.tif	Aster	Parrish
20060622	Multispectral_LE07_L1TP_046003_20060622_20200914_02_T1_MTL	Landsat7	Parrish
20060817	AST_L1T_00308172006195149_20150515185827_43491_V.tif	Aster	Dobbin, Eugenie
20070722	AST_L1T_00307222007184506_20150520170156_121419_V.tif	Aster	Dobbin, Eugenie
20070817	AST_L1T_00308172007192156_20150521003622_12156_V.tif	Aster	Parrish
20080606	Multispectral_LE07_L1TP_043003_20080606_20200912_02_T1_MTL	Landsat7	Dobbin, Eugenie
20080627	Multispectral_LE07_L1TP_046003_20080627_20200912_02_T1_MTL	Landsat7	Parrish
20090625	Multispectral_LE07_L1TP_043003_20090625_20200911_02_T1_MTL	Landsat7	Eugenie
20090720	Multispectral_LE07_L1TP_042003_20090720_20201020_02_T1_MTL	Landsat7	Dobbin, Eugenie
20090720	Multispectral_LE07_L1TP_042003_20090720_20201020_02_T1_MTL / Multispectral_LE07_L1TP_043003_20090625_20200911_02_T1_MTL	Landsat7	Parrish
20100320	AST_L1T_00307032010005143_20150602013611_107591_V.tif	Aster	Parrish
20100608	Multispectral_LE07_L1TP_047002_20100608_20200911_02_T1_MTL	Landsat7	Dobbin, Eugenie
20110609	AST_L1T_00306092011192115_20150606070853_58195_V.tif	Aster	Parrish
20110701	Multispectral_LE07_L1TP_043003_20110701_20200910_02_T1_MTL	Landsat7	Eugenie
20110727	Multispectral_LE07_L1TP_049002_20110727_20200909_02_T1_MTL	Landsat7	Dobbin, Eugenie

20120701	Multispectral_LE07_L1TP_045003_20120701_20201008_02_T1_MTL / Multispectral_LE07_L1TP_043003_20120703_20201020_02_T1_MTL	Landsat7	Parrish
20120715	Multispectral_LE07_L1TP_047002_20120715_20200908_02_T1_MTL	Landsat7	Dobbin, Eugenie
20130504	Multispectral_LC08_L1TP_042003_20130504_20200913_02_T1_MTL	Landsat8	Dobbin, Eugenie, Parrish
20140505	Multispectral_LC08_L1TP_044003_20140505_20200911_02_T1_MTL	Landsat8	Parrish
20140701	Multispectral_LC08_L1TP_043003_20140701_20200911_02_T1_MTL	Landsat8	Dobbin, Eugenie
20150411	Multispectral_LC08_L1TP_047002_20150411_20200909_02_T1_MTL	Landsat8	Eugenie
20150501	Multispectral_LC08_L1TP_043003_20150501_20200909_02_T1_MTL	Landsat8	Parrish
20150810	Multispectral_LC08_L1TP_046002_20150810_20200908_02_T1_MTL	Landsat8	Dobbin, Eugenie
20160402	Multispectral_LC08_L1TP_050002_20160402_20200907_02_T1_MTL	Landsat8	Parrish
20160706	Multispectral_LC08_L1TP_043003_20160706_20200906_02_T1_MTL	Landsat8	Eugenie
20160807	Multispectral_LC08_L1TP_043003_20160807_20200906_02_T1_MTL	Landsat8	Dobbin
20170502	Multispectral_LC08_L1TP_047002_20170502_20200904_02_T1_MTL	Landsat8	Dobbin, Eugenie, Parrish
20180401	Multispectral_LC08_L1TP_049002_20180401_20200901_02_T1_MTL	Landsat8	Eugenie
20180601	Multispectral_LC08_L1TP_076242_20180601_20201015_02_T2_MTL	Landsat8	Parrish
20180701	Multispectral_LC08_L1TP_078242_20180701_20200831_02_T1_MTL	Landsat8	Dobbin
20190505	Multispectral_LC08_L1TP_083241_20190505_20200829_02_T2_MTL	Landsat8	Parrish
20190702	Multispectral_LC08_L1TP_048002_20190702_20200830_02_T1_MTL	Landsat8	Dobbin
20190812	Multispectral_LC08_L1TP_047002_20190812_20200827_02_T1_MTL	Landsat8	Eugenie
20200706	Multispectral_LC08_L1TP_078242_20200706_20200913_02_T1_MTL	Landsat8	Dobbin, Eugenie
20210504	Multispectral_LC08_L1TP_080242_20210504_20210517_02_T1_MTL	Landsat8	Eugenie, Parrish
20210805	Multispectral_LC08_L1TP_043003_20210805_20210811_02_T1_MTL	Landsat8	Dobbin, Eugenie
20220501	Multispectral_LC09_L1TP_046003_20220501_20230418_02_T1_MTL	Landsat9	Parrish
20220801	Multispectral_LC08_L1TP_042003_20220801_20220805_02_T1_MTL	Landsat8	Dobbin, Eugenie
20230504	Multispectral_LC09_L1TP_046003_20230504_20230505_02_T1_MTL	Landsat9	Parrish
20230701	Multispectral_LC08_L1TP_076242_20230701_20230711_02_T2_MTL	Landsat8	Dobbin, Eugenie
20240503	Multispectral_LC09_L1TP_082241_20240503_20240503_02_T2_MTL	Landsat8	Parrish
20240705	Multispectral_LC08_L1TP_042003_20240705_20240712_02_T1_MTL	Landsat8	Dobbin, Eugenie